UNIVERSITY OF SOUTHAMPTON

FACULTY OF PHYSICAL SCIENCES AND ENGINEERING

Optoelectronics Research Centre

Photonic Microfibre Devices Based on Carbon Nanotubes

By

Medya Fouad Namiq

Thesis for the degree of Doctor of Philosophy

December 2016

UNIVERSITY OF SOUTHAMPTON

ABSTRACT

FACULTY OF PHYSICAL SCIENCES AND ENGINEERING
Optoelectronics Research Centre

Thesis for the degree of Doctor of Philosophy

PHOTONIC MICROFIBRE DEVICES BASED ON CARBON NANOTUBES

By Medya Fouad Namiq

Photonic fibre devices based on the interaction of evanescent fields with materials possessing high Kerr nonlinearity such as carbon nanotubes are promising as an efficient, low loss and low cost devices to be employed in all-optical system applications. Specifically, this report encompasses the work toward addressing the basic key parameters to design and fabricate sufficient all-optical fibre devices based on coated CNTs. Thus, the fundamental concepts of optical fibres; fibre Bragg gratings (FBG), Optical nonlinear (ONL) properties and their effects, CNTs characteristics have been explored. Experimentally, an etch method by utilizing HF acid has been proposed to reduce cladding diameter of the optical fibre and to extend the overlapped evanescent waves to the outer-cladding, thus gaining an efficient interaction with the nonlinear effect of CNTs. And, we probed a numerical model for SMF-28 fibre to estimate the fraction of evanescent field coupling within outer-cladding. In addition, real-time monitoring of etching process for both standard fibre SMF-28 and uniform FBG have been applied to demonstrate the influence of etching cladding diameter on the insertion loss of both fibre simultaneously. An optical deposition technique has been proposed to fabricate all-optical fibre devices by CNTs dispersed in DMF solution to be coated on the etched fibre. Moreover, Four wave mixing (FWM) has been performed experimentally and numerically to optimize the fabricated devices. A numerical study has been propped for the effective nonlinear coefficient of the fabricated all-optical fibre devices where it reported on interested results. With the purpose of controlling the losses, the extended fraction of the evanescent field in the etched optical fibre, a simple technique based on measuring, in-situ, the differential relative shifts of the Bragg resonances between the fundamental mode LP01 and the higher-order modes; LP11, LP02, LP21, LP12, LP31 in an etched FBG with accuracy precision ~0.2μm. Furthermore, we determine the refractive index of buffered Hydrofluoric (BHF) acid to be 1.36± 0.005 at 1.55μm. The experimental results were compared with simulations and exhibited excellent agreement. Adding to that, we applied this technique experimentally as a sensor for detecting the change of water salinity and as detector of thermal change based on the relative shifts of between the LP01 and first higher-order mode LP11. This it came matched with the simulations results. A Bragg wavelength shift has been observed about 3.3nm from complete etched cladding of the FBG and has been confirmed simultaneously. In additional work ,for thinned FBG the evanescent field of the propagating mode within outer-cladding and the effect of surrounding refractive index on effective refractive index, Bragg wavelength shift for LP01, LP02 and LP03 have been simulated.

Table of Contents

List of Tables

List of Figures

DECLARATION OF AUTHORSHIP

I, Medya Fouad Namiq, declare that the thesis entitled "Photonic Microfibre Devices Based on Carbon Nanotubes" and the work presented in it are my own and has been generated by me as the result of my own original research.

I confirm that:

1. This work was done wholly or mainly while in candidature for a research degree at this University;
2. Where any part of this thesis has previously been submitted for a degree or any other qualification at this University or any other institution, this has been clearly stated;
3. Where I have consulted the published work of others, this is always clearly attributed;
4. Where I have quoted from the work of others, the source is always given. With the exception of such quotations, this thesis is entirely my own work;
5. I have acknowledged all main sources of help;
6. Where the thesis is based on work done by myself jointly with others, I have made clear exactly what was done by others and what I have contributed myself;
7. Parts of this work have been published as conference contributions as listed in List of Publications.

Signed: .....

Date: .....

Acknowledgements

First of all, I want to express my sincere appreciation to Dr. Morten Ibsen for his support, patient supervision and assessment during my doctoral research work.

I am also thankful to Optoelectronics Research Centre (ORC), University of Southampton for offering this valuable opportunity of study and support for my studies. ORC has been an inspiring place for me to pursue my PhD studies. Big thank to Dr Colin Sones for his help and assistance during work. I am grateful for all of my colleagues and friends; for your help, kindness, support and assistance that I gained it all during my study.

Last but not least, for my dearests father and mother, my brother, my partner and all of my family; without your prayers, support, patient and courage during many tough times during my study years I couldn't achieve this level of success, I owe you all an infinite gratefulness for the rest of my life.

Abbreviations

2D	Two-dimensional
ACCVD	Alcohol Catalytic Chemical Vapour deposition
ASE	Amplified Spontaneous Emission
BHF	Buffered Hydrofluoric Acid
CNTs	Carbon nanotubes
CVD	Chemical Vapour deposition
DMF	Dimethylformamide
DUT	Device Under Test
EDFA	Erbium-doped fiber Amplifier
FBGs	Fibre Bragg Gratings
FP	Fabery-Perot Laser source
FWM	Four-wave mixing
HF	Hydrofluoric Acid
IL	Insertion Loss in the optical fibre
MF	Micro Fibre
MFBGs	Micro Fibre Bragg Gratings
MFPD	Micro-Fibre Photonic Devices
MWCNT	Multi-wall carbon nanotube
NA	Numerical Aperture
NLO	Nonlinear Optical
OSA	Optical Spectrum Analyser
SBS	Stimulated Brillouin Scattering
SiO_2	Silicon dioxide
SMF	Single Mode Fibre
SPM	Self-Phase modulation
SRS	Stimulated Raman Scattering
SWCNT	Single-wall carbon nanotube
TFBGs	Titled Fibre Bragg Gratings
XPM	Cross-Phase modulation

Nomenclature

l	Azimuthal order of the propagated mode
λ_B	Bragg wavelength
Θ	Chiral angle in the CNTs
C_h	Chiral vector of CNTs
$\emptyset(z)$	Chrip phase
Γ	Core mode confinement
Ω	Coupling coefficient of FBGs
Δk	Detuning wave-vector of FBGs
d_{CNT}	Diameter of the CNTs
D_{fibre}	Dimeter of the etched fibre
Z	Distance along the fibre axis
L_{eff}	Effective length
A_{eff}	Effective mode area
n_{eff}	Effective mode index
γ_{eff}	Effective nonlinear coefficient
E_{ii}	Energy band gap
a	Fibre core radius
$J_l(x)$	First kind of Bessel function
ε_o	Free-space permittivity
L	Grating length
Λ	Grating period
n_g	Group index
v_g	Group velocity
P_{in}	Input pulse peak power
n_o	Linear refractive index
α_o	Linear saturable absorption coefficient
γ	Nonlinear coefficient
n_{NL}	Nonlinear coefficient refractive index
L_{NL}	Nonlinear length
Φ_{NL}	Nonlinear phase shift
$\overline{n_{NL}}$	Nonlinear refractive index
$\chi^{(i)}$	Nonlinear susceptibility
α_{int}	Non-saturable absorption coefficient
V	Normalized frequency (V-number)

b	Normalized propagation constant
E	Optical electric field
ω	Optical frequency
I	Optical intensity
α	Optical loss in the fibre
β	Propagation constant
$n_{cladding}$	Refractive index of fibre cladding
n_{core}	Refractive index of the fibre core
α_{NL}	Saturable absorption in CNTs
$K_l(x)$	Second kind of modified Bessel function
c	Speed of light
Δn_a	The amplitude
P	Total optical polarization
k_o	Vacuum propagation constant
a_i	Wave vectors of the graphite sheet
λ	Wavelength
η	wavelength conversion efficiency

Chapter 1 : Introduction

1.1 Photonic Fibre Devices

Photonic devices are components for generating, controlling or detecting light[1]. In recent years, photonic devices based on microfibers have been widely employed for a range of versatile fields such as telecommunication, sensing and industry. The continuous progress and investigations in these microfibres have motivated research into novel photonics devices with the aim of producing low cost and heightened efficiency, given their interesting properties from efficiently interacting with the evanescent field to the confinement of the propagated mode in the microfiber. This thesis explores the design and fabrication of photonic microfibre devices (PMFD) based on wet chemical etching technique of the silica-cladding fibre, then optically coated with highly nonlinear materials and their potential use in photonic applications.

Progressively, a wide number of future high capacity communication network applications are projected to be based on the Kerr nonlinearity optical effects. For example, ultrafast switching, signal generation, high speed demultiplexing are all functions that can be achieved using Kerr nonlinearity. That is, through engaging a number of nonlinear optical materials (NLO) with all-optical system theoretically and experimentally, where these NLO-materials are classified as molecular materials (for instance, polymers, organic molecules and organic crystal) and bulk materials (for instance inorganic crystals, semiconductors, metals) [2, 3].

Consequently, for its extraordinary mechanical, thermal, electrical and optical properties, in particular the high nonlinear optical properties, the focus on carbon nanotubes CNTs research has increased over the past decade. In 1985, H.W. Kroto et al. reported a carbon molecular C60 mediated by laser pulse vaporization. Later, in 1991, multi-wall- CNTs (MWCNTs) were discovered by Iijima and Ichihashi [4]; two years later, they found the single-walled carbon nanotubes (SWCNTs)[5]. In addition, in 1996 Thess et al. produced an almost uniform small diameter of single-wall carbon nanotubes [6]. After the discoveries of CNTs, the investigations around it have grown and are ongoing. These investigations are related to their diameter, tubules length, their properties or efficient applications.

Because of the level of Kerr nonlinearity in CNTs is high with an ultrafast response and great saturable absorber; they are highly applicable in many optical nonlinear-based devices [5, 7-10]. Many applications have been demonstrated by utilising CNTs starting in 2003 in the nonlinear photonic area such as passive-saturable absorbers[11, 12], Four-wave mixing (FWM) based on wavelength conversion [13-15], and in passively mode-locked lasers [16, 17].

1.2 Micro-sensors Based on Etched Fibre Bragg Gratings

Over the last decades, fibre Bragg grating is known by low insertion loss, fibre compatibility and compact design. Such fibres have been utilized in a wide range of fields and have found numerous uses in a wide range application fields, such as optical sensing, as the technology is sensitive to strain, ambiance refractive index and temperature, and in optical telecommunication such as filtering, fibre laser, fibre amplifier, and optical add/drop multiplexer[18-20]. Alternatively, the efforts have risen to study nonlinear effects in the intensity dependant refractive index of the FBG throughout the control of fibre diameter as well as the index of the surrounded medium.

This has lit up the way for optical sensing field as well, as they are showing a high sensitivity and fast response based on the extended rate of the evanescent field and any perturbation in the effective refractive index of the fibre. Later, the FBGs sensors also showed more comparable sensing with microfibre sensors and they have been implemented in many sensing elements. Consequently, in the recent years, etched-FBG has generated a considerable interest in the development of the standards of optical fibre based sensing techniques and other applications developed with high sensitivity and fast response [21, 22].

1.3 Thesis Structure

This Thesis is divided into seven chapters. First, an introduction to the PMFDs based on wet chemical etching and the rate of interaction of evanescent field then their implantations in nonlinear optical effects and optical sensing has been provided. This chapter is followed by the motivation and aims of this work, represented in part one. Chapter 2 presents an indication of the fundamental background theory and the concepts for optical fibres, FBGs, nonlinear optical (NLO) properties and its effects, together with the basic characteristics of high nonlinear coating materials like CNTs.

Next, Chapter 3 will investigate and describe in detail the fabrication process of PMFDs and the wet chemical etching technique by using standard single mode fibre. In this chapter, the experimental work and the obtained results during real-time monitoring of etching silica-cladding fibre of single mode fibre and FBGs will be described, followed by an analysis of the insertion losses of these devices.

In Chapter 4, investigating the optical deposition process for coating the etched surface of silica-cladding fibres with CNTs in different methods, subsequently applying these PMFDs coated with CNTs in nonlinear applications such as FWM experiments. Moreover, the PMFDs coated with CNTs examined as a saturable absorber has been exhibited in Chapter 4. The modelling theory of etched optical fibre and simulation work of optimizing the overlapped

power fraction in the outer-cladding, as well as a simulation model of etched FBG and their changes of effective refractive index have been described in Chapter 5. Also, Chapter 5 will be included on the numerical results of the effective nonlinear efficiency of coated PMFD with CNTs.

In Chapter 6, the focus will be on a simple technique based on the relative shifts of higher-order modes generated in the etched FBG and its implantations. This chapter will be investigating how we will be able to determine the diameter of etched optical fibre precisely based on that technique. In addition, applying those etched FBG as sensors of refractive index sensors, water salinity will be demonstrated. The experimental and simulation works have been reported as well in this chapter.

Finally, this thesis ends with Chapter 7, which includes the summery of all the work that has been done experimentally and numerically followed by the suggested available areas for future work.

1.4 Motivation & Objectives

CNTs has shown extraordinary optical properties, which has attracted the attention of many researches to be used in promising technologies, especially, in optical fibre and FBG applications in all-optical systems.

However, the field of CNTs based photonic devices is still relatively new but an increasing number of researches have been attempting to explore and exploit their promising properties in many all-optical applications. Since 2003, many implantations of CNTs has been raised as saturable absorbers for mode-locked lasers [7, 10, 23-25].. On the other side, exploiting the interplay of the evanescent filed of the guided mode in the optical fibre with CNTs has been demonstrated in nonlinear optical applications. This application involves either tapering optical fibre, using D-shaped fibre, by hollow optical fibre or applying it in all-fibre mode locked and as a tuneable wavelength conversion such as FWM [14, 15, 17, 26-29].

From another point of view, research groups have started demonstrating the CNTs based on optical fibre devices to be employed in nonlinear applications such as a D-shaped fibre deposited by SWCNTs generated a FWM. This has been examined with interaction length of 5cm and insertion loss of 12dB obtaining an effective nonlinear coefficient about 563 $W^{-1}km^{-1}$ and 6nm as a tuning range of wavelength within -31dB of conversion efficiency [14]. Then, the same process but with a tapered standard optical fibre and deposited with SWCNTs within 9dB as insertion loss to generate a FWM resulted in a 6 nm wavelength tuning range with a -48 dB as conversion efficiency and an estimated effective nonlinear coefficient of 1.81×10^{5} W-1km-1 [15]. In another demonstration, employing the same above experiment, a

highly impressive effective nonlinear coefficient of about 1816.8W-1km-1 for conversion efficiency of -27dB and tuning range about 9nm and 5 dB as an insertion loss of the tapered optical fibre coated by SWCNTs device have been demonstrated from a 5cm long device by B. Xuand et al.. However, this was done with some modification of using CNT/polymer composited coated tapered fibre [28].

K. T. Dinh et al. [30] studied the influence of optical absorption of coated CNTs on thinned FBGs. This resulted in a tuneable reflection band of FBG via in-line optical power control. They demonstrated tuneable filters with a 2 nm range of tuning and -13.5dB limited output of high optical power blocker [30]. L. Shao et al. demonstrated a tilted fibre Bragg grating (TFBG) wrapped by SWCNTs around the cladding to generate a FWM by the interaction of core and cladding mode. This resulted in a tuned wavelength with a range of 7.8 nm, and an estimated effective nonlinear coefficient of SWCNT is 1.8×10^{3} W-1km-1, and a conversion efficiency of about -52 dB [13]. G. E. Villanueva et al. have presented an optical tilted fibre grating coated using SWCNTs by two depositions on cladding techniques: the dip-coating and wrapping. This has shown an effective intensity (12%) modulation mediated by the nonlinear cladding coupling mode of TFBG [31]. Recently, a thinned FBG coated by MWCNTs for photomechanical optic modulator has been reported by B.N. Shivananju and his colleagues resulting in tuning the Bragg wavelength for a range of optical wavelength from IR , visible light and UV light [32].

In recent years, microfibre Bragg gratings (MFBGs) have inspired a lot of interest and many have been applied in numerous potential applications of sensing filed such as chemical, biological, structural[18, 33, 34]. Their efficient evanescent filed, confinement of mode, immunity to electromagnetics filed, low loss, compactness and low cost-effective have made them competitive in comparison with the other conventional electrical sensors and optical sensors [21, 22, 35]. MFBGs are mainly generated by either wet chemical etching [21, 36, 37] or by inscribing FBG on tapered fibres thermally stretched or MFs [38-40]. Hence, these MFBGs are utilized as higher sensors for refractive index [41, 42], temperature, strain[43-45], humidity[46, 47], gas sensing[48, 49], water salinity[50]. Therefore the basic ambitions of this project are:

• First, the aim of this thesis is the probable design, fabrication, and optimization of photonic nonlinear all-optical fibre devices based on coated CNTs. This includes investigating and examining the promising interaction of Kerr-nonlinearities of coated CNTs with the propagated evanescent field in the outer-cladding of fibre, for the purpose of obtaining a uniform long length of nonlinear interaction and high efficiency photonic devices. These photonic fibre devices will be fabricated by chemical wet etching of silica-cladding of either standard optical fibre or FBG. This leads to study the possibility of exploiting the technology

in a number of promising, more efficient, low cost and low power loss nonlinear all-optical fibre-based applications. For instance, four wave mixing (FWM), self-phase modulation (SPM), wavelength conversion, optical signal switching, and signal regenerating.

• Secondly, exhibiting a simple yet efficient technique for enhancing the measurement of etched optical fibre, in-situ, with high precision. This technique is based on etched FBG and studying the relative shifts of Bragg resonances between the fundamental mode LP01 and higher order modes (LP11, LP21, LP02, LP12, LP31) with different diameters of the etched fibre. In addition, the influence of changing the refractive index of the surrounding medium with the evanescent wave of a thinned cladding optical fibre will be probed. The differential relative shifts of these higher order modes are proposed and examined as a high efficient detector of refractive index change induced by applying different measurands. This can be utilized as a temperature sensor as well. This low cost, ease of configuration as well as compactness of sensors provides sufficient properties that have special importance for health environment monitoring, and biological and chemical sensors that require a high level of sensitivity.

Chapter 2 : Background Theory

2.1 Introduction

In recent years, PMFDs have attracted a great interesting in a variety of all-optical applications, and that's for their remarkable properties such as; low cost, evanescent field, small size, low loss, compactness, flexibility and configurability. These features of PMFDs have a replacement potential of bulky and lossy optical devices in versatile optical applications like; telecommunication, sensing and laser [35, 51-56]. There are several ways to fabricate microfibers such as flame brush technique which is based on stretching heated SMF to form a microstructure fibre and mainly used to fabricate optical fibre couplers, and tapered fibres[57]. The fabrication of microfibres in this work is proposing the wet chemical etching technique that is based on the use of buffered HF acid solution to produce cladding-etched optical fibre intended for use as a platform for fiberized photonic devices. Hence, the mainly optical fibre utilized in this work is standard single-mode fibre either if bare optical fibre or FBG. In this chapter, we are going to describe the basic concepts and properties of optical fibre of SMF as well as FBGs. The second part will focus on the nonlinear effects in optical fibre and some of its applications such as four-wave mixing (FWM) and self-phase modulation (SPM). Finally, the third part will be a background review of highly nonlinear materials that will be applied later for coating the PMFDs, such as carbon nanotubes (CNTs) and their basic optical and nonlinear properties.

2.2 Optical Fibre

The simplest silica-based optical fibre consists of two concentric homogeneous dielectrics as shown in Figure 2.1. The inner dielectric core fibre has a refractive index of $n_{core,}$ while the outer dielectric cladding fibre has a refractive index of $n_{cladding}$ where $n_{cladding} < n_{core}$ [58] .

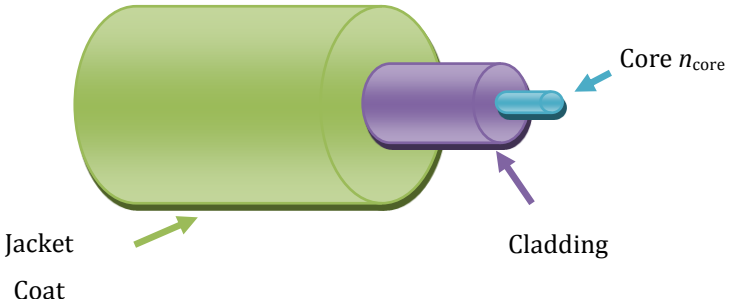

Figure 2.1: Step-index optical fibre structure.

The key structural parameters for step-index fibre are the numerical aperture (NA), the normalized frequency V-number, and the normalized propagation constant b, given by

$$NA = \sqrt{n_{core}^2 - n_{cladding}^2} = \sin \alpha_{max} \tag{2.1}$$

NA is associated with the maximum angle of the incident light α_{max}, which maintains its confinement inside the fibre core, and the normalized frequency parameter,

$$V = \frac{2\pi}{\lambda} . a. NA \tag{2.2}$$

where ***a*** is the core radius, and λ is the wavelength of the propagating light. V determines the cut-off conditions for the propagated mode as well as gives information about the power confinement within the fibre core. For the fundamental propagating mode; V≤ 2.405 [58].

$$b = \frac{\beta^2 - n_{cladding}^2 k_o^2}{n_{core}^2 k_o^2 - n_{cladding}^2 k_o^2} \approx \frac{n_{eff} - n_{cladding}}{n_{core} - n_{cladding}} \tag{2.3}$$

b is the normalized propagation constant, β is the propagation constant, n_{eff} is the effective refractive (mode) index and k_o is the vacuum propagation constant. For the case of LP_{lm} modes, (Linearly Polarized) where the propagated field mode equation is solved by b and applied the family of Bessel function is,

$$V\sqrt{1-b}\frac{J_{l-2}(V\sqrt{1-b})}{J_{l-1}(V\sqrt{1-b})} = V\sqrt{b}\frac{K_{l-2}(V\sqrt{b})}{K_{l-1}(V\sqrt{b})} \tag{2.4}$$

Where l is the azimuthal order of the mode, $J_l(x)$ and $K_l(x)$ are the Bessel functions of the first kind and the modified Bessel function of the second kind of order l, while, the ratio of the confined power in the core to the total power propagated within the fibre is given by

$$\Gamma = \frac{P_{core}}{P_{core}+P_{clad}} = (1-b)\left(1 - \frac{K_l^2(V\sqrt{b})}{K_{l+1}(V\sqrt{b})K_{l-1}(V\sqrt{b})}\right) \tag{2.5}$$

Figure 2.2 illustrates the normalized propagation constant b and the core mode confinement Γ and against the V-number for the fundamental mode (LP01 mode) of the step-index fibre. Nevertheless, this research is more interested in the ratio of the confined power within the outer-polymer cladding in a step-index fibre, and it will be explained in Chapter 5.

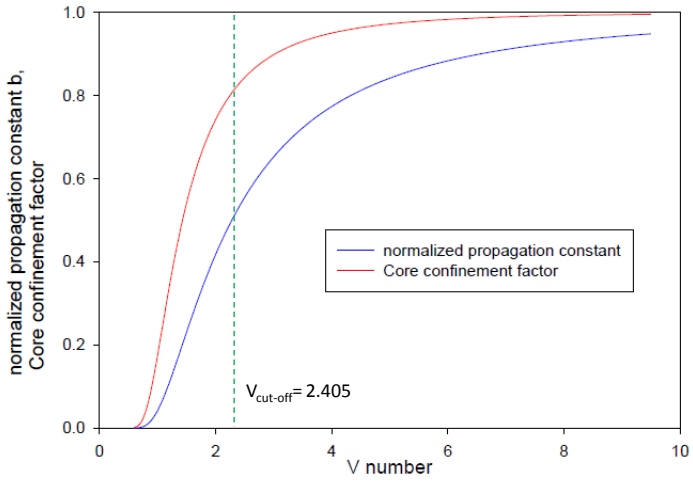

Figure 2.2: The normalized propagation constant b and the core confinement factor against the V-number for LP01 mode fundamental mode of step-index fibre [59].

2.2.1 Optical Fibre Dispersion

A substantial effect on the transmission of the signal light pulse through the optical fibre is chromatic dispersion, whereby, different spectrum components within optical fibre propagate at different speeds inducing pulse broadening. As a result, a walk-off effect occurred between narrowly spaced optical pulses[60]. The effect of fibre dispersion is calculated numerically within the propagation constant using Taylor series as a function of the frequency;

$$\beta(\omega) = n(\omega)\frac{\omega}{c} = \beta_o + \beta_1(\omega - \omega_o) + \frac{1}{2}\beta_2(\omega - \omega_o)^2 + \cdots \tag{2.6}$$

Where

$$\beta_m = \left[\frac{d^m\beta}{d\omega^m}\right]_{\omega=\omega_o} \quad (m = 0,1,2,\ldots.) \tag{2.7}$$

At the group velocity ($\nu_g = 1/\beta_1$) while the pulse broadening is accountable by the parameter β_2., the refractive index is associated with both parameters β_1 and β_2, expressed by;

$$\beta_1 = \frac{1}{c}\left[n(\omega) + \omega\frac{dn(\omega)}{d\omega}\right] = \frac{n_g}{c} = \frac{1}{v_g}, \tag{2.8}$$

$$\beta_2 = \frac{1}{c}\left[2\frac{dn(\omega)}{d\omega} + \omega\frac{d^2}{d\omega^2}\right] \cong \frac{\omega}{c}\frac{d^2n(\omega)}{d\omega^2} \cong \frac{\lambda^3}{2\pi c^2}\frac{d^2n(\lambda)}{d\lambda^2}, \tag{2.9}$$

where n_g is the group index and $n(\lambda)$ is the refractive index of the fibre at a wavelength of λ.

Fibre dispersion is influenced by two types of dispersion; material and waveguide dispersion[61]. Material dispersion is the result of the dependency of the material refractive index on wavelength. While the waveguide dispersion counts on the core radius, the core-cladding difference Δ, which are the parameter designs of the optical fibre, especially the single mode fibre. The relation of β_2 to the dispersion parameter is:

$$D = \frac{d\beta_1}{d\lambda} = -\frac{2\pi c}{\lambda^2}\beta_2 \approx \frac{\lambda}{c}\frac{d^2 n(\lambda)}{d\lambda^2} \tag{2.10}$$

2.3 Fibre Bragg Gratings

FBG in its simplest form consists of a periodic modulation of the refractive index of the core of a single mode fibre. This index modulation can result from exposing the core with an intense optical interference pattern created by, for example, a UV laser beam [20, 62, 63]. In order to understand the interesting nonlinear properties of the FBGs, their fundamental linear properties have to be expounded first [63].

The condition of Bragg wavelength λ_B with a strong coupling mode is given by,

$$\lambda_B = 2n_{eff}.\Lambda \tag{2.11}$$

λ_B is the input light wavelength, which is reflected back from the Bragg grating. The guided mode within the fibre core effective index is n_{eff}, while Λ is the grating period or pitch. For a uniform Bragg grating within the optical fibre core, the profile refractive index can be described by,

$$n(z) = n_{eff}(z) + \Delta n_a(z)\, cos\left(\frac{2\pi z}{\Lambda} + \emptyset(z)\right) \tag{2.12}$$

Where Δn_a is the amplitude of index perturbation, z is the distance along the fibre axis, and $\emptyset(z)$ is the chirp phase. Each reflection from the index perturbation pitch is in phase with the following one denoted as λ_B. The coupled-mode theory is a basic form to analyse FBG [19]. For a uniform amplitude of modulation, the reflection of Bragg gratings as a function of wavelength λ as well as grating length *L* is expressed by:

$$R(L,\lambda) = \frac{\Omega^2 sinh^2((\Omega^2 - \Delta k^2)L)}{\Delta k^2 sinh^2((\Omega^2 - \Delta k^2)L) + (\Omega^2 - \Delta k^2)cosh^2((\Omega^2 - \Delta k^2)L)} \tag{2.13}$$

Where Ω, Δk represent the coupling coefficient, the detuning wave-vector, respectively; as $\Delta k = k - \pi/\lambda$ and $\beta = 2\pi n_{eff}/\lambda_B$ is the propagation constant. Where the coupling coefficient Ω, for sinusoidal index perturbation changes along the fibre,

$$\Omega(z) = \frac{\pi \Delta n(z) \Gamma}{\lambda_B} \tag{2.14}$$

Γ denotes the power fraction of propagating mode within the fibre core as in Eq. (2.5), as it's a uniform grated fibre and Γ is approximately represented by $(1 - \frac{1}{V^2})$ as V is the fibre normalized frequency parameter.

As a result of the couple mode theory, for Δk=0 (no wave-vector detuning at uniform Bragg wavelength) and length of L of uniform fibre Bragg gratings within standard optical fibre, the peak reflectivity is seen to become,

$$R = tanh^2(\Omega L) \tag{2.15}$$

Where (ΩL) represents the grating strength; the peak transmission can be described by

$$T = 1 - R = sech^2(\Omega L) \tag{2.16}$$

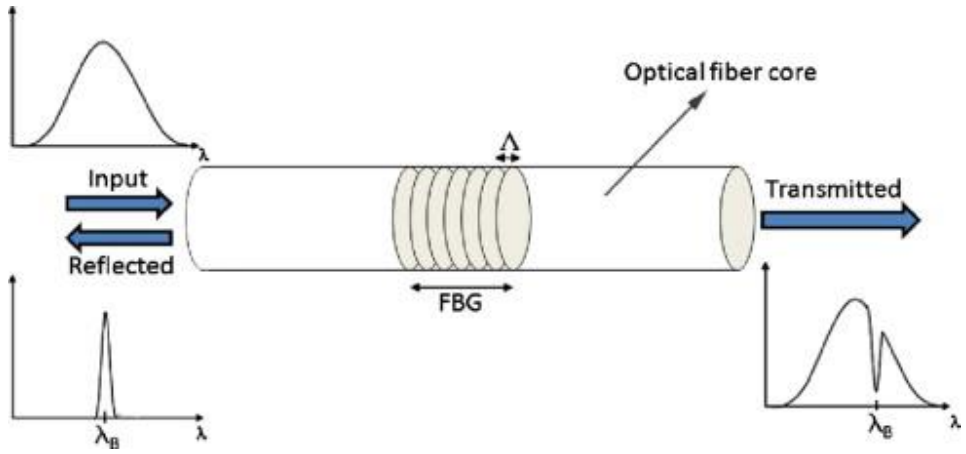

Figure 2.3: FBG concepts[64].

2.4 Nonlinear Effects in Optical Fibres

Optical nonlinearity is related to the response of the nonlinear medium refractive index with an intense optical intensity. Optical nonlinearities can be distinguished into two different classes as shown in Figure 2.4; they are described as:

1. Nonlinearities resulting from inelastic scattering at a high level of power. That occurs when the incident power surpasses its threshold value; the scattered light intensity rises exponentially[65]. This result of producing scattering effects, for instance, stimulated Raman scattering (SRS) and stimulated Brillouin scattering (SBS).

2. Nonlinearities arising from a change of refractive index. The dependency of power on refractive index results in the Kerr effect. This Kerr effect leads to different effects of nonlinearities depending on the input power, such as self-phase modulation (SPM) and cross-phase modulation (XPM) or creating new frequencies by combining several waves as in Four-wave mixing (FWM)[65, 66] .

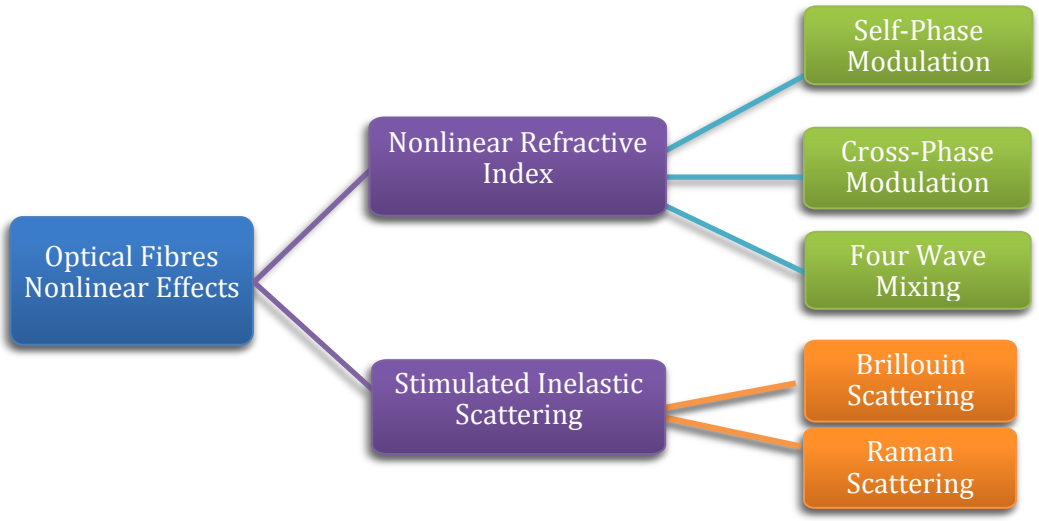

Figure 2.4: Nonlinear effects of Optical Fibre.

Through an intense optical field, the optical response of the material for both types of nonlinearities is tailored, and an expansion of polarization can explain it as,

$$P = \varepsilon_o(\chi^{(1)}E + \varepsilon_o\chi^{(2)}EE + \varepsilon_o\chi^{(3)}EEE) + \cdots \quad (2.17)$$

Where ε_o is the free-space permittivity, and $\chi^{(n)}$ represents the n^{th} order (n= 1, 2, 3, ...) of susceptibility at optical frequencies. The nonlinear susceptibility has been demonstrated in terms of real and imaginary parts. The real part interacts with refractive index while the imaginary part deals with either loss or gain[66]. The first term expression indicates $\chi^{(1)}$ the

linear susceptibility with dominant involvement to the polarization *P,* the second harmonic generation and sum- frequency as a result of the nonlinear effect of $\chi^{(2)}$, the second order of susceptibility; however, it non observable in silica fibre as a result of the inversion symmetric structure[60].

On the other hand, $\chi^{(3)}$, the third order of susceptibility creates the lowest-order nonlinear influences in optical fibre that results in a third harmonic generation, four-wave mixing, and nonlinear refraction.

2.5 Nonlinear Refractive Index

As a result of the contribution of $\chi^{(3)}$ nonlinearities and hence the most nonlinear effect in optical fibre occurring owing to the nonlinear refractive index, the refractive index of the optical fibre can be described by[60, 66],

$$\tilde{n} = n(\omega) + \overline{n_{NL}}\,|E|^2 \quad = \; n_o + \; n_{NL}|E|^2 \tag{2.18}$$

where n_o is the linear refractive index while $\overline{n_{NL}}$ is the nonlinear refraction part of index and E is the fibre optical electrical intensity field[66]. The nonlinear coefficient refractive index n_{NL}term is expressed by,

$$n_{NL} = \frac{3}{8n_o} Re\left(\chi^{(3)}\right) \tag{2.19}$$

The effective magnitude of the nonlinear coefficient γ given by,

$$\gamma_{eff} = \frac{2\pi n_{NL}}{\lambda A_{eff}} \tag{2.20}$$

where A_{eff} is the effective area In silica $n_{NL} \approx 2.6 \times 10^{-20}\, m^2.W^{-1}$,while for CNTs and Graphene $n_{NL} \approx 2 \times 10^{-12}\, m^2.W^{-1}$ and $n_{NL} \approx 10^{-11}\, m^2.W^{-1}$, respectively [66-68].

2.6 Nonlinear Application in Optical Fibre

As aforementioned, the nonlinear effects contributed in different applications in the optical fibre. In this section, we are going to focus on the influences of the Kerr effect on nonlinear optical applications. The main purpose of this nonlinear application is a way for optimizing the nonlinear coefficient effect γ in the nonlinear optical fibre. There are several techniques to measure the nonlinear coefficient; these include SPM and FWM.

2.6.1 Self-Phase Modulation

The dependency of the refractive index of the nonlinear material on high intensity causes phase change or nonlinear phase delay and generation of new wavelength, leading to a spectral broadening of the optical pulse[60], as a result of the third order nonlinearity $\chi^{(3)}$, which leads to a time-varying refractive index change. Moreover, from Eq. (2.18), the nonlinear index change Δn for a pulse with intensity envelope $E^2(t)$ could be expressed by[69, 70],

$$\Delta n = n_{NL}.E^2 \tag{2.21}$$

leading to a nonlinear phase shift or SPM, ϕ_{NL} of the propagating pulse along the fibre (at β_2=0), since $U(z,T)$ is the normalized amplitude expressed by,

$$A(z,\tau) = \sqrt{P_{in}}\, e^{-\left(\frac{\alpha z}{2}\right)} U(z,T) \tag{2.22}$$

then becomes,

$$\frac{\partial U}{\partial z} = \frac{i e^{-\alpha z}}{L_{NL}} |U|^2 U \tag{2.23}$$

P_{in} is the input pulse peak power, α represents the losses of the fibre, while the nonlinear length L_{NL} is,

$$L_{NL} = \frac{1}{\gamma P_{in}}, \tag{2.24}$$

γ indicates on the nonlinear index coefficient n_{NL} expressed by the formula; by solving Eq. (2.20) through substituting $U = V\, e^{i\phi_{NL}}$, the obtained real and imaginary part solutions are,

$$\frac{\partial V}{\partial z} = 0; \qquad \frac{\partial \phi_{NL}}{\partial z} = \frac{e^{-\alpha z}}{L_{NL}} V^2 \tag{2.25}$$

V represents the unchanged amplitude along the length of fibre L; thus the obtained general solution via analytic integration of the phase equation,

$$U(L,T) = U(0,T)\, e^{i\phi_{NL}(L,T)} \tag{2.26}$$

at z=0, $U(0,T)$ is the amplitude of the field and

$$\phi_{NL}\,(L,T) = \,|U(0,T)|^2 \left(\frac{L_{eff}}{L_{NL}}\right) \tag{2.27}$$

L_{eff} is the effective length given by ,

$$L_{eff} = \frac{[1 - e^{-\alpha L}]}{\alpha} \tag{2.28}$$

Since the nonlinear phase shift ϕ_{NL} is related proportionally to the fibre length L and owing to the fibre losses, its length L is greater than the effective lengthL_{eff}. Otherwise, when the losses are α=0, $L_{eff} = L$ and at T=0, and the centre of the pulse makes $|U(0,0)|$=1, the maximum phase shift ϕ_{NLmax} occurs by,

$$\phi_{NLmax} = \frac{L_{eff}}{L_{NL}} = \gamma P_{in} L_{eff} \tag{2.29}$$

As ϕ_{NL} is time dependent, SPM spectral broadening occurs. This temporal change in phase contributes to the instantaneous frequency shift through the optical pulse, which is also called frequency chirping and represented by $\Delta\omega$

$$\Delta\omega(T) = \, -\frac{\partial \phi_{NL}}{\partial T} = \, -\left(\frac{L_{eff}}{L_{NL}}\right)\frac{\partial}{\partial T}|U(0,T)\,|^2 \tag{2.30}$$

The induced frequency chirp is related proportionally to the propagating distance in SPM. On the other hand, the shape of the pulse and the instantaneous level of power in the pulse is considered in SPM in terms of the spectral broadening expand[60]. The SPM induced frequency chirp is given by,

$$\Delta\omega(T) = \, \frac{2m}{T_o}\,\frac{L_{eff}}{L_{NL}}\left(\frac{T}{T_o}\right|\Big)^{2m-1} e^{\left[-\left(\frac{T}{T_o}\right)^{2m}\right]} \tag{2.31}$$

where m=1 in the case of Gaussian pulse shape, while for higher values the shape of the pulse differs (e.g., it will be similar to a square or rectangular pulse)[60, 65] .

2.6.2 Four-Wave Mixing

FWM is one of the optical nonlinear effects that arising owing to the third nonlinearity contribution χ^3 (Kerr effect). Hence, FWM happens in case of two different wavelengths (frequencies) or more propagating together within a highly intense optical signal in a nonlinear medium such as optical fibre, and they give arise to a new wavelength known as idler. This high power of input raises the nonlinear effects in the optical fibre, which is caused by the optical Kerr effect[59, 71]. As a way of generating a new wavelength in optical fibre, the concept of FWM—based on the effect of the nonlinear third order of polarization as a function of the electric field and the third susceptibility χ^3—is given by ,

$$P_{NL} = \varepsilon_o \chi^3 E^3 \tag{2.32}$$

Assuming four optical waves linearly polarized along the x-axis, each wave propagating at different frequencies is represented by ω_1, ω_2, ω_3, ω_4. The total electric field for this case is given by,

$$E = \frac{1}{2}[E_1 e^{(k_j z - i\omega_1 t)} + E_2 e^{(k_j z - i\omega_2 t)}] + c.c \tag{2.33}$$

Applying Eq. (2.33) in Eq. (2.32), the nonlinear polarization will include a number of terms where,

$$P_4 = \frac{3\varepsilon_o}{4}\chi^3_{\chi\chi\chi\chi}\big[|E_4|^2E_4 + 2(|E_1|^2 + |E_2|^2 + |E_3|^2)E_4 + 2E_1E_2E_3e^{(i\theta_+)} + 2E_1E_2E_3^*e^{(i\theta_-)} + \cdots\big] \tag{2.34}$$

In Eq. (2.34), the four first terms result from the SPM and XPM. On the other side, $P_{NL} \propto 2E_1E_2E_3e^{(i\theta_+)} + 2E_1E_2E_3^*e^{(i\theta_-)}$ is responsible for the FWM, which is considered in this section as a way to characterize the nonlinear based devices [66].

The condition of parametric coupling of FWM depends on the matched different frequencies of the optical waves and their wave vectors in order to get a phase matched case, from Eq. (2.34), the terms of θ_- and θ_+ represented by,

$$\theta_\pm = (k_1 + k_2 \pm k_3 - k_4)z - (\omega_1 + \omega_2 \pm \omega_3 - \omega_4)t \tag{2.35}$$

k is the wave vector of the contributed optical waves. FWM includes two cases in terms of θ . First, when θ_+ is the case of launching three optical waves where the mix leads to the creation of a fourth new frequency wave ($\omega_4 = \omega_1 + \omega_2 + \omega_3$). Besides, this case generates either third harmonic THG ($\omega_1 = \omega_2 = \omega_3 \rightarrow 3\omega_1 = \omega_4$), or frequency conversion ($\omega_1 = \omega_2 \neq \omega_3$). The second case at θ_-, when launching two optical pump waves of high

intensity having identical frequencies $\omega_1 = \omega_2$ and $\omega_3 = \omega_4$ leads to the generation of $(2\omega_1 - \omega_3)$ and $(2\omega_3 - \omega_1)$ [60, 66].

For phase match, the condition is given by,

$$\Delta k = k_3 + k_4 - k_1 - k_2 = \frac{n_3\omega_3 + n_4\omega_4 - n_1\omega_1 - n_2\omega_2}{c} = 0 \tag{2.36}$$

For $\Delta k = 0$, which most commonly occurs in Optical fibre, specifically$\omega_1 = \omega_2$, which represents degenerated FWM state (Figure 2.5). In this case, the frequency shift of launching highly intense optical pump wave generating two new optical frequencies— referred by signal (stokes bands) and idler (anti-stokes bands) located equally at each of $\omega_3$and ω_4, respectively ($\omega_3 < \omega_4$)—is represented by,

$$\Omega_s = \omega_1 - \omega_3 = \omega_4 - \omega_1 \tag{2.37}$$

where Ω_s is the frequency shift that occurs through the high pumped wave that transferred its energy on the other two waves.

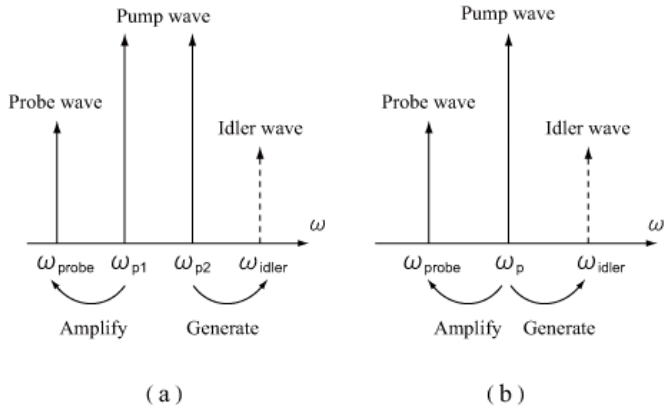

Figure 2.5: Typical Four-wave Mixing in frequency domain a) no-degenerate FWM b) degenerate FWM.

In the case of FWM, single mode fibre has a low dispersion at 1550nm. Therefore, as idler wave frequency is generated at $(2\omega_{pump} - \omega_{probe})$ where $\omega_{pump}, \omega_{probe}$ denote the pump and probe or signal frequency, respectively. The wavelength conversion efficiency η is represented by,

$$\eta = \left(\gamma P_p L_{eff}\right)^2 \tag{2.38}$$

γ is the nonlinear coefficient in the optical fibre given by Equation(2.20), P_p is the pumped power and L_{eff} is the effective length in the nonlinear optical fibre. In addition, it is important to satisfy the phase-match condition in order to get high conversion efficiency for the FWM.

2.7 High Nonlinearity Coating Materials

All the materials under the interaction of intense light show nonlinear optical (NLO) effects; these materials are gases, liquids or solids. There are two NLO material types, molecular materials (e.g., organics and molecules, organic crystal and polymers) and bulk materials (e.g., inorganic crystals, semiconductors, and metals). These promote the design and fabrication of nonlinear-based photonic devices[2], as the concerns focused on CNTs in this work with the purpose of extracting and exploiting its nonlinear optical features.

The unique atomic structure and properties of CNTs are due to the type, strength and the number of bonds and basically from the sp^2 hybridization in the elemental carbon [72, 73]. The first fullerence, C_{60}, discovered by Rick Sammolly and co-workers in 1985 which is a molecular includes on 60 carbon atoms bonding together in pentagon or hexagon form. Then, in the early of 1990, the discovery of carbon-nanotubes has established a huge route for potential applications in various scientific disciplines including; electronics devices(wires, transistors, interconnectors), reinforced materials. [74], optoelectronics (light emitting diodes, lasers), sensors (gas sensors and biosensors) [75] [76], medicine and biology (biological labels, drug delivery carriers) [72, 73]. The early work in 1991 was reported on coaxial carbon cylinders known as multi-wall carbon-nanotubes (MWCNTs) then followed by the discovery of single-wall carbon-nanotubes (SWCNTs) in 1993, which are a one atomic thickness of carbon cylinders. For further CNTs key interesting features it will be described in the next section.

2.7.1 Carbon Nanotubes (CNTs)

2.7.1.1 Basic Properties of CNTs

A CNT, basically, is a cylindrical tube made of a 1-D carbon atom; simply, CNTs are assembled from wrapping a one-atom layer sheet of Graphene [77-79] . This sheet of Graphene is made of a net of honeycomb or hexagonal structure within π-bonded carbon atoms [14, 80, 81]as shown in Figure 2.6. The tubes have diameters of 1-3nm on an average[82] and a length of more than 1μm. Moreover, there are two types, single-wall and multi-wall CNTs, as aforementioned[77].The most common use in the electronic and especially the photonics application is the SWCNT, which is what we are more interested to implement in our single mode fibre. CNTs, whether single or multi-walls, are metallic or semiconductor depending on the diameter of tubes and the wrapping angle of the shells[83].

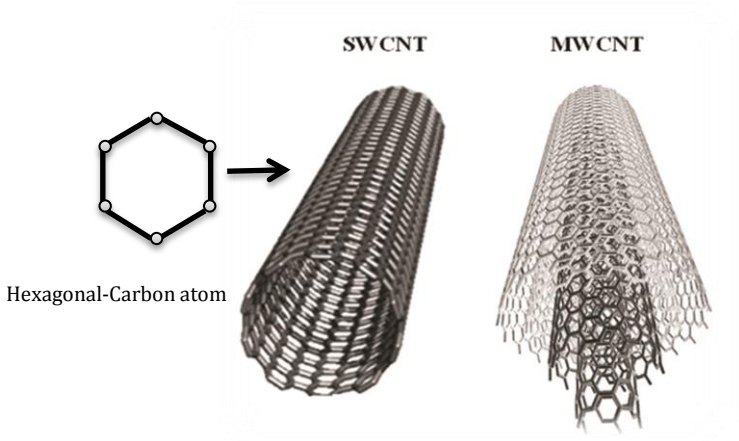

Figure 2.6: Single and Multi-Wall Carbon nanotubes[84].

There are different types of CNTs relative to the direction of wrapping the Graphene sheet layer and known by chiral vector C_h[78, 81] ,

$$C_h = na_1 + ma_2 \tag{2.38}$$

where, a_1 and a_2 is the wave-vectors of the graphite net sheet (as shown in Figure 2.7a), m and n defines the way of rolling the Graphene sheet. On the other side, the CNTs types are also relative to angle of wrapping the sheet known as chiral angle, θ which is ,

$$\theta = \tan^{-1}\left[\frac{\sqrt{3n}}{(m+n)}\right] \tag{2.39}$$

where there are three ways of sheet rolling; zigzag [θ=0°, (n=0 or m=0)], arm-chair [θ=30°, (n= m)], and chiral [0° < θ <30°, (n≠m)]. This leads to an influence on the electronic and optical properties of the nanotubes to be either metallic, in case of n−m=3k (k is integer, ≠0), or semiconducting, in case of n−m≠3k, as shown in Figure 2.7c [78, 81, 85].

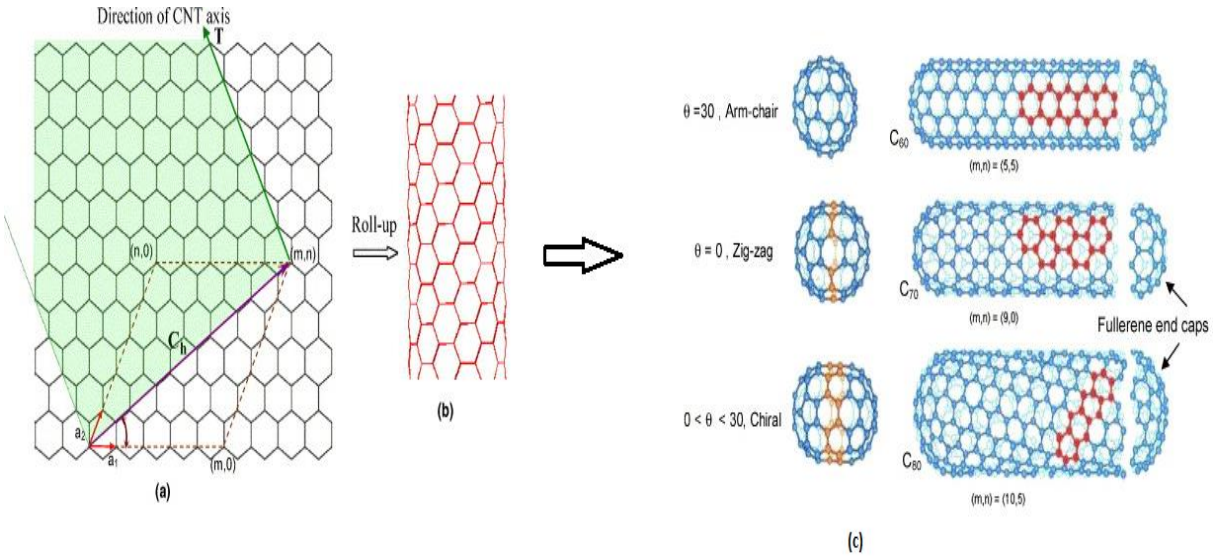

Figure 2.7: Schematic model illustrating of single-wall carbon nanotubes structure a) Graphene sheet. b) Single-wall carbon nanotubes (after wrapping). c) The different types of rolled Graphene with different chiral angles[78].

Metallic CNTs have a small finite band gap structure, which evinces more interest in numerous electrical applications for its high conductivity and electrical properties[8, 82]. The Semiconducting CNTs have significant optical properties relative to the direct band gap, where most of the optical transitions occur, as shown in Figure 8.2c, and 8.2d[77].

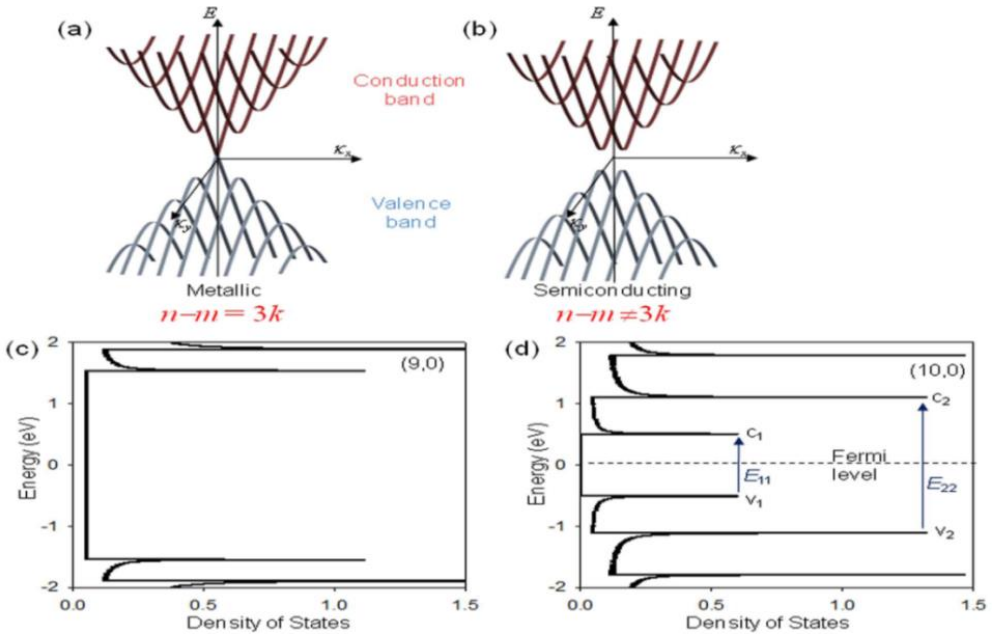

Figure 2.8: The band structures types .(a) Metallic CNTs (b) Semiconducting CNTs with their Energy band gaps c)Metallic and d)Semiconducting [78].

The energy band gap of the nanotubes is inversely proportional to the diameter of nanotubes[77, 82] as in Figure 9.2a. In the case of semiconducting CNTs, the optical transmission occurs between the conduction and valence band gaps (E_{11}, E_{22}....., E_{ii}), where the sharp spikes within the density of states are labelled as van Hove singularities[77, 86] . The energy band gap as E_{11} is given by:

$$E_{11} = \frac{2\gamma_o a_{C-C}}{d_{CNT}} \tag{2.40}$$

γ_o the transfer integral between first-neighbour π-orbital and its ranges (2.9-3.1eV) , a_{C-C} is the length of the C-C bond (0.142-0.144)nm while $d_{CNT} = |C_h|/\pi$ is the diameter of the CNTs[77, 78, 85] . Additionally, the wavelength transmission is in a parallel proportional with the CNTs diameter as $E(eV) = hc/\lambda$. Consequently, the semiconducting CNTs, as they are wavelength dependant, have a spectral transmission range of wavelength from about 600nm-2000nm as shown in Figure 9.2b[77, 86]. Moreover, the semiconducting CNTs possess a peak absorption wavelength, which it is defined by the mean of the nanotubes diameter[77].

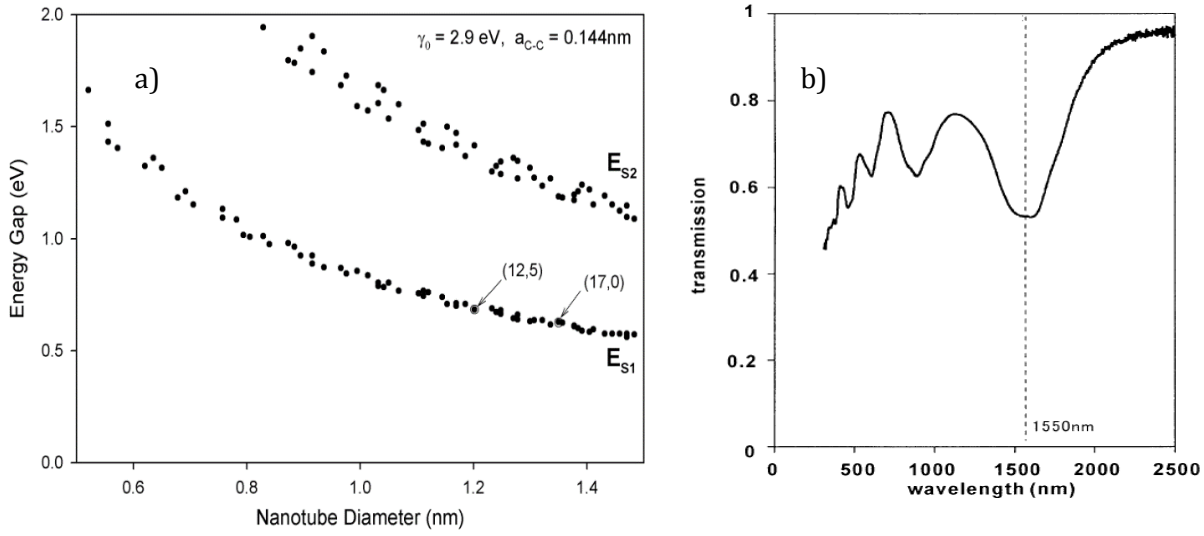

Figure 2.9: Represents a) part from Kataura-plot, for just the semiconducting energy band gaps of CNTs b) the transmission spectrum of SWCNT with a diameter ≈ 1.2nm [87].

There are many techniques for synthesizing or fabricating CNTs (Fig. 2.10); these include the carbon arc growth discharge, the laser ablation, sono-chemical or hydrothermal, electrolysis and the chemical vapour deposition (CVD); the last one is the most popular commercially[77, 86]. Besides, Alcohol catalytic CVD (ACCVD), is a technique leading to the deposit of a high quality and purity of CNTs straight onto the fibre that causes an increase in nonlinearity[26]. Recently, another method has been utilized for high quality production of CNTs of single-wall mediated by applying a thermal plasma, which is similar to the arc-discharge technique[88].

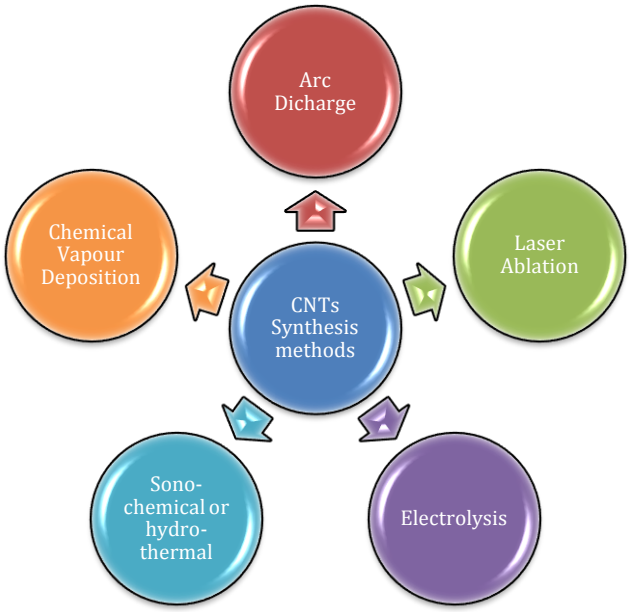

Figure2.10: Represents the method of synthesising of CNTs [89].

2.7.1.2 Optical Nonlinearity in CNTs

In this project, we seek after the nonlinear optical properties of CNTs, as they possess a very significant third order nonlinearity $\chi_{CNT}^{(3)}$. As a reason of the hexagonal structure of carbon nanotubes, it does not show any second order nonlinearities $\chi_{CNT}^{(2)}$. The $\chi_{CNT}^{(3)}$ nonlinearities CNTs are created by the delocalization of the π-band electrons. Moreover, the $\chi_{CNT}^{(3)}$ susceptibility is a result of essential three electronics mechanisms; firstly, within parted occupied band with a free electron motion, virtual electron transitions through the bandgap, and the electron motion into the band-interband transitions; Figure 2.11.

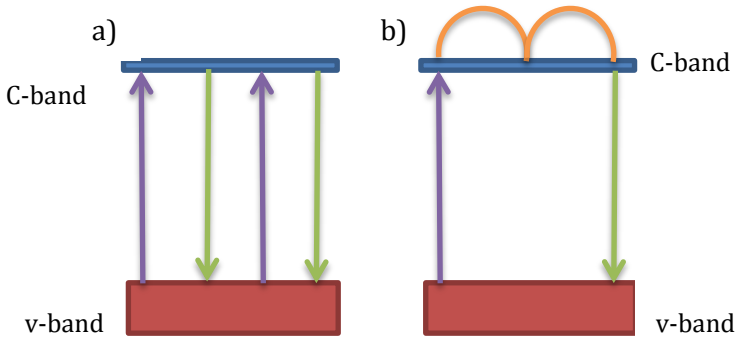

Figure2.11: The π-band electronic transitions band (re-schematic from [67]).

It has been estimated for typical single wall CNTs that $\chi^{(3)}_{\mathrm{CNT}} = 3\times10^{-9} esu$, according to the relation , $\chi^{(3)}_{\mathrm{CNT}} = 64.8(er)^4/\pi^2\,\gamma^3$; thus , it is believed that $\chi^{(3)}_{\mathrm{CNT}}$ is dependent on the nanotubes radius ; $\chi^{(3)}_{\mathrm{CNT}} \propto r^4$ [67].

On the other side, the real part of $\chi^{(3)}_{\mathrm{CNT}}$ is influenced by the intensity-dependant index of refraction and the two-photon absorption spectrum of the CNTs, where it has been estimated that $n_{NL} = 2 \times 10^{-12}\, m^2/W$ and the two photon absorption coefficient $\beta_{NL} = 5.5 \times 10^{-7}$m/W [67].

Another effect of $\chi^{(3)}_{\mathrm{CNT}}$, besides the nonlinear refractive index n_{NL}(expressed in Eq. (2.20)), is the saturable absorptionα_{NL}, which is responsible by the imaginary part of the third order of nonlinearities, described by [31]

$$\alpha_{NL} = \alpha_o + \alpha_{int} + \frac{3\omega Im\left(\chi^{(3)}_{CNT}\right)}{2\varepsilon_o c^2 n_0^2} I \tag{2.41}$$

where α_o is the linear absorption coefficient, α_{int} is non-saturable absorption coefficient. ω is the optical angular frequency. Besides, I and I_s are the optical intensity and the saturation intensity, correspondingly. Many types of research have reported the semiconducting CNTs showing a fast saturable absorption with a recovery time of few fs to 1ps [17, 77, 87]; as a result, these CNTs have been employed widely in passive-mode locking application [10, 12, 16, 17, 25, 26, 77].

2.8 Conclusion

This chapter has outlined the basic platform and principle to understand and form the confinement structure of PMFDs. At first, the fundamental properties of optical fibres from fibre structure, wave propagation and total power propagating within single-mode fibre, and the optical dispersion have been described. Then, the basic principles and condition of FBGs were exhibited. Followed by explanation the effects of optical nonlinearity in optical fibre and their main applications such as FWM and SPM, as a way to characterize and evaluate the nonlinear efficiency in the PMFDs coated with CNTs. A special emphasis was laid on the structure and optical and nonlinear properties of CNTs as it will be applied as the coating material around the microfibers as and it served as a route for enhanced performance in compact fibre-based photonic devices.

Chapter 3 : Microfibre Fabrication by Wet-Etching Technique

3.1 Introduction

In recent years, a novel new class of optical fibres has emerged known as microfibers (MF), microstructure optical fibres or sub-micron optical fibres. These fibres have opened up a promising rout for a wide range of potential photonics applications such as in supercontinuum, biomedical, biochemical and environmental optical sensing aspects [90, 91]. The two most common technique to fabricate MFs are either by tapering fibre, through extending the optical fibre thermally by flame brush to form a sub-micron diameter, or by wet-chemical etching of fibre optic using chemical acid solutions. The wet-chemical etch process has been proposed and applied to etch fused silica cladding of the optical fibre in this work; to achieve a percent or even less of evanescent field extending to outside the cladding-fused silica in single mode fibre with a controlled and precise method. Also, a high confinement for the propagated mode is maintained in the fibre core. In this chapter, we shall describe the experimental works that have been done as the fundamental basis for designing and fabricating nonlinear optical fibre-based devices. The first part deals with the procedure for optical fibre adaptation through wet etching of the silica-cladding by using a buffered chemical solution of hydrofluoric (BHF) acid and investigating the etching rate of this acid for two different concentrations, (20:1) and (7:1).The second part represents a comparison of the results of wet chemical etching aimed at both bare SMF-28 fibre sample and fibres with uniform Bragg gratings inscribed in their core. The final part of this Chapter demonstrates experimentally the effect of applying different surrounding refractive indices of solvents on etched uniform fibre Bragg gratings.

3.2 Wet Chemical Etching of Fused Silica-Cladding Fibre

First of all, since the proposed substance to be reduced in thickness is fused silica, hydrofluoric (HF) acid is the best solution to etch or ablate the surface effectively. Also, the smoothness and robustness of the surface of the etched-cladding fibre depend on the utilized acid concentration. In BHF acid, the etching time takes longer. However, it will result in an efficient optical quality of etched surface in the optical fibre.

In general, the most common method of micro-machining the surface of silica is HF or also known as hydrogen fluoride acid, and, as mentioned above, one of the ways of creating micro-sensors and micro-actuators [92]. Another method of fabricating micro-fibre (MF) is thermal

stretching of the optical fibre until the diameter is thinned to a few micrometres [93, 94]. However, for certain applications, it is preferred to use the method of wet chemical etching by HF acid because: 1) Fabricating MFs with maintaining on the propagating mode confined in the fibre core. 2) to expose a controlled percent of the fibre's evanescent field (with an extended tail of evanescent field) at the outer-cladding; 3) Fabricating MF sensors based on etched FBG to improve their sensing sensitivity to the surrounding refractive index and other certain applications, without the necessity to remove the cladding totally(as in the tapering method), on one side. On the other side, it serves to preserve the grating section in the core of the FBG from thermal treatment. 4) It allows for fabrication of MFs with less cost, limited time and specialised equipment.

3.2.1 Fused Silica Etching Process

Exceptional features of silicon glasses, such as optical transparency and sustainability in many harsh environments, can be considered as the most desirable in fabricating optical waveguides. However, silicon is affected by HF acid and can be easily dissolved at room temperature[92]. In HF acid, the chemical reaction of Silicon dioxide (SiO_2) dissolution can be described:

$$SiO_2 + 4HF \rightarrow SiF_4^{2-} + 2H_2O^+ \quad (3.1)$$

This represents the simplest formula of SiO_2 dissolution in the aqueous HF acid during the etching process[92, 93]. Because of the high electronegativity of fluorine, the strong Si-O bond of the tetrahedral silica network is attacked by the Hydrogen and Fluorine in the HF acid solution, subsequently, forming a hydroxyl group at 4 oxygen atoms of the SiO4. At that point, the hydroxyl group is attacked by fluorine ions and expands its categorizing number from 4 to 6, thereby SiF_6^{2-} is formed at the end of the chemical reaction [93].

3.3 Silica Single Mode Fibre Etching process

After the theoretical background for the standard single mode optical fibre was covered in Chapter 2, the experimental procedure for wet chemical etching of the optical fibre and the fabrication of MFs based on etched silica-cladding fibre will be discussed in this Section (as illustrated in Fig. 3.1). A single mode fibre (SMF-28-Corning Ltd.) has been the main optical fibre was used in the etching and fabrication process. It consists of core, cladding and coating diameters of 8.2µm, 125µm, 245µm respectively. The refractive index of the core and fused

silica-cladding are 1.4489 and 1.444, respectively, at λ = 1550nm with a numerical aperture of~ 0.12.

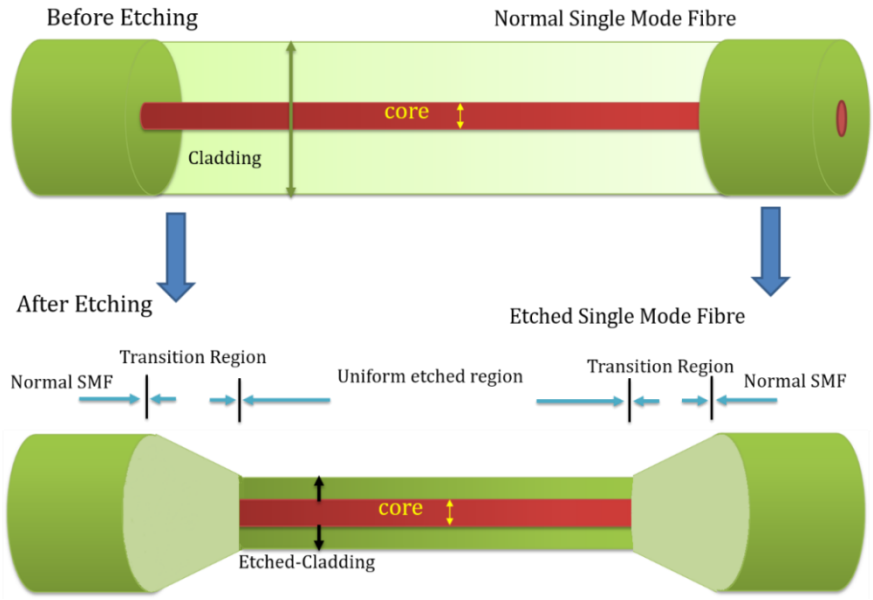

Figure 3.1: Schematic represents the single mode fibre before and after wet chemical etch of the silica cladding layer.

First step, at each etch process (etch run) we applied a set of prepared SMF-28 fibres. Each set has included 8 individuals of SMF-28 optical fibre samples together with fibre length about (1.5-2.0) meter and their middle sections were stripped of coating jacket [94]. The length of that middle section, to be etched, was 3-5mm. Later, for the purpose of increasing the nonlinear effective length for the proposed PMFDs coated with CNTs, the middle jacketless section of the SMF-28 samples was extended to be between 10-20mm. After that, the SMF-28 bare fibres were wiped and cleaned up by Isopropanol solvent to remove any residuals of jacket coating. The prepared fibre samples were mounted in a container made of Teflon/plastic, as it dose not react with BHF chemical acid solution. In this work we used two containers; the first container and then later the second container (improved design) as shown in Fig.3.2a and b. The first container was used at the beginning of etching process, then the replaced by a second container, because of some issues with the design of the first container in terms of protecting the mounted fibres, the robustness and optical efficiency of the etched fibres results.

At early stage of etching process, , when we used the first container as shown in Figure 3.1a, was employed to mount the SMF-28 fibre samples. The first container includes two holders made of the same material to hold the SMF-28 fibre samples during the etching process.

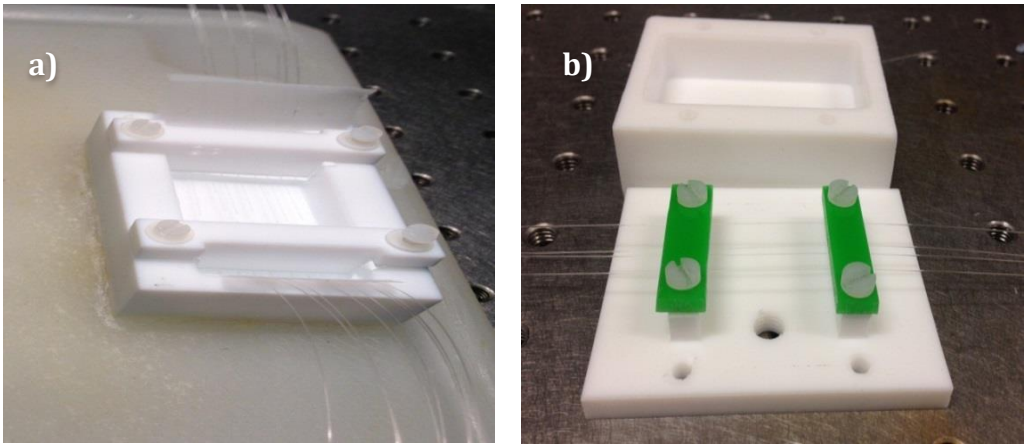

Figure 3.2: SMF-28 samples mounted in the Teflon/Plastic container and prepared to be etched by BHF acid. a) The first container. b) The second container.

As has been mentioned before, the chemical solution of BHF (commercial from OM-group) acid with a concentration of (20:1) [95] was utilized for etching the optical fibre cladding of SMF-28 fibre samples. This commercial chemical acid includes 20 parts of Ammonium Fluoride (NH_4F) (40% in water) and 1part of HF acid (48% in water). Moreover, the chemical BHF acid etching is the most common technique used to etch the cladding of an optical fibre as it maintains the cylindrical geometry of the optical fibre with a uniform and smooth reduction of cladding diameter through using the low concentration (20:1) [21, 45, 96, 97].

A number of etch processes to sets of optical fibres were run with the same concentration (20:1) and amount of BHF solution acid, which resulted on set of etched SMF-28 at each etch run and included 6-8 samples ascertained that all have been etched similarly. After each etch run, the remainder of the BHF solution in the container was removed carefully followed by rinsing the fibre samples and container with deionized water (DI-water) for about 10mins. Since HF acid solution is highly toxic, extra care and precaution was taken to ensure that the container is completely free from any residual HF. Following this, the container and the etched fibre samples were gently blow dried. Most of this stage of etching process had occurred under stable average temperature and relative humidity (RH) conditions of $21^{o} \pm 0.5^{o}$ C and 45%±5%, respectively. The resulted etched SMF-28 fibres were mounted on microscope glass and checked under the microscope (Nikon-Eclipse-LV150L) from any HF residuals, and the uniformity of the surface of etched-cladding fibre.

Later, we used a second container (made from Teflon/plastic), In the second stage, where this container was used after its design had alterations after modifying and doing alterations to the design of the container as shown in Figure 3.1b and that is due to; i) mainly, it was sought to reduce the speed of evaporation of the acid solution by means of a cover-lid for the container includes on two stages with a V-grooves. These grooves hold the mounted fibres in place. ii) Reduce the number of breaking in etched fibre samples after etching process and obtain etched fibre samples with more robustness and optical efficiency. Subsequently, the same procedure for etch process and the number of fibre samples were applied for each etch run as in the first container, also using the same chemical solution of BHF acid with the concentration (20:1), as it was mentioned above.

Then, we used another concentration of BHF acid solution (7:1) (commercial OM-group) for the purpose of speeding up the etching time and saving on the time consumed during the etching process. This concentration (7:1) had 7 parts of NH_4F (40% in water) and 1 part of HF (48% in water). Additionally, the refractive indices of both concentrations of BHF acid will be investigated experimentally and theoretically later in Chapter 6.

Furthermore, after finishing the etch process, and the check of the resulted etched fibre samples; these etched fibres (microfibres) were stored in transparent plastic boxes to prevent them from contaminations of dust or dirt particles.

3.3.1 Results and Discussion of the Etching Process of Silica Optical Fibre

The next step after the etching process from the first and the second containers, was to measure the thickness of the etched fibres after they had been taken out from the container carefully (as in some earlier stages of etch run, some of the samples were fragile D_{fibre}<10.0μm). All the etched fibre samples were measured with a microscope (Nikon-Eclipse-LV150L) to check the reduced diameter of the fibre cladding. Figures 3.3 and 3.4 depict some finished etched samples of SMF-28 fibre using the first and second containers, respectively. These are representing the resulted etched SMF-28 fibres from different sets of fibres after the etch process. The consistency of the etched surfaces of the cladding samples for SMF-28 fibres in each experiment of etch process can be noticed from Figures 3.3 and 3.4.

However, it is worth indicating here that we had faced concerns in the consistency of the etching rate, controlling the conditions of the etching process as well as the resulted etched samples; in terms of the targeted fibre thickness and the quality of the etched fibres, which led to the change in design of the etching container, as mentioned in section 3.3. Additionally, the second modified container is more efficient at handling and reducing the loss from

broken samples after each etching run due to the stability of the optical fibres that are mounted along the v-grooves' holders in the top of the lid of the second container (shown in Figure 3.2b), besides it has also resulted in etched samples of SMF-28 within a much thinner diameter (as shown in Figure 3.4c and d).

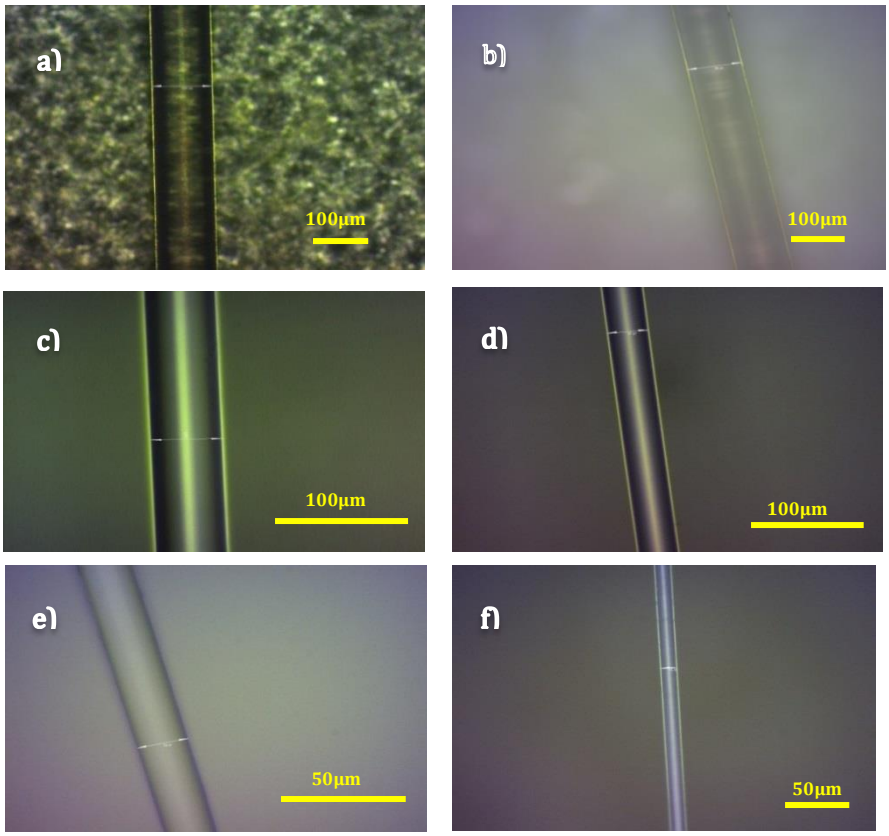

Figure 3.3: Number of etched SMF-28 samples by BHF acid with concentration (20:1) using the first container. a)D~111.0±0.5µm. b)D~98.6±0.5µm. c)D ~55.0±0.5µm. d)D~37.5±0. 5µm. e)D~20.0±0.5µm. f)D~15.6±0.5µm.

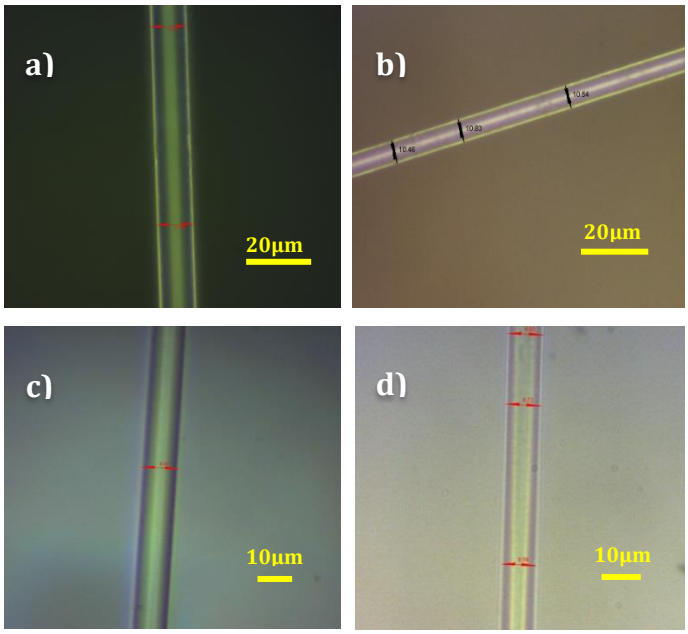

Figure 3.4: Number of etched SMF-28 samples by BHF Acid with concentration (20:1) and using the seconed container. a) D~11.8±0. 5µm. b) D~10.6±0.5µm. c) D~9.8±0.5µm. d) D~8.7±0.5µm.

Moreover, we noticed that humidity and temperature were another factors affecting the etching process, hence we put a digital monitor to measure the humidity and the temperature in the acid-wet bench during the etching process in the cleanroom. Figure 3.6 shows the collected data of relative humidity (%) and temperature (°C) at the cleanroom for around 53 hours within a 3-days period time (day-time and night-time) that included several runs of etching of SMF-28 fibre, on January 2013. It shows a strong evidence of a sharp drop in the relative humidity from about 45% to 25% to start fluctuating exponentially, until reaches lowest rate about 21% (the dotted-green line) on the second day of monitoring after the mid-day-time as caused by change of weather conditions or technical issues within the ventilation of the wet-bench acid at the cleanroom. Hence, that is what influenced the evaporation speed of the acid solution causing a rise in the dissolution acid rate and a change in the acid concentration, and thus, we believe, a change of the speed of etch rate and the targeted etched diameter at the end of the etch process.

On the other hand, it is quite clear that the temperature stayed constant within 21°C as an average (as shown in Figure 3. 6). However, strong temperature dependency of the speed of etch rate of BHF acid solution, where for an accurate control of the etching process and etch rate requires a temperature control within ±0.5°C [97-100]. Adding to that, Figure 3.5 represents the etch rate (Å/min) of different range of BHF acid concentrations versus different etchant temperatures (°C)[100]. From these dataset it believed that BHF acid with concentration (20:1), if applied in uncontrolled temperature condition will results in a

change of the etch rate about 100 Å/min.°C (for etched optical fibre waveguide from both sides-top and bottom- about 200Å/min.°C (1µm/hour.°C)) which it has been estimated based on the data in Figure 3.6[97, 100, 101]. Furthermore, any variation or inconsistent of the etching process condition and etchant temperature will be resulting in under- or over-etching for the targeted thickness of etched optical fibre. Hence, we solved these factors through; i) the alteration that was done to the etch container design (second Teflon/plastic container). ii) Calculating the etch rate of BHF for each new bottle of BHF acid solution that will be used in the etching process of the fibre optics in the cleanroom. iii) Monitor the temperature and the relative humidity (%) of the wet-etch bench at the cleanroom.

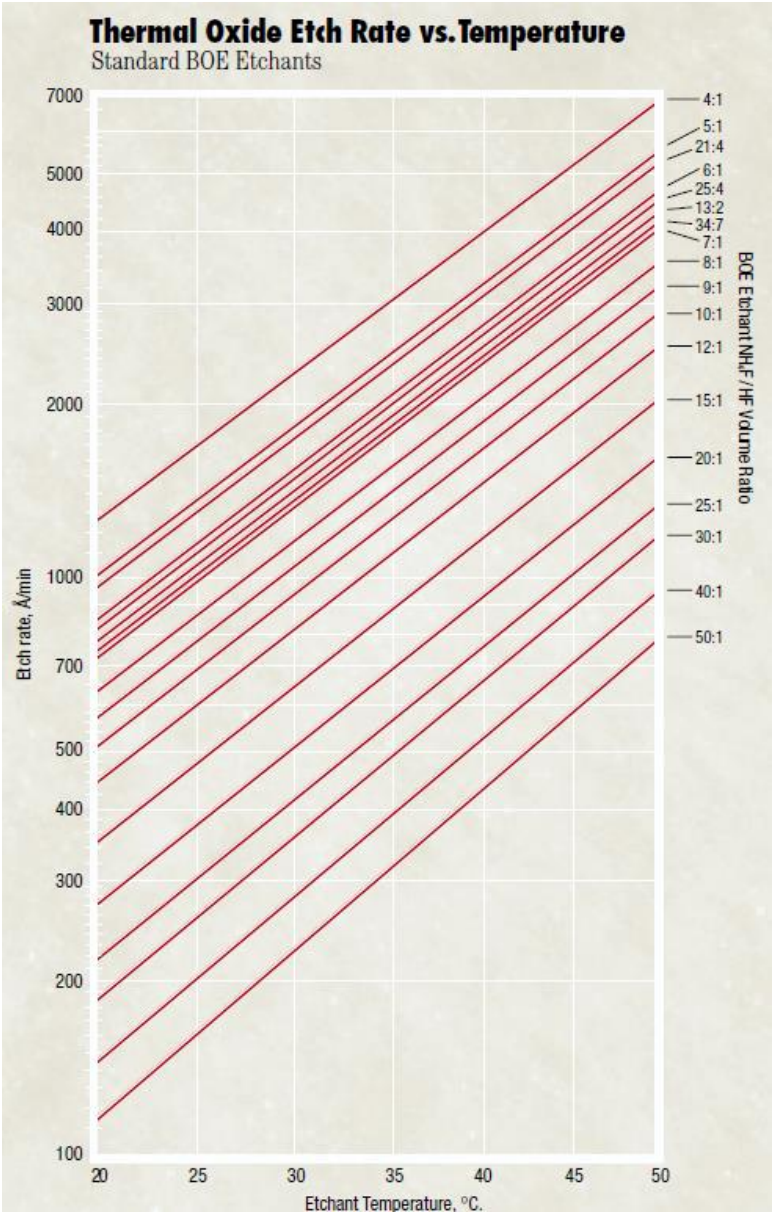

Figure3.5 : The etch rate (Å/min) of different range of BHF acid concentrations versus different etchant temperatures (°C)[100].

In order to check the repeatability of the etch rate of the used BHF acid bottle, each etch run was repeated more than three to five times. Figure 3.8 illustrates the measured data of the thinned (etched) cladding diameter versus the time of each etching process per hour for both containers, the first and second, and for different bottles of BHF solution acid. For the 1st bottle and first container was used, it is obvious that the measured thinned cladding with the etching time is a linear trend, exhibiting an etching rate ≈4.6 ±0.05 µm/hour. Moreover, the period time run of the etching process that has been accomplished for that slope was from 3 hours of etch run to almost 25 hours.

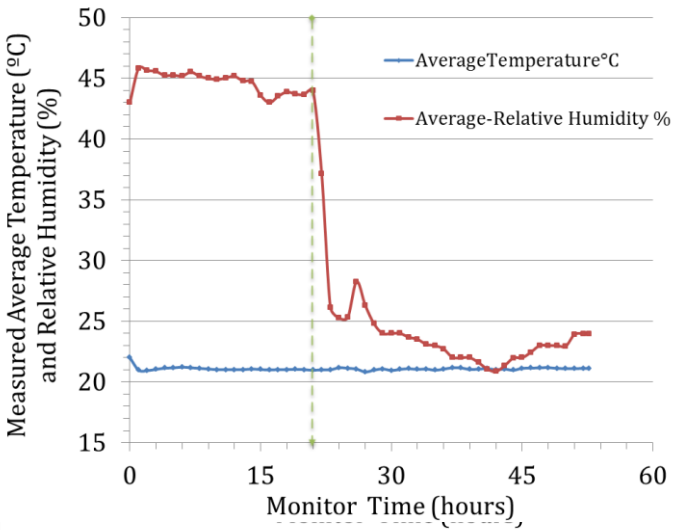

Figure 3.6: Averaged measured relative humidity (%) and temperature (°C) data in the clean-room (acid-wet bench) during the etching process of SMF-28 fibre using BHF acid with concentration (20:1) for 53 hours continuously within 3days.

On the other hand, the second container and 2nd bottle of BHF acid was used, and several runs of etching for the same fibre SMF-28 resulted in a decrease in the slope of the rate of reduction of fibre diameter per hour to be ≈ 4.5 ±0.1 µm/hour, as shown in Figure 3.8. In addition, the second container has given us the ability to produce a thinner diameter of cladding from the last results to reach a thickness of about 8.7±0.5µm as shown in Figure 3.4 c, d.

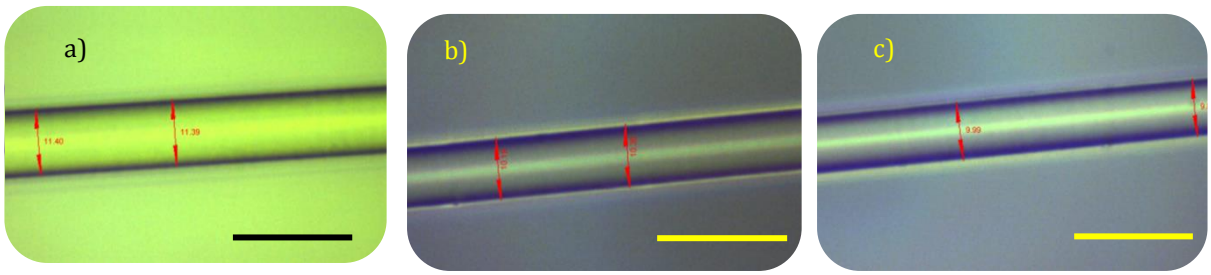

Figure 3.8: Number of etched SMF-28 samples by BHF Acid with concentration (7:1) and using the second container. a) D~11.3±0. 5µm. b) D~10.2±0.5µm. c) D~9.8±0.5µm.

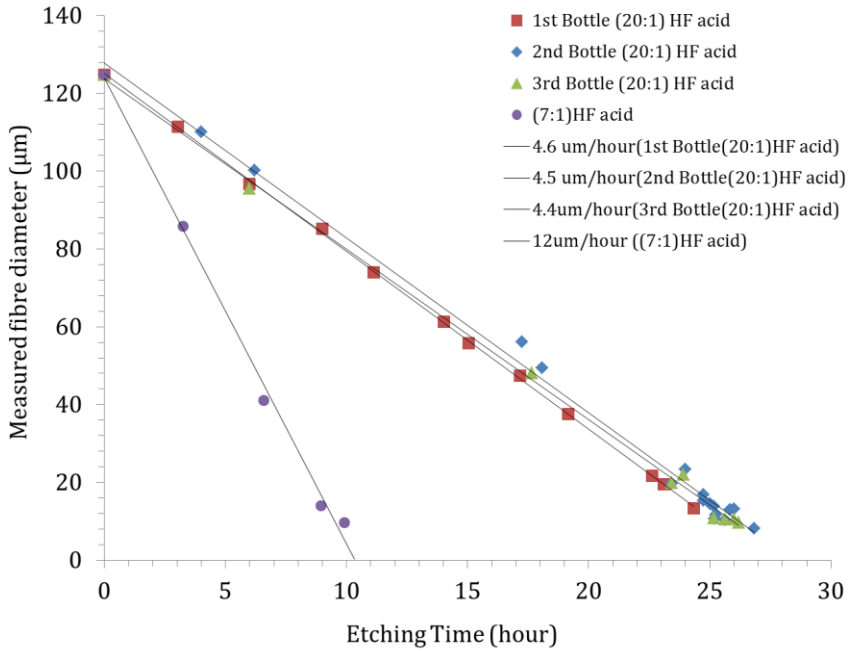

Figure3.9: Measured diameters of etched cladding fibre vs. the etching time for both used container first and second and different bottles of BHF acid solution and both concentrations (20:1) and (7:1).

Finally, here we used another concentration of BHF acid solution with concentration (7:1) in the etching process of SMF-28 fibre samples (as mentioned in section 3.3).Figure 3.7 shows number of different thickness of the resulted etched of SMF-28 fibre samples by BHF acid with concentration (7:1). the resulted etch data at the end of each etching process using BHF acid with concentration (7:1) was optimised and the slope of the rate of reduction of fibre diameter of this concentration was analysed to be about ~12±0.2µm/hour as shown in Figure 3.8. As mentioned, this concentration of BHF acid has reduced the time of etching yet is not efficient in terms of the transition regions of the etched fibre samples (later to be discussed in the next section) due to the policy of the limited working time hours of the cleanroom facility. Hence, for a thinner diameter, the etch process was done in two stages within two days which consumed the same time as with the concentration (20:1) of BHF acid solution. At

the end of the first stage of etch run, the etch process stopped and the mounted fibre samples in the container were immersed in DI-water instead of BHF acid (7:1) until next day, then the etch process was commenced again (the second stage of etch process) to reach the targeted etched fibre diameter. This was not efficient BHF acid concentration for our work, in specific ,if the targeted etched fibre diameter was less than 16.0μm since it required (estimation based on the speed of the etch rate ~12±0.2μm/hour) more than 9hours of continuous etch run of the fibre samples. However, the quality of the etched fibre cladding still shows a uniform, smooth and robustness etched surface.

3.3.2 Optical Loss Characterisation of The Etched Fibre Optic

Most of the etched optical fibre samples from the first stage were characterised by measuring the insertion loss against the etched cladding diameter.

In the first step, both the non-engraved ends of the etched optical fibre samples were cleaved by (Fujikura CT-04 cleaver) and cleaned by using Isopropanol solvent. The cleaned cleaved fibre ends were spliced using a fusion splicer (Ericsson FSU 925), to another standard optical fibre (SMF-28) connector followed by fused splicer protector to cover the fused spliced section. The range of splicing losses was about 0.03±0.01dB.

Furthermore, an optical experiment setup was prepared to evaluate the losses through the etched optical fibre. Figure 3.9 depicts the optical experiment setup. In the experiment, we used a Fabry-Perot (FP) laser as an input light source launched into the etched fibre (device under test(DUT)) with a wavelength about 1549.750 nm and input power P_{input}=-1.30dBm (I=45mA).

On the other side of the setup, an optical power-meter (Anritsu -ML9001A) was utilised to measure the output power. The surrounding medium of the etched fibre section was air (n=1) in the all cases. The optical experiment setup was applied to most of the etched samples resulted by using the first and second containers with a different run time of etching process.

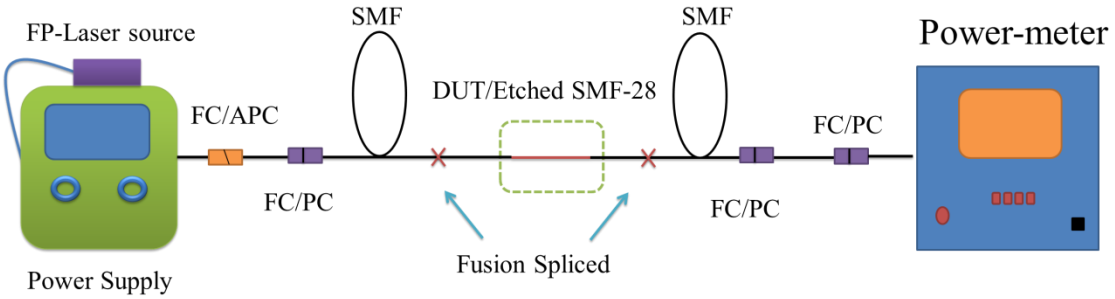

Figure3.10: The experimental setup for characterisation the etched SMF-28 samples by using BHF acid with concentration (20:1).

The etched fibre samples resulted from the etch run by using BHF acid with concentration (7:1), were also characterised using the same procedure as above. Both the normal ends of the etched samples were spliced to pigtail connectors (SMF-28) within splice losses ~0.04±0.01dB. In this experimental setup for analysing the insertion losses of these etched samples, we used an amplified spontaneous emission (ASE) broadband source instead of FP laser source and launched to the DUT, due to that the FP laser was not available to use it, as shown in Figure 3.10. The output power was measured by using a power meter (Anritsu - ML9001A). Adding to that, we characterised the rest of the resulted etched SMF-28 fibre samples by using the same setup shown in Figure 3.10 since unavailability of the light source used in Figure 3.9, the FP-laser.

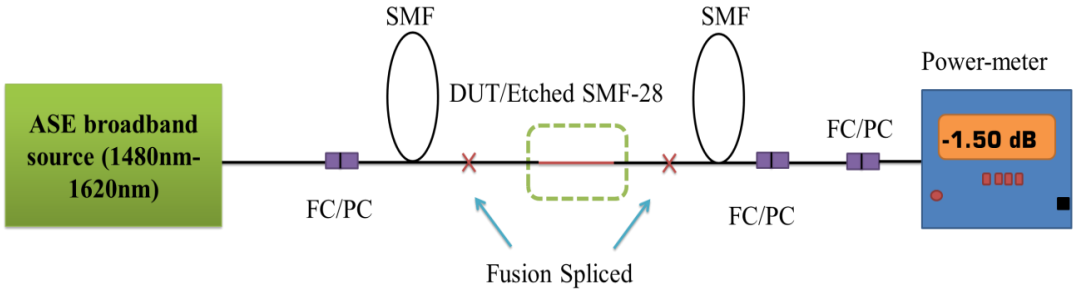

Figure3.11: The experimental setup for characterisation of the etched SMF-28 samples etched by using BHF acid with both concentrations (20:1) and (7:1).

3.3.2.1 Results & Discussion

Figure 3.11 summarizes the resulted insertion loss obtained by optimising the etched SMF-28 fibre samples with different diameters and for both BHF acid concentrations (20:1) and (7:1). In the early stages of the etching process, when SMF-28 diameter = 125μm, it showed an insertion loss ≈ 0.02 dB resulted from the two-spliced bare fibre ends to the pigtails connectors(SMF-28), besides the normal insertion loss of SMF-28 fibre. The insertion loss shows a gradual increase to ~0.8 dB at diameter ≈61.0μm. Thus, it is obvious that the insertion loss of the optical power fluctuated with the variation of the cladding diameter.

From our resulted etched fibre samples of SMF-28, at the stage when the etched fibre diameter around 13.5μm, it can be noticed that the optical losses escalated to ≈ 1.2 ± 0.2dB which we believe some are as a result of thinning the fibre diameter, in parallel, leads to the change in the effective mode index of the fibre (n_{eff}). As a result, the NA of the thinned optical fibre sample has increased along with the V-number which it might reach the point to support higher-order modes (will be discussed later in more details in Chapter 5 and 6). Subsequently, the propagating mode has risen leading the fundamental mode to be more confined in the core. On the other side, that has led to an increase in the tail of evanescent field extending from the propagated mode in the etched fibre (very small proportion from the fundamental mode and higher proportions from the higher-order modes), and thus has contributed partially in optical loss in the transmitted light. Besides, the average insertion loss was obtained is around 0.8 ± 0.2dB. From the experimental point of view, we did not anticipate a noticeable insertion loss at etched fibre samples with diameters >15μm from this experiment. Although that's what has been shown, but that is not the case because the following other factors that possibly could have strongly contributed to it, are:

1- The probability of etched fibre samples had been accumulated with some dirt while running the experiment which led to cause these losses for the etched fibre > 15μm; in specific the transition regions on both side of the etched section in the etched fibres as it surrounded by the jacket coating and it was quite hard to clean that area from any residuals or dirt remained after the etching process (as shown in Figure 3.12), and
2- Losses that were obtained, as mentioned above, from the used equipment (FP-laser, OSA), the connectors that were employed, splicing losses, the way of mounting the etched fibre during the characterising experimental setup and the bending losses of the etched fibre.

Furthermore, two materials with different refractive indices were applied to the etched fibre samples resulted from BHF acid with concentration (20:1) , to optimise and characterise the optical loss depending on change of the refractive index of the surrounding medium around the etched section of SMF-28 fibre samples. The first material was Isopropanol with refractive index n=1.3738 (at T=20°C and λ=1550nm), and was applied on an etched fibre sample with a diameter ≈16.5±0.5µm and insertion loss 1.3 ± 0.2dB (before apply the Isopropanol) at n=1 (air and λ=1550nm). The etched fibre area that was dipped in the solvent caused a very slight increase of the insertion loss to be 1.60dB±0.02dB (increase by ~ 0.3dB).

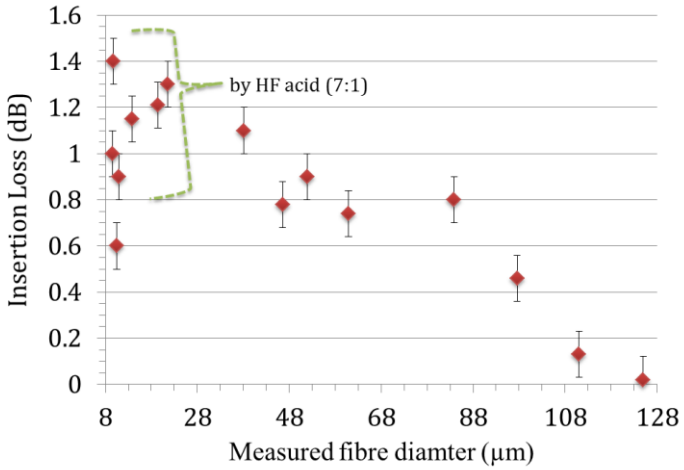

Figure3.12: Insertion loss of the characterised measured etched fibre diameter samples of SMF-28 (µm) resulted from etching process by using BHF acid with both concentrations (20:1) and (7:1).

In contrast, the second material, a machine oil with a higher refractive index n=1.49 (at λ=1550nm) (> n_{core}), was applied on the same sample used before, caused a significant upsurge of the insertion loss to be 11.20±0.2dB. These increases in losses were because of coupling out the propagating mode from core to the etched cladding of the fibre as extended tail of evanescent field which it is highly sensitive to any increase in the surrounding refractive index, in term of both the fundamental mode and higher-order modes [102]. Hence, for surrounding refractive indices higher than that of silica-cladding of the fibre ($n_{cladding}$=1.444), the propagated core mode is more likely to expand into the cladding. Besides, the rate of evanescent field extended causing some of it to leak out inducing optical losses in the transmitted mode with the fibre.

In the case of using the BHF acid with concentration (7:1), it was observed from the resulted etched fibres that their insertion loss after characterisations were increased to higher than the insertion loss of etched fibre samples via the BHF acid with concentration (20:1). Figures 3.12a and b show the difference of transition region of etched fibre of SMF-28 via BHF acid

using two different concentrations (20:1) and (7:1) respectively. The BHF acid with concentrations (7:1) takes less time (higher etching rate of silica fibre). The resulted etched fibres featured with efficient optical quality and robustness fibre structure. However, each etch process was done on two stages within two days roughly for targeted diameter < 16µm, due to the policy and limitation of working hours at the cleanroom facility (explained before in section 3.3.1), although the resulted etched fibre samples of SMF-28 with high smooth surface, maintained geometry and robustness. Accordingly, it rapidly formed two transition regions on both sides of the etched fibre section or the waist region which generated a high insertion loss up to 1.7 dB of the etched fibre because of the propagating mode coupling sharply between the core and cladding modes (as shown in Figure 3.12b). Adding to that, the aforementioned effects resulted in a noticeable insertion optical loss in the etched fibre samples.

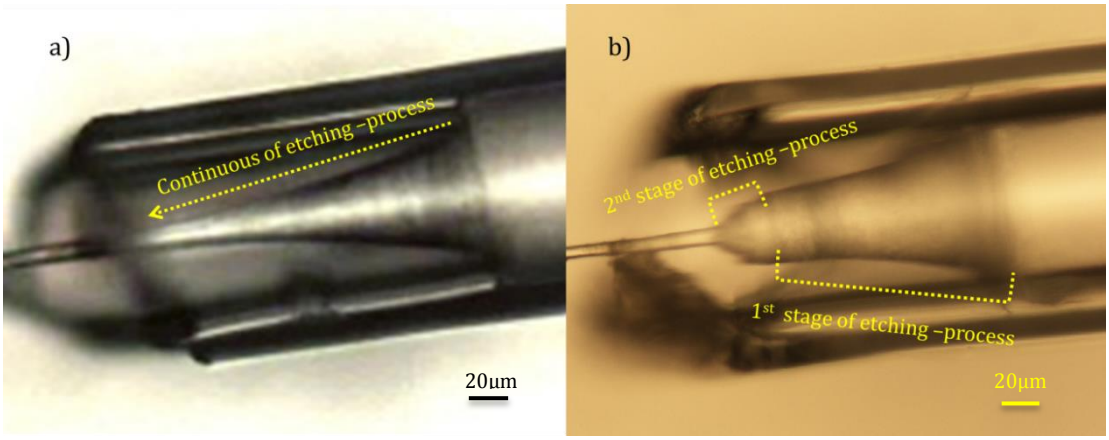

Figure3.13 : Etched SMF-28 fibre using BHF acid with; a) concentration (20:1) and has a uniform continuous transition region (D_{fibre}=10.0±0.5µm). b) Concentration (7:1) exhibiting the two generated transition regions after the end of the etch process (D_{fibre}=9.5±0.5µm).

3.4 Real-Time Monitoring of Etching Process

An experiment on two standard optical fibres of SMF-28 and a uniform FBG was conducted in a real-monitoring etching process via BHF acid with concentration (20:1) with the purpose of observing the variation of the optical transmission spectrum losses with respect to both etching time and thinned fibre cladding diameter. The experiment was done for more than 26hours of continuous etching process with in-situ monitoring of the output spectrum of both fibre samples (bare SMF-28 and uniform-FBG). In this section, the two samples will be introduced individually besides their results.

3.4.1 Etched Single Mode Fibre SMF-28

In this experiment, a single mode fibre was monitored beside to a uniform FBG (will be introduced in section 3.4.2) during the etching process in order to measure the variation of the optical power loss, in-situ. An identical sample of SMF-28 employed in this experiment with the same preparation that was described previously in Section 3.3, by using the second container which was altered for ease of handling, and the purpose of preventing the samples from bending or breaking up during the etching process. Following that, the fibre sample of SMF-28 and FBG were etched by using the same acid solution BHF acid with concentration (20:1).

Figure 3.13 depicts the experimental setup for a real-time monitoring of etching process of SMF-28 fibre and FBG sample by using BHF acid with concentration (20:1). It comprises a broadband source of ASE (1480nm-1620nm) and input power of 16dBm, a 3dB coupler has been employed with the intention of launching the light source into the two samples of fibre, a standard SMF-28 fibre and an FBG. In addition, a power meter (Anritsu -ML9001A) was used to measure the output light power for the SMF-28 fibre sample during the etching process, and an OSA (Ando-AQ63170) was also used to monitor the transmitted/reflected spectrum of the FBG sample. The conditions during the etching process , which it took long about 26hours and 30mins (continuous etching process left in the cleanroom for overnight until next day),have been controlled to be under stable average temperature and relative humidity rate of 21^{o}C ± 0.5^{o}C and 45%±5%, respectively. Furthermore, we follow the same procedure as mentioned earlier after finishing the etching process to clean the etched fibre sample from any BHF acid residuals as well as the container.

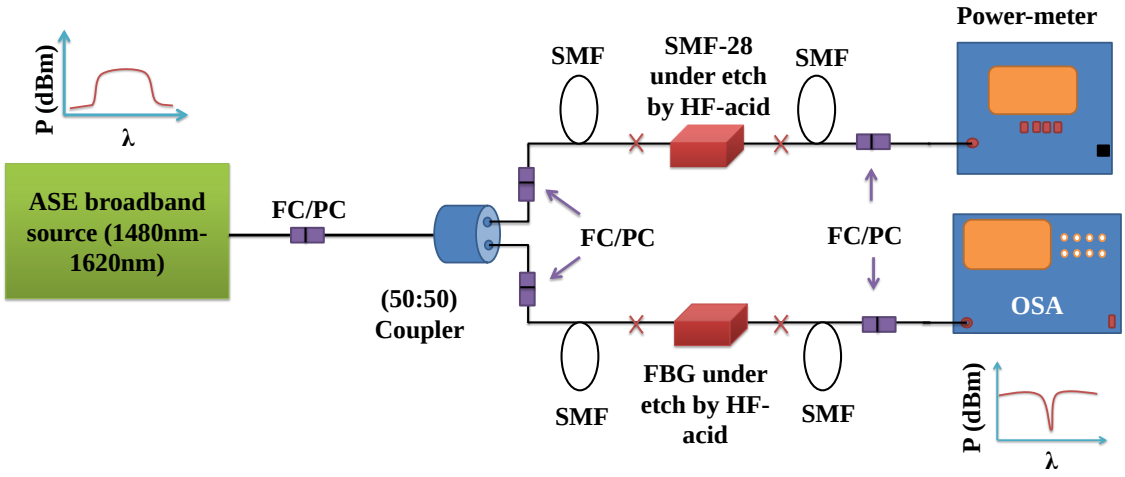

Figure 3**3.14**: The experimental setup of real-time monitoring of etching process for two optical fibre samples SMF-28 and FBG (λ_B=1533.14nm) by using BHF acid with concentration (20:1).

3.4.1.1 Results & Discussion

Initially, by utilizing the power-meter (Anritsu-ML9001A), the transmitted power was found to be 10.50 dBm through bare SMF-28 while it was mounted in the container and before commencing the etching process by the BHF acid solution with concentration (20:1). Figure 3.14illustrates the measured data of the transmitted power against the calculated etched cladding diameter (based on the reducation rate in fibre diameter during the etching process ~4.5±0.1µm/hour) in the real-time monitoring process.

It noticed that the stable trend of the transmission power losses at the early stages of etching is around 0.0 ± 0.05dB as we are still far from observing any noticeable losses due to the diameter of the fibre is still large. After 25 hours of etching (D_{fibre} ≈ 12.5±0.5µm), an increase of the transmitted power losses was observed. Whereas, the losses increased to 1.7±0.2dB (from the dashed green-line at Figure 3.14) after 26 hours and 30 minutes of etching (D_{fibre} ≈ 6.0±0.5µm, i.e. within the fibre core). Then, we kept etching the fibre until we approached the core area and the power kept on dropping and getting higher optical loss until we lost the transmission signal because the fibre sample broke.

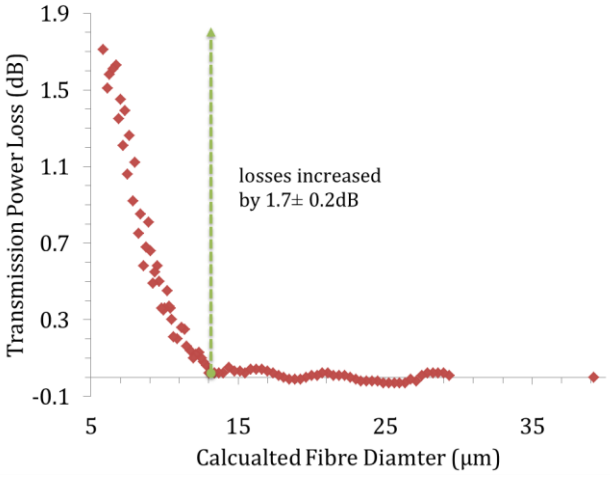

Figure 3.15: Measured transmission power loss variation in-real time monitoring with the calculated diameter of SMF-28 based on the reduction rate in fibre diameter during the etching process (4.5±0.1µm/hour) by using BHF acid with concentration (20:1).

The achieved results from this real-time monitoring of the etching process have, to some extent, matched with what we expected and from another perspective checked out the achieved results in Section 3.4.1. As we mentioned before, because of the reduction of fibre diameter, the n_{eff} of the thinned SMF-28 fibre sample is change and hence corresponding parameters values of NA, V-number and the normalized propagation constant *b* of the etched fibre will be different from that of the pristine fibre, where NA and V-number followed by the value of *b* will be increased, hence the etched SMF-28 will start to support the higher-order modes beside the fundamental mode (as shown in Figure 3.15a and b). In this case, the propagating mode becomes more confined inside the fibre core as we can notice from Figure 3.15b when the fundamental mode in the fibre core of SMF-28 starts to exceed the $V_{cut\text{-}off}$ value (>2.405), the power fraction P_{core}/P starts to increase gradually in opposite to the power fraction in the cladding of the fibre $P_{cladding}/P$. On the other side, the tail of the evanescent wave will be extended from the etched silica-cladding of the fibre into the outer surrounding medium resulted from the excited higher-order modes that contributed partially as insertion optical loss in the output power (Figure 3.15b) as the propagating mode within the etched SMF-28 fibre will be distributed between the fundamental mode and higher-order modes. It is worth indicating that some of the values of the insertion loss in etched fibre that was obtained from the evanescent wave will depend on the refractive index of the outer surrounding medium (as will be explained later in Chapter 5). Thus, in order to approach an efficient evanescent wave that would overlap with the coated materials to fabricate MFPD, we needed to reduce the fibre diameter to < 15µm while maintaining the lowest losses.

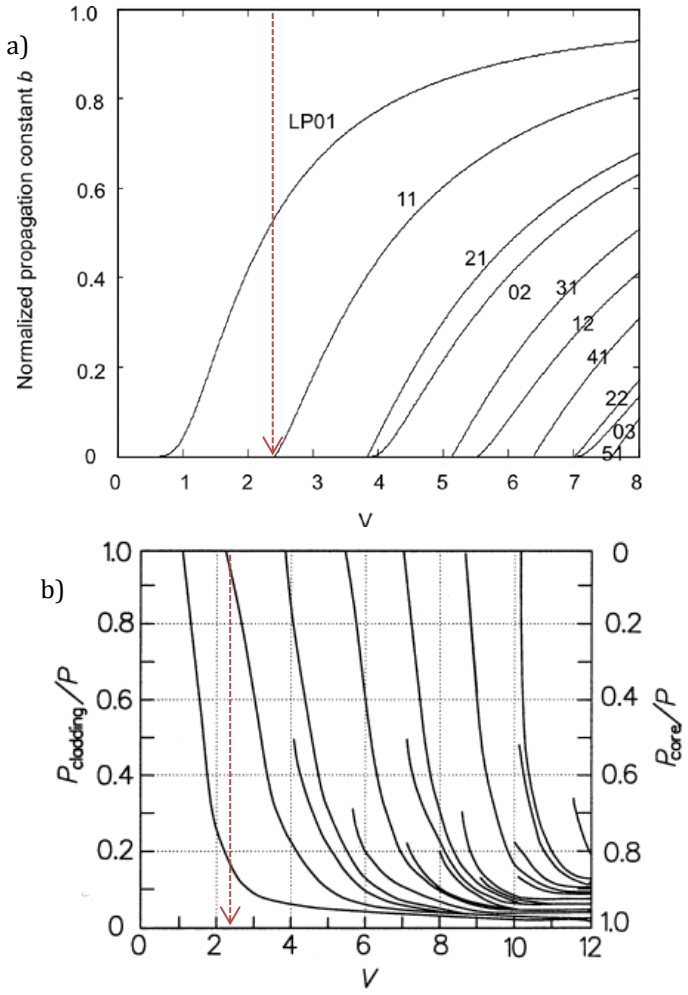

Figure3.16: a) The normalized propagation constant *b* versus the V number of the fundamental mode and higher-order modes of the optical fibre [103] b) the power fraction at the cladding fibre (left-axis) and the core of the fibre (right-axis) versus the V-number for the fundamental mode and higher-order modes of the optical fibre[104].

3.4.2 Etched Fibre Bragg Gratings

As we mentioned above an experimental work of real-time monitoring of continuous etching process for both two fibre samples in the same time; SMF-28 fibre and a uniform FBG sample was done. In this section, we will first investigate the effect of reducing cladding diameter of an FBG with the shift of Bragg wavelength by etching process via BHF acid with concentration (20:1). The applied FBG was a uniform UV-written grating in a single mode fibre SMF-28. As a first step, The FBG-sample was cleaved and accurately connected to pigtails connectors of SMF-28 with an average splice loss of 0. 04dB. Then, by using the OSA (Ando AQ63170), the transmitted spectrum of the uniform FBG sample was monitored (span=10nm, resolution=0.05nm) by recording the shift in the Bragg wavelength λ_B = 1553.140 nm, grating length L_g= 2.4mm, a transmission loss of 3.4dB, and a full bandwidth of $\Delta\lambda_B$ = 0.85nm

as shown in Figure 3.12. Then, the FBG sample was mounted in the etching container, using the same previous experimental setup as shown in Figure 3.10. The FBG sample as well as the bare SMF-28 sample, were launched by 12.0dBm as an input power provided from the ASE source through a 3dB-coupler aforementioned. Moreover, by using the OSA, the variation of the transmission spectrum of the FBG-sample was in real-time monitoring during the etching process. At the beginning of the experiment, the transmitted spectrum of the FBG sample was recorded. Subsequently, after 21 hours of etching, the transmission spectrum was recorded every 5 minutes, followed by every 2-3 minutes in the final stages with the intention to record each single change in the transmission spectrum. Furthermore, the FBG sample and the SMF-28 sample were etched for about 26 hours and 30 minutes.

3.4.2.1 Results and Discussion

Figure 3.16 exhibits real-time monitoring of the transmission spectra of the FBG sample during the etching process via BHF acid with concentration (20:1) and the change of Bragg wavelength from the start to the end time of etching process experiment. The transmitted spectra of the FBG sample from no. 2 until no.10 represents the recorded data from 21 hours until 26 hours and 30 minutes of etching process, respectively, and the calculated thickness of the etched FBG sample (based on the etching rate of 4.5±0.1μm/hour), for the reason that in the early stages of the etching process, the transmission spectrum of the FBG-sample did not show any obvious changes. Each transmission spectrum has different calculated thickness of the etched FBG sample during the etching process as shown in Figure 3.16 (right legend).

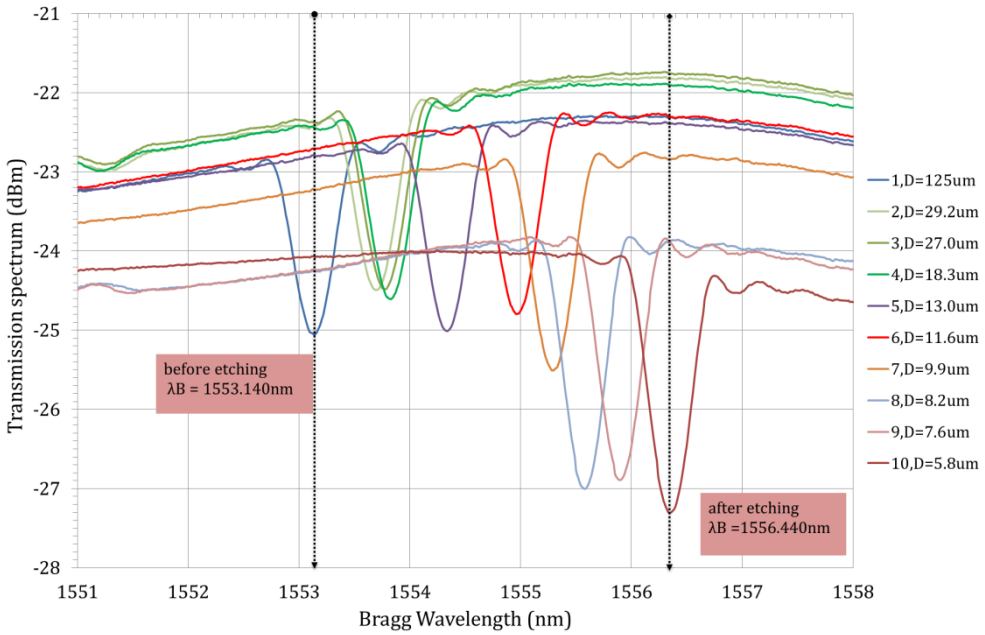

Figure3.17: The transmission spectra evolution of the FBG-sample (λ_B=1533.14nm) before etch process (no.1) and during the etching process by BHF acid with concentration (20:1) showing the shift of the Bragg wavelength (no. 2, 3 4, 5 , 6, 7, 8, 9, 10).

As observed from the transmitted spectra dropped gradually until the end of the experiment and caused an average losses of 1.7±0.2dB, similar to the average optical losses in the etched SMF-28 fibre. These losses resulted as we had explained earlier in Section 3.4.1 from the effect of reducing the fibre diameter to a few microns, in increasing the values of NA and the V-number of the etched fibre subsequently and this will be corresponding to the propagated fundamental mode to be more confined within the fibre core from a side (as shown in Figure 3.15). From another perspective, the evanescent wave will be extending to the surrounding refractive index [43].

In addition, it can be seen that the transmission spectra references in Figure 3.16 dropped by 0.5 ± 0.2dB between fibre diameter 27µm-13.0µm, which could be attributed to the imperfect arrangement of the container cover and due to several times of checking the level of the BHF solution with concentration (20:1), if it was dropped lower than the level of the mounted fibre samples in the container.

Though in Figure 3.17 the reflectivity of the FBG showed a stable trend with an average reflectivity 0.4±0.02 followed by a growth about 12% started from the same calculated $D_{fibre} \approx$ 13±0.5μm, this was expected due to the increase of confinement rate Γ (as shown in Figure 3.15a) of the fundamental mode in the FBG core. This led to an increase in the coupling coefficient Ω (shown in Figure 3.15b), and subsequently the reflectivity peak of the FBG as is described in Eq. (2.14) and (2.15) in Chapter 2.

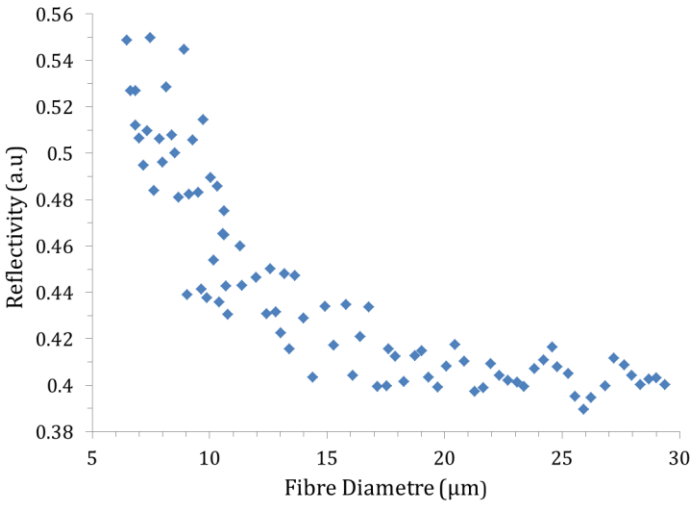

Figure3.18: The reflectivity evolution of the etched FBG-sample (λ_B=1533.14nm) during the etching process vs. calculated fibre diameter (based on etch rate 4.5±0.1μm/hour).

On the other side, the Bragg wavelength shifted toward a longer wavelength (red wavelength shift) about 3.3 nm, from its initial central wavelength of 1553.140nm to 1556.441nm as shown in Figure 3.19. Where the effective refractive index n_{eff} of the fundamental mode due to the reduction of the thickness of the FBG cladding diameter uniformly and subsequently the Bragg wavelength exhibited a shift towards longer wavelength range (based on Eq. 2.11 in Chapter 2) since the surrounding refractive index (SRI) is BHF acid with concentration (20:1) ~1.360 (will be determined later in Chapter 6), lower than the fused silica cladding ($n_{cladding}$=1.444), which was opposite to the numerical anticipation[22, 43]. Adding to that, previous reports also claimed the tendency of red shift of Bragg wavlength in etched FBG by HF acid, it was not even similar to their numerical anticipations and it was reported that is resulted either from the exothermic properties from the chemical reaction between the high concentration HF(40%-13%) and the FBG or the contribution of non-adjustable setup of the FBG caused a rise of strain effects along the weak etched area [21, 22, 105]. However, we used a very low concentration of BHF acid (5%) or (20:1) in our experiment but we still expected to observe this effect of longer wavelength shift. We repeated the experiment with

another FBG sample (λ_B=1533.1nm) to obtain the same trend of red shift of Bragg wavelength (from 1533.15nm to 1533.4nm) during the etching process (from 22hour to25hour) then it dropped towards shorter wavelength shift (from 1533.4nm to 1533.34nm) then we lost the FBG sample signal as it broke at the end of the etching process, as shown in Figure 3.18.

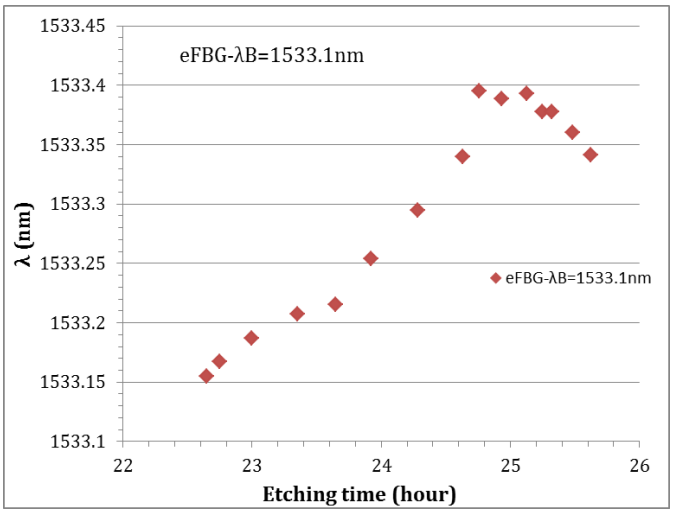

Figure3.19: The measured Bragg wavelength shift of another etched FBG-sample (λ_B=1533.14nm) during the etching process by BHF acid (20:1) as a function of etching time.

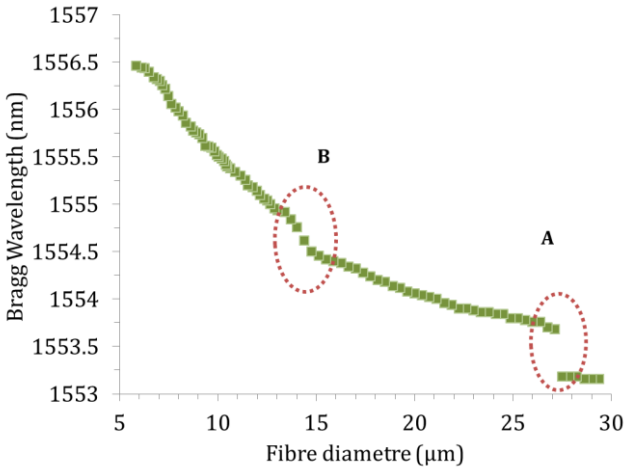

Figure3.20: The measured Bragg wavelength of FBG-sample (1553.14nm) variation against the fibre diameter (calculated based on 4.5±0.1µm/hour).

Moreover, the sudden growth of Bragg wavelength shift in area A represented in Figure 3.19 is attributed to checking the level of the BHF solution acid and was filled as we lifted and put back the container cover. Whereas, area B has shown a slight rise in the wavelength shift from 1554.5nm to 1554.7nm at thickness ≈15.0μm because the core is not anymore well bonded by a thick layer of cladding and became more sensitive to the SRI, and we are more interested in within that range of fibre diameter, as will be described later in Chapter 5 and 6.

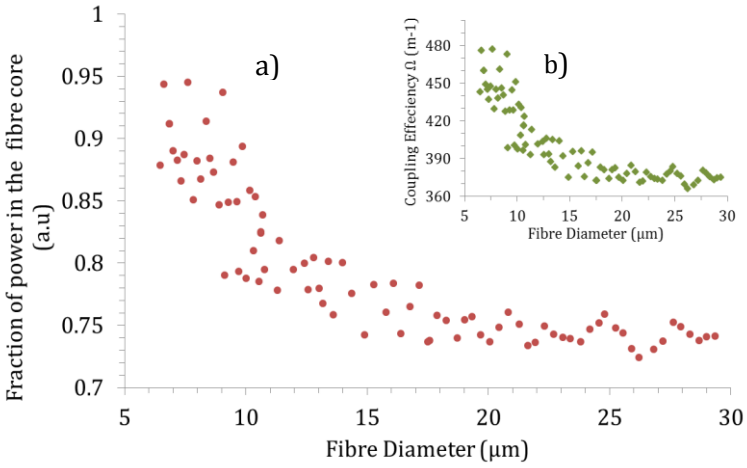

Figure3.21: The effect of reducing diameter of FBG for; a) The evolution fraction of fundamental mode power in core of the etched FBG and b) The change of coupling efficiency of the etched FBG.

Furthermore, Figure 3.20 represents the fraction of the propagated mode in the core variation in relation to the thinned cladding diameter of the etched FBG sample (1553.140nm). As we expected and discussed above, it can be seen how the fraction of the propagated mode grew up gradually from ≈ 0.75 to ≈0.95 after D_{fibre} < 15μm. Finally, it is worth mentioning that figure3.20 a, b have been calculated numerically based on Eq. 2.15 and Eq. 2.14 in Chapter 2; as the reflectivity was measured experimentally from the experimental data as shown in Figure 3.17 then the coupling efficiency Ω was calculated numerically based on Eq. 2.15 as follow;

$$\Omega = \frac{tanh^{-1}\sqrt{R}}{Lg} \tag{3.2}$$

the FBG has Lg= 2.4mm followed by that calculating numerically the fraction of power in the etched FBG core based on Eq. 2.14 as follow;

$$\Gamma = \frac{\Omega\lambda_B}{\pi\Delta n} \tag{3.3}$$

Where the Δn of the FBG written in SMF-28 fibre ~0.0025 and the λ_B measured experimentally. Furthermore, the etched FBG diameter based on the reduction rate of the fibre diameter in the etching process (4.5±0.1μm/hour) and the experimentally data obtained and recorded.

3.5 Characterisation The Effect of Thinned FBG Versus Different SRIs

This section explores the effect of applying different solutions of SRIs on Bragg wavelength of an etched grated fibre. There have been many investigations reported about the Bragg wavelength shift in a thinned silica-cladding FBG treated with different index coatings [30, 36, 106]. In the first stage, before the etching run, we characterized the uniform FBG sample UV-written in SMF-28 fibre, by splicing it with two pigtailed connectors with an average splice loss of 0.05dBm. An ASE source (1480nm-1620nm) is used to launch light source through the FBG-sample. An OSA (Advantest-Q8384) with a resolution of 0.02nm is used for the spectral characterisation of the gratings. The output transmission spectrum shows that the central wavelength of the grating is λ_B=1544.390nm with a transmission loss of 29.25 dB and a 1.92 nm full bandwidth (as shown in Figure 3.21). Note that this experiment of FBG and its characterization were carried out under controlled conditions of T=21±0.5°C and relative humidity of 45%±5%. Subsequently, the FBG-sample was etched via BHF acid with concentration (20:1) until the diameter thickness dropped to be about average 19.8 ± 0.5 μm (as shown in Figure 3.22a and b).

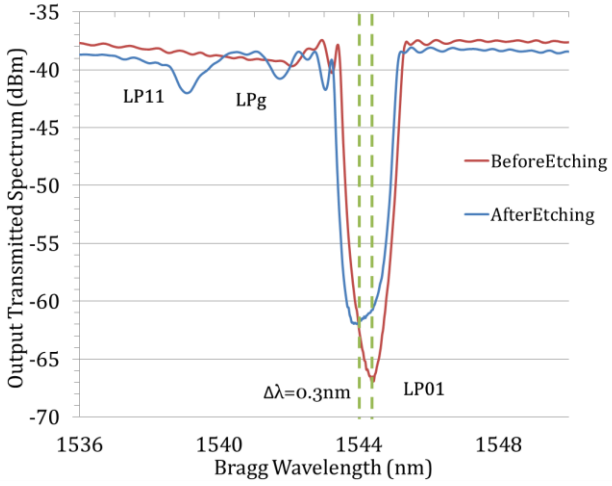

Figure3.22: the transmitted spectrum of a uniform FBG-sample (1544.390nm) before and after etching run, both surrounded by air (n=1), LPg is ghost mode and LP11 is the first order of higher-order mode generated after etching the FBG sample.

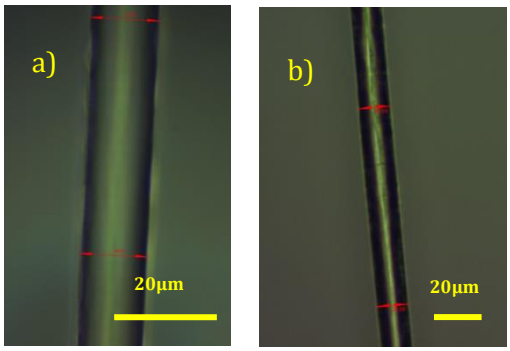

Figure3.23: A uniform etched FBG-sample by BHF acid with concentration (20:1) under microscope magnifications with D_{fibre}=19.8 ± 0.5 µm; a)50X b)20X.

Following this, the etched-FBG was characterized again to examine any changes that accrued after reducing the cladding diameter. The first observable change after etching the FBG was creation of first order of higher-order modes LP11 and ghost mode LPg due to cladding modes[107, 108] as it can be noticed in Figure 3.21(blue-line). Then, a central wavelength shift of 0.30 nm was observed. The next step was to calibrate the etched FBG as SRI sensor by immersing the etched FBG-sample in liquids of different refractive indices with the purpose of examining their effect on the Bragg wavelength and the reflected peak. We used number of labelled solvents such as; methanol, water, isopropanol, and acetone, and resulted of a wavelength shift of +0.15 nm, +0.09 nm, +0.09 nm, +0.08 nm respectively. The Bragg wavelength shifts were toward longer wavelength range (Table 3.1). Figure 3.23 shows the characterisation experimental setup of the thinned FBG-sample with different SRI solvents. Table 3.1 represents the characterisation results of applying etched uniform FBG-sample (D_{fibre}~19.8µm and after etch λ_B=1544.1nm) by BHF acid (20:1) to a number of solvents as a SRI sensor and their effect on the Bragg wavelength shift. Furthermore, the unsystematic reflected peak of the transmission spectrum of the etched FBG in Figure3.21 due to the resolution bandwidth (=0.06nm) of the OSA and the noise floor of the spectrum.

Table 3.1: The characterisation data of etched FBG-sample (D_{fibre}~19.8µm) with different SRI solvents.

SRI	λ_B (nm)	$\Delta\lambda_B$ (nm)	Transmission Loss (dB)
FBG (before etching by HF)	1544.39	-	29.25
Thinned-FBG, n_{air} =1	1544.09	-0.30	25.50
$n_{methanol}$= 1.317	1544.24	+0.15	28.25
n_{water}=1.318	1544.30	+0.09	25
n_{aceton}= 1.350	1544.30	+0.09	26.75
$n_{isopropanol}$ = 1.3738	1544.31	+0.08	28.25

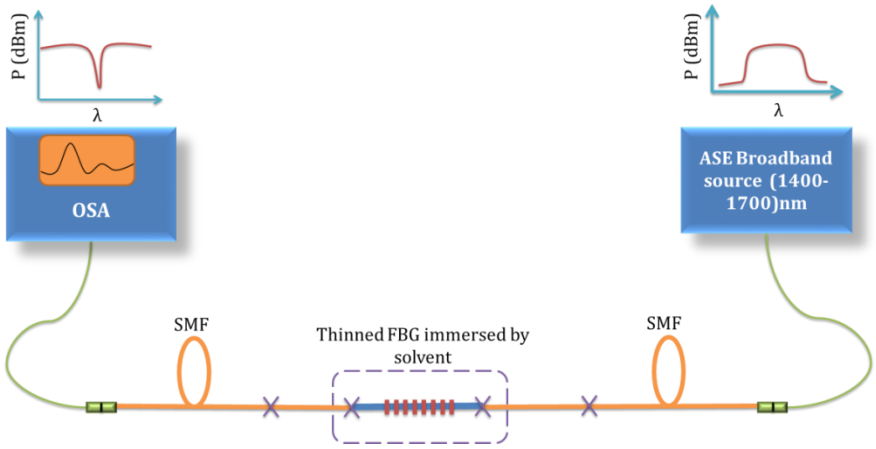

Figure3.24: Experimental setup of etched FBG (D_{fibre}~19.8µm) characterisation with different SRIs solvents.

3.5.1 Results & Discussion

Table 3.1 and Figure 3.24 both show the measured transmission spectra of the FBG-sample before and after etching process and wavelength shift when was applied to different SRIs to calibrate the sensitivity of the etched FBG for the fundamental mode, LP01 mode. It is observed that the Bragg wavelength after the end of etching process shifted to a lower wavelength range by 0.3nm, which is less than the past experiment run in Section 3.5.2. The reason of this small shift of λ_B is that the diameter of the etched FBG sample is relatively large (D_{fibre} ~19.8µm) in order to obtain a functional change in the effective mode index n_{eff} of the etched FBG sample. Hence this resulted on small amount of Bragg wavelength shift and less sensitivity to the SRIs (as it will be explained more in Chapter 5 and 6). Adding to that, that is mean that the amount of the evanescent wave extended tail outside the etched FBG sample is small that not influenced strongly by the SRIs change. Besides, from the numerical study obtained by COMSOL Multiphysics, to simulate the power fraction that is overlapping at the outer-cladding layer of etched fibre as a function of different fibre diameter and various SRIs (explored later in Chapter 5), it is believed that the evanescent wave (power fraction) that is overlapping outside the etched cladding fibre (outer-cladding) about 0.002 % (from Figure 5.6 in Chapter 5), which is a very small rate to be affected or sensitive to the SRI. For these reasons, we were not able to gain a notable shift of Bragg wavelength with the applied indices of solvents.

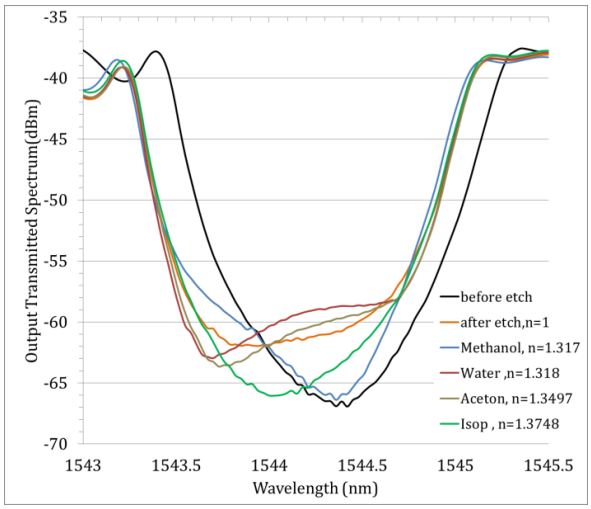

Figure3.25: The transmitted output spectra of etched FBG-sample (D_{fibre}=19.8 ± 0.5 μm) applied to different SRIs.

Figure 3.25illustrates the transmission spectra of the obtained first order of higher-order modes (LP11) in an etched FBG-sample (D_{fibre} ~19.8μm). As a result of changing the cladding diameter, as we explained before, the effective index of the propagated mode and the effective refractive index n_{eff} of the etched FBG changes to higher values in correspondence the NA , the V-number and normalised propagating constant *b* increase too of the etched FBG change, and subsequently, the fibre starts to support other higher-order modes besides the fundamental mode as illustrated in Figure 3.15 a and b (as it was explained before), where the first order of higher-order mode (LP11) has a central wavelength of 1539.0nm and the relative shift between the LP01 and LP11 showed ~5.0nm. In addition, applying solvents with different SRIs resulted in a red shift of their central wavelengths for LP11 in the range (+0.1 to +0.2) nm. Thus, we noticed that, the LP11 is more sensitive to SRI due to that the mode is with less fraction in the core compared to the fundamental mode LP01. More investigations on the generated higher order modes in etched cladding-FBGs are explained theoretically as well as experimentally in Chapters 5 and 6. We can notice another mode observed during the etching process of the grated fibre which is believed to be created within the cladding as a cladding mode or it can be called as the ghost mode LP_g [107, 108].

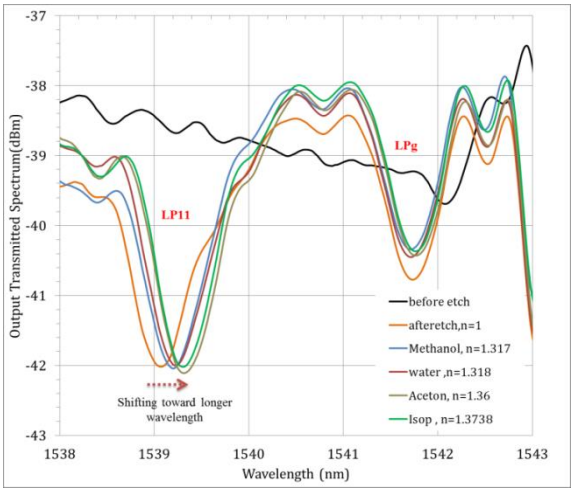

Figure 3.26: Measured transmitted spectrum of LP011 and LPg (ghost-mode) mode of etched FBG sample (D_{fibre} ~19.8µm) with different SRI

3.5 Conclusion

The main fabrication technique used to produce MF based on etching technique of the fused silica-cladding of single mode fibre was described in this chapter. Wet chemical etching process of optical fibre by using BHF acid solution with two different concentrations (20:1) and (7:1) was explained and demonstrated experimentally. The etching rate of the BHF acid for both concentrations for the reduction of silica fibre diameter was optimised to be 4.5 ±0.1 µm/hour and ~12±0.2µm/hour for (20:1) concentration and (7:1) concentration, respectively under controlled conditions. Some factors affected on the consistency of the etching rate of BHF acid for both concentrations were manged to be solved either by; enhancement the design of the container was used during the etching process, and control the environmental conditions during the etching process (i.e. temperature and relative humidity %). The fabricated etched fibres were optimized and their insertion loss for different fibre dimeters were characterised with an average of 0.8±0.2dB for BHF with concentration (20:1). In contrast, the BHF with concentration (7:1) showed a higher insertion loss of about 1.7±0.2dB due to the formation of a double transition region in the etched fibre caused by the policy working hours of the cleanroom (when we targeted etched diameter <16µm). However, the optical quality of etched surface with (7:1) was quite comparable to the BHF concentration (20:1) in terms of smooth, uniform and robustness etched fibre. The etched SMF-28 fibre were characterised the sensitivity to be immersed in low and high index (SRI) in term of optical loss and showed a high insertion optical loss at high index as a surrounding material.

An experiment on two standard optical fibres of SMF-28 and a uniform FBG was conducted in a real-monitoring etching process via BHF acid with concentration (20:1) with the purpose of

observing the variation of the optical transmission spectrum losses with respect to both etching time and thinned fibre cladding diameter. In the experiment, the results of both fibres were optimised to obtain a similar average loss for the output optical power from both fibre samples (SMF-28 and FBG (λ_B=1553.14nm)) around of 1.7±0.2dB. The real-time of the etching process for both fibre samples was done for 26hours and 30 minutes continuously resulted on estimated final etched fibre diameter ~5.8μm. The etched single mode fibre started to support higher-order modes due to reduction the thickness of the fibre diameter and in parallel the optical properties of the fibre. Based on the experimental results and numerical calculations obtained from the real-time monitoring of etching process by BHF acid (20:1), in term of the etched FBG sample (λ_B=1553.14nm), the reflectivity of the etched FBG enhanced by average 0.4±0.02 besides the rate of the power confinement of the fundamental mode in the fibre core of etched FBG increased from 0.75 to 0.95 after etched D_{fibre} <15μm. Furthermore, the Bragg wavelength of the etched FBG sample (λ_B=1553.14nm) shifted 3.3nm in the longer wavelength shift that it believed to be resulted of either from the exothermic properties from the chemical reaction between HF acid and and the FBG or the contribution of non-adjustable setup of the FBG caused a rise of strain effects along the weak etched area.

On the other hand, the effect of wet-chemical etching of silica-cladding diameter in a uniform FBG and the Bragg wavelength shift versus a number of solvents as a SRIs sensor were demonstrated and their results explained in this Chapter. The resulted etched FBG sample with D~19.8 μm showed a wavelength shift by 0.3nm in the lower wavelength range. This is due to relatively large diameter of the etched FBG and very small rate of evanescent wave to interact strongly to the applied SRIs.

Chapter 4 : Optical Deposition of CNTs on Cladding-Etched Fibre Optic

4.1 Introduction

The technique of optical deposition of CNTs on thinned fibre optic, was proposed by K. Kashiwagi and S. Yamashita, is used to deposit a CNT-dispersed solution on the exposed core region of an optical fibre from one end within optical power up to 22dBm to be used as a saturable absorber in a passively mode-locked fibre laser. They gained spectral width of 3.2nm and the output pulse the full-width at half-maximum (FWHM) was of 630 fs. The CNT-deposited fiber on its end was with insertion loss ~4.2dB[109]. Other reported on CNTS deposition around the microfibre [26, 110]which was based on thermally tapered microfibre between the range of D_{fibre}~6μm and 7μm and employed in all-fiber mode-locked ring laser. They abled to produce a pulsed laser with repetition rate of 7.3MHz and the pulse width of 829fs while the other group reported of laser of 594 fs/1.7 nJ pulses with a repetition rate of 13.3 MHz[26, 110]. There are other methods to deposit the CNTs such as spraying coatings, direct synthesising and polymer CNTs embedding however, these methods essentially require sophisticated processes, large-scale setups, and consume significant amounts of CNTs[27, 109]. Here, in terms of simplicity setup and low cost for an efficient technique for caoting a uniform layer of CNTs on the etched surface of fibre to fabricate our proposed all-optical fibre devices PMFDs, we have employed optical deposition of mixed solutions of CNTs. This method of optical deposition of CNTs empoly the interaction between the evanescent wave of guided wave (etched fibre optic) and CNTs in mixed solution which imerses the cladding-etched fibre optic completely, where the method is relying on the combination of effective optical trapping of the CNTS and heat convection effects [17, 26, 27, 110].These CNTs have been dispersed homogeneously in other materials (e.g. polymer, sodium dodecyl sulfate (SDS) mixed with water and ethanol) for the purpose of depositing or coating CNTs around the etched surface of silica cladding of the optical fibre. The CNTs are most likely to get entangled in bundles due to the Van der Waals (VdW) forces, which make it difficult to disperse the CNTs in any solvent. However, from this perspective, there are a number of solvents and surfactants that CNTs can be dispersed in with less entanglement and more homogeneity, like Dimethylformamide (DMF) and deionized water (DI-water) with SDS surfactant[111]. All of the mentioned materials will be explained later in this chapter and will be examined experimentally. Furthermore, at the end of this chapter, the PMFDs coated with CNTs will be employed experimentally in all- optical fibre nonlinear effects such as; FWM and SA and the optimised resultes will be demonstared.

4.2 Optical Deposition by DMF/CNTs Solution

In this method, we employed CNTs dispersed in a solution of DMF. The used solution, bought commercially from NanoIntegris Technologies Inc., was made from a 1 mg of SWCNTs Isonanotubes-S (95%) dispersed in 100 mL of DMF polymer solution which is believed the dispersed mixture has a refractive index ~1.4[110]. Then, we used a number of etched fibre samples of SMF-28 which were prepared as mentioned in Chapter 3, Section 3.3. The next step was to apply on these characterised ethced fibre samples a coating of CNTs around the etched silica-cladding surface. One of the drawbacks of CNTs, as mentioned above, is that it starts bundling easily and quickly after just 1 month from manufacture, even if it has been mixed with disentangling material. To prevent that, it needs to be sonicated in an ultrasonication bath for a while before applying the mixture of CNTs/DMF in the optical deposition process.

Figure 4.1 below represents the optical deposition experiment setup for the first attempt. The setup included; a tunable CW laser source (TLS) (Anritsu Tunics BT) with bandwidth 1500nm-1600nm, an isolator to reduce the undesirable feedback transmitted power within insertion loss about 0.2dB, and Erbium-doped Fibre Amplifier (EDFA) with maximum output power up to 20dBm. An optical fibre coupler of (90:10) was used to both attanuate the output high power to ower power (for the power-meter) and monitor the output power from the etched SMF-28 fibre coated with CNTs finally an optical power-meter (Anritsu-ML9001A).

First of all, the samples that were used in the first attempt were of different etched diameters (as detailed in Table 4.1). They were cleaned using Isopropanol solvent followed by a check under the microscope (NIKON-Eclipse LV150). Then they were spliced by fusion splicing (Ericsson FSU 925) to pigtailed connectors with an average splice loss of 0.03dB. The samples were then mounted in aluminium (Al) containers and kept straight in a V-groove (depth ~1mm). The TLS was tuned to a wavelength of 1550nm with an input power of 0-1dBm and subsequently amplified by the EDFA to about 16-17dBm. This power was then injected into the prepared etched samples. The transmitted power through the sample was split by using the (90:10) coupler, to allow simultaneous monitoring of the insertion loss and changes to the coating characteristics around the etched surface of fibres during the deposition process. The 10% arm with an insertion loss of more than 10 dB was connected to the optical power-meter.

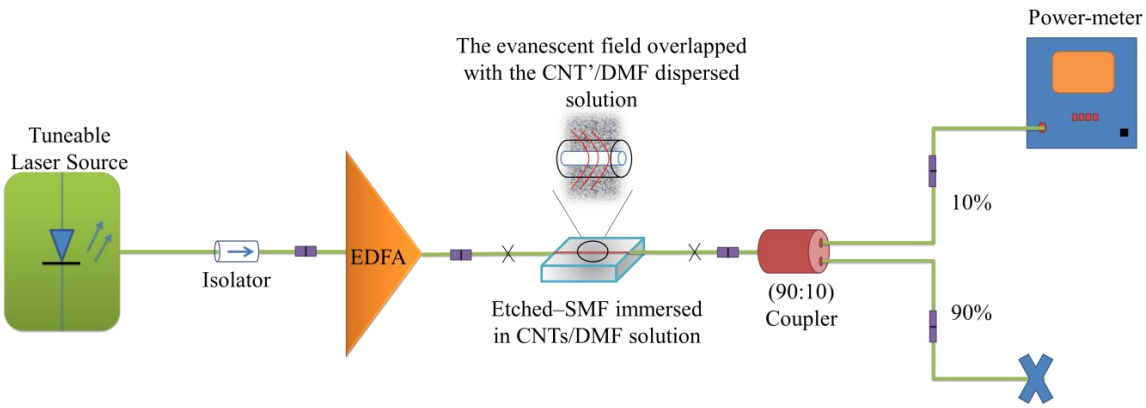

Figure 3.27: schematic of the experimental setup of the first attempt of the optical deposition of CNTs on the etched surface of SMF-28.

The CNTs that were being used in the experiment were ready dispersed in a solvent with of amount of DMF from NanoIntegris with 95% of purity, as mentioned before. The diameter of the CNTs =1.2-1.7nm, CNTs length= 300nm-5µm. This solvent was dropped on the surface of the etched samples such that they were covered completely and uniformly.

This experiment was repeated several times in the second attempt with another set of etched fibre that had different specifications of etched diameter and length; and it will be explained in detail in following Section 4.2.1.

4.2.1 Results and Discussion

We apply this method to eleventh different etched fibre diameters by BHF acid solution with concentration (20:1), the most cleaned and efficient optical quality etched surface, to investigate the optical loss in each different diameter, length of etched section, injected optical power and optical deposition time as represented in Table 4.1.

Regarding the diameter thickness of the etched fibres (shown in Table 4.1), it can be noticed that the average insertion loss (IL) of all the etched SMF-28 smaples <0.8dB before the optical depeosition of CNTs process except etched SMF-28 sample 1 (D_{fibre}~ 11.0±0.2µm) was with IL =2dB (due to factors were explained before in Chapter 3 Section 3.3.2). After optical deposition process of CNTs, in general, it is very clear that there were a drop in the output power for all the 11 samples embedded with CNTs caused mainly by light scattering and absorption loss effects induced by the deposited of CNTs[110, 112]. In the case of sample 1, showed a raise in the optical IL by about 3dB to be totla IL 5.08dB . Accordingly, this is attributed by the rate of the evanescent wave (~ 1.0% according to the numerical study that will be demonstrated in Chapter 5) propagating outside the etched silica cladding surface of sample 1, which is basically led to increase the light scattering and the abospetion rate by

the embedded CNTs. Another perespective that we examined during this process was the time of optical depeosition process, which it did not reveal on strong effect on the optical IL condition for the 11 samples in Table 4.1. For instance, the fibre samples 9 and 11, both were with similar etching thickness (D_{fibre}~19.0±0.3) and optical depositing time for about 80 mins, where both have showed different optical; IL 2.32dB and 0.51dB, respectively. In addition, sample 7 was same etching conditon with sample 8 (D_{fibre}~18.0±0.5) however sample 7 has showed higher optical IL~1.91dB for 80 mins of optical depeosition in compare with sample 8 which optically deposited for longer time about 105mnis, and resulted with less optical IL ~0.9dB. Hence, that led us to conclude that the time factor has an inconsistencey effect on the process of optical deposition of CNTs in our setup work. Furhtermore we believed that is the employed the commercial mix solution of dispersed CNTs in DMF was insufficient which is associted in not efficient coated etched fibre samples.

Table3.2:The resulted data of the first set of optical deposition process b CNTs/DMF solution on etched SMF-28 fibre smaples using BHF acid with concentration (20:1).

	Diameter (µm)	Etched length (mm)	I.L before OD (dB)	Deposition time (minutes)	I.L after OD (dB)	I.L after polymerization (dB)
1	11.0±0.2	20	2	20	5.1	4.85
2	16.0±0.5	22	0.48	20	46.34	3.61
3	16.0±0.5	22	0.13	20	60.91	6.61
4	17.0±0.5	10	0.2	94	19.69	11
5	17.0±0.5	8	0.18	-	20.50	16.50
6	17.0±0.5	8	0.2	20	1.37	-
7	18.0±0.5	10	0.76	80	1.91	-
8	18.0±0.5	10	0.29	105	0.90	3.44
9	19.0±0.3	15	0.27	80	2.32	1.07
10	19.0 ±0.3	20	0.3	20	0.56	1.03
11	19.0±0.3	15	0.2	80	0.51	-

From the point of view of the experiment, the coated etched fibre samples that resulted after the process of optical deposition of CNTs, were very lossy where in some coated fibre samples the IL exceeded 60 dB due to the interaction between the evanescent wave and the CNTs dispersed in the DMF polymer mix solution led to absorption loss and light scattering as mentioned above[110, 112]. Besides, when we tried to examine the effect of time duration of optical deposition by decreasing or increasing it, we could not infer any relation to the losses. Although we tried with sample 5 (17.0±0.5 µm) without the optical deposition and just kept it immersed in the mixed solution until it had dried completely. It also it showed a high loss rate with a very weak deposition of CNTs as was observed under the microscope. Figure 4.3 shows the etched samples of 17.0±0.5µm after it has been dispersed with CNTs without optical power and checked under the scanning electron microscope (SEM). It is believed that the high optical IL are attributed to the dried residuals of DMF polymer and a concentrated coating layer of CNTs as it was accumulated as agglomeration around one side of the etched section leading to high light scattering (as illustrated in Figure 4.3 a). Figure 4.2 illustrates how some of the deposited etched SMF-28 fibre (by BHF acid (20:1)) samples (D_{fibre}=16.0±0.5µm) by CNTs were optically checked by a handheld fibre-coupled laser source (ThorLabs-HLS635) with λ= 635nm and output power ~1mW. We can notice that the majority of the loss occurs due to the light scattering beam and coupling out from the deposited section either on the transion regions of the tched SMF-28 as it is iullstrated in Figure 4.2b and c or on the middelle of the etched section of the etched fibre samples as shown in Figure 4.2a.

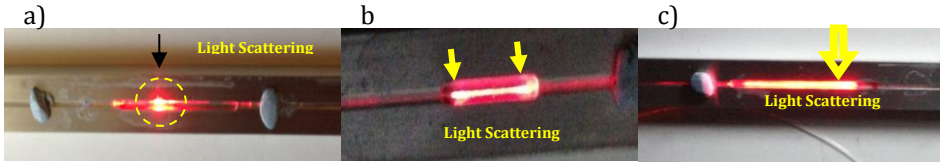

Figure 3.28: Optically deposited etched SMF-28 fibre samples (by BHF acid (20:1)) with CNTs /DMF solution launched by handheld laser source (λ=635nm, and D_{fibre} =16.0±0.5 µm).

In an attempt to reduce the losses caused by the coated layer of CNTs (n~2.4 and absorption ~1[113, 114]), we applied a low index polymer (Luvantix, pc-373) (n=1.37 @ λ= 1550nm) on the sampled devices that had been optically coated with CNTs. Using an in-situ monitoring process, we noticed a gradual decline in the losses until they settled at a minimum value, followed by curing the polymer using a UV-Lamp source (λ=320nm) for several times of beam exposure. Except for sample 8 (D_{fibre}= 18.0±0.5µm), it showed a raise in the optical IL ~3.44dB after it has been UV curied with low index polymer. It is believed is due to the generation of many air bubbles within the polymer layer near the etched surafce of fibre sample and coupling out the propagting mode as light scattering loss. Subsequently, this

significant drop in the losses as can be noticed in Table 4.1 due to minimize the effect of light scattering and coupling out of more evanescent wave (the propagating mode more likely be guided through the etched section since the refractive index of polymer=1.37 > air=1)and reduce the absorption loss from the CNTs dispersed on the etched surface of SMF-28 fibre samples[17, 26, 27, 109, 110, 112]. Some of the sample devices had not been polymerised (sample 6, 7 and 11) as the losses were already quite low within the limit of loss (<2dB). Figure 4.4 a, b, c, d, e, and f illustrate different thickness of the etched SMF-28 fibre samples that were coated by CNTs/DMF solution optically. We observed under the microscope that there were non-uniform CNTs depositions around the etched surface of the standard fibre; and where the CNTs are most likely to entangle in some areas, i.e., either the middle or on the side ends of the etched area (close to the transition region of the etched fibre) as illustrated in Figure 4.4a and b. In other cases it formed or was deposited in a periodic way along the etched section of the fibre as shown in Figure 4.4 e. On the last process run of this first attempt, we could not achieve a coated etched sample device (coated Photonic micro-fibre device) with a uniform coating or deposition around the etched surface of the fibre and with (high) optical efficiency and low loss. We believed that the thickness of the etched fibre samples had a low rate of evanescent field that could have overlapped with the mixed solution of CNTs. Moreover, optical losses due to the light scattering and absorption loss by the embedded CNTs around the etched fibre samples (as explained before)[17, 26, 110], besides the launched power into the fibre sample was not enough to interact with the CNTs dispersed solution (within the limit power lower than the thermal damage power of the microfibre and the dispersed CNTs[115]).

Later, to gain an optically efficient functioning and a uniform CNTs coating for the fibre samples and reduce the insertion optical losses of the coated fibre samples due to the reason mentioned above, we worked on optimising the assumed involved parameters mentioned below:

1- The diameter thickness of the etched cladding of the fibre sample, along with the length of the etched area, in terms of the rate of evanescent field overlapping with the CNTs/DMF solution.
2- The value of the injected power into the etched fibre optic samples.
3- Employ another mix solution of dispersed CNTs in DMF with efficient effect.

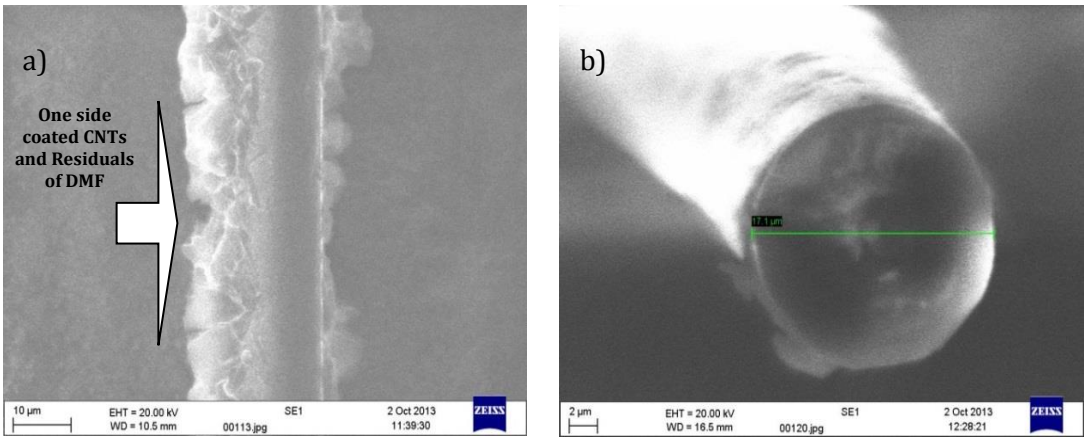

Figure3.29: Etched SMF-28 fibre optic sample (D_{fibre} =17.0±0.5µm, IL=20.5dB)) deposited with CNT's without optical power checked under the SEM a) top-side view b) cross section-side view.

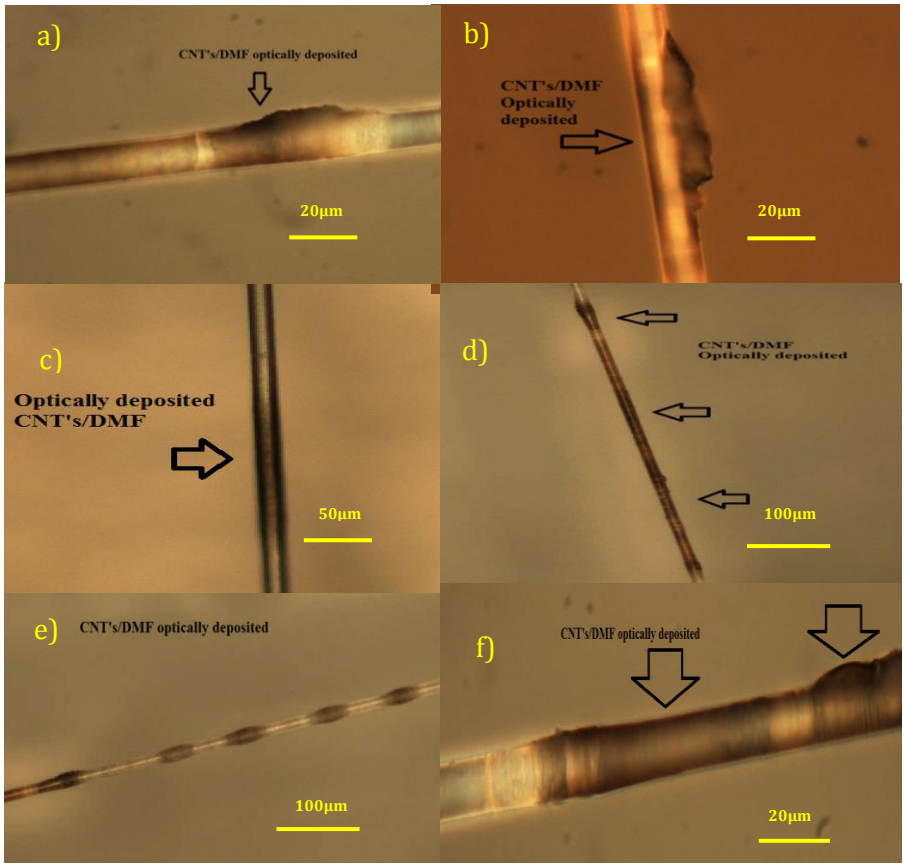

Figure 3.30: Etched SMF-28 fibre optic samples optically deposited with CNT's /DMF solution under microscope. a) sample 1, D_{fibre}= 11.0±0.5µm (IL= 5.1dB, time=20mins). b) Sample 1, D_{fibre}=11.0±0.5µm(IL= 5.1dB, time=20min). c)Sample 10, D_{fibre}=19.0±0.5µm (IL=0.56dB, time=20mins). d)Sample 2, D_{fibre}=16.0±0.5µm(IL=46.34dB, time=20mins). e) Sample 3, D_{fibre}=16.0±0.5µm (IL=60.9dB, time=20mins). f) Sample3, D_{fibre}=16.0±0.5µm (IL=60.9dB, time=20mins).

Hence, the second attempt that we made was on the etched SMF-28 fibre samples with thinner diametersBHF acid solution concentration (20:1) (as shown in Table 4.2), than the ones involved on the first attempt of the optical deposition process mentioned above (at Table 4.1). The same procedure for optical deposition (as indicated above) was implemented on the second attempt of the etched fibre samples; however, the optical experimental setup had a minor alteration. First, we applied a new commercial mixed solution of CNTs dispered in DMF with similar specifications of the above applied mixed of CNTs/DMF solution (from NanoIntegris Technologies Inc.; 1 mg of SWCNTs Isonanotubes-S (95%) dispersed in 100 mL of DMF polymer solution) that was employed at the first attempt of optical depeosition process. Figure 4.5 shows the experimental setup of the second attempt of the optical deposition process for coating etched SMF-28 fibre samples with CNTs/DMF solution. The same TLS source (Anritsu Tunics BT), isolator with IL =3dB, and two power-meters (Anritsu-ML9001A) were used in the optical experimental setup. Adding to that, in this setup we used an EDFA source with higher output power up to 30dBm and two couplers of (90:10).

Then, the same procedure steps for the optical deposition process were applied for the second batch of the etched SMF-28 fibre samples under the same method and conditions as in the first attempt, however the input power in the attempt of optical deposition of CNTS was increased to the range ~23dBm-27dBm. All were done at wavelength 1550nm; and the resulted coated etched fibre samples are detailed in Table 4.2, where it includes 8 etched SMF-28 fibre samples embedded with CNTs. Moreover, we still observed high optical IL after optical deposition of CNTs around the etched fibre samples at the second attempt , but is lower than the losses were obtained from the first process of optical deposition. Relatively, the optical IL has enhanced due to applying functional new mixed solution of CNTs/DMF (shelf-life of the solution< 3months), even though still the optical IL more than the reasonable limit of loss <3dB for sufficient PMFDs. As we explained at the first attempt, the optical IL after the deposition process of CNTs is due to the fact of light scattering from the etched fibre surface and absorption loss by the CNTs embedded on the fibre samples. Adding to that, we observed the same inconsistancey and ineffective trend in term of optical deposition time, such as sample 5 and 6 have same fibre thickness (Dfibre=13.0±0.2μm) were optically deposied with CNTS at similar time and conditions (time =23mins), nevertheless both showed different optical IL after the process about 3.56dB and 14.20dB, respectively. Furthermore, we applied the same low index polymer (Luvantix, pc-373, n=1.37), as mentioned above, to the samples with high losses resulted in a drop in the loss of most of the coated etched samples (as in Table 4.2)except sample 5 (IL=3.56dB within the loss limit).

For the reason that, as mentioned above, the effect of light scattering and coupling out of more evanescent wave were minimized since the propagating mode becomes more guided (polymer low index n=1.37>air=1) as well as the absorption loss resulted from the CNTs dispersed on the etched surface of SMF-28 fibre samples was reduced [17, 26, 27, 109, 110, 112].

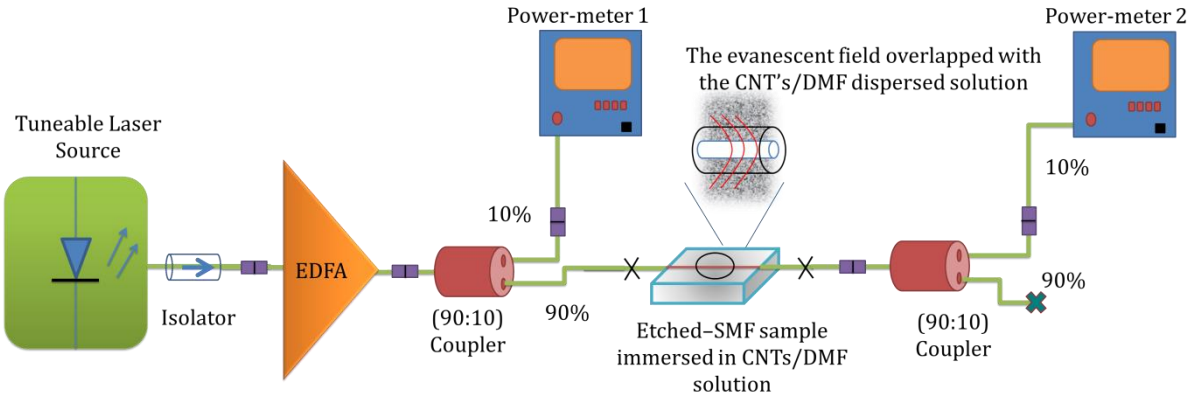

Figure 3.31: The experimental setup of the optical deposition of CNT's on the etched SMF-28 (by BHF acid (20:1)) surface fibre by using CNTs/DMF solution.

Table 3.3: The second attempt of optical deposition of CNTs on etched SMF-28 fibre samples using another new CNTs/DMF mixed solution.

	Diameter (µm)	Etched length (mm)	I.L before OD (dB)	Deposition time (minutes)	I.L after OD (dB)	I.L after polymerization (dB)
1	11.0±0.2	5	1.00	5	9.68	-
2	11.0±0.2	11	1.50	6	14.30	10.90
3	13.0±0.2	20	0.58	20	4.36	4.57
4	13.0±0.2	22	0.94	20	4.70	3.35
5	13.0±0.2	20	0.80	23	3.56	-
6	13.0±0.2	10	1.30	23	14.20	9.00
7	16.0±0.2	10	0.39	23	8.50	5.65
8	16.0±0.2	11	0.37	15	12.00	9.40

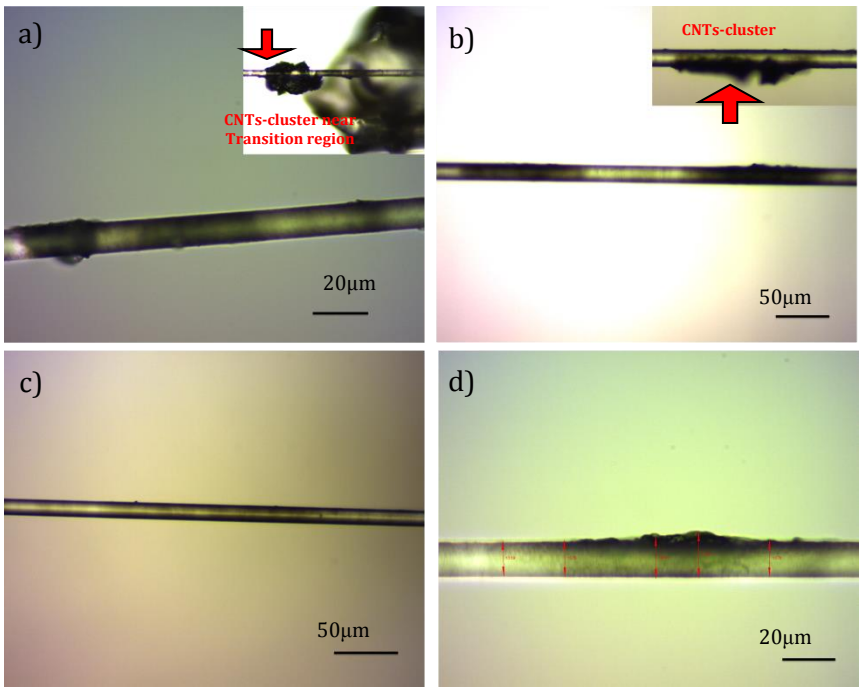

Figure 3.32: Second set of Etched fibre optic samples (by BHF acid (20:1)) optically deposited with CNTs /DMF solution under the microscope. a)11.0±0.5 µm. b)16.0±0.5 µm. c)13.0±0.5µm (without optical deposition process). d) 13.0±0.5µm.

As shown in Figure 4.6 which represents different coated etched SMF-28 fibre samples under the microscope (Nikon- Eclipse LV150L) that resulted from the second attempt of optical deposition. It can be observed that a uniform layer of CNTs deposited around some of the etched surfaces of the optical fibre samples like in Figure 4.6b and c. However,, the amplified injected power that had been launched into the fibre samples was higher and around the range of (23dBm -27dBm) than the power that was used in the first attempt. This resulted in creating a cluster of CNTs and DMF's residue around the etched surface or the transion region of the etched SMF-28 fibre sample (as shown in Figure 6.4 a and b) which is drive to raise the insertion loss of the coated etched fibre sample with CNTs generated by the light scatttering and absorption loss by these clustered CNTs and thermal damages to the etched section of the fibre, and consequently an inefficient photonic fibre device that could be empoly in nonlinear optical applications.

4.3 Four-Wave Mixing Effect in Photonic Fibre Device coated with CNTs

As we are interested in investigating the nonlinear efficiency in the fabricated nonlinear-based microfibre devices embedded with CNTs, we performed the four-wave mixing experiment as one of the methods of optimising these fabricated devices in Section 4.2. Besides, many reports have investigated the FWM in CNTs coated optical fibres to estimate and measure the nonlinear effects of their designed optical devices as mentioned in before Chapter 1[15, 28]. So, in this section, we are going to explore the experimental setup of the four-wave mixing followed by the results and discussion.

4.3.1 Experimental setup

The experimental setup of FWM with several fabricated sampled fibre devices is illustrated in Figure 4.7. We provide two laser sources; a tunable CW laser source (TLS) (1500-1600) nm as a probe signal with an input power -2.15dBm and λ=1550.0nm, and distributed feedback laser (DFB) as a pump signal with an input power 3.6±0.1 dBm at λ=1552.0nm by using a current controller with input current I_{in} ~150 mA. An isolator with an I.L ~ 0.2dB was used to connect to the TLS to reduce any feedback power. Both signal sources, the prop and pump signal are continuous wave (CW). A polarizer controller (PC1 and PC2) has been used for each laser to ensure the phase matching of both the laser sources and to keep them linearly polarised during the experiment. Then, two EDFAs were employed in the experimental setup to amplify the laser source. The EDFA1 was connected with the TLS and amplified the power to a maximum gain of 18.0dBm, while, the EDFA2 was connected to the DFB laser, and the output power of DFB laser (~3.6dBm) was amplified with a gain output power up to 25 dBm. Moreover, a (50:50) coupler with I.L ~3dB was used to couple the two signals (probe and pump) to be launched into the coated fibre device sample. The output transmission spectrum was monitored from the OSA (Advantest-Q8384) in order to measure the idler signal. In addition, we reduced the length of the used pigtailed connecters to less than 0.5m and any bare SMF-28 fibre connected within the setup in order to supress the nonlinear optical effect (SMF-28 η~1.15W^{-1} km^{-1} for fibre L~150m and A_{eff} ~80μm^2 [116]) that would get generated during the experiment on these bare single mode fibres and to make sure it was only created from the coated micro fibre devices. It is worth noting that the first setup was designed as the two laser sources were launched into one EDFA and it has been figured out that the generated idler and FWM effect came from the nonlinear effect produced inside the EDFA and not from the DUT where this setup was reported previously with other groups [13, 15, 28].

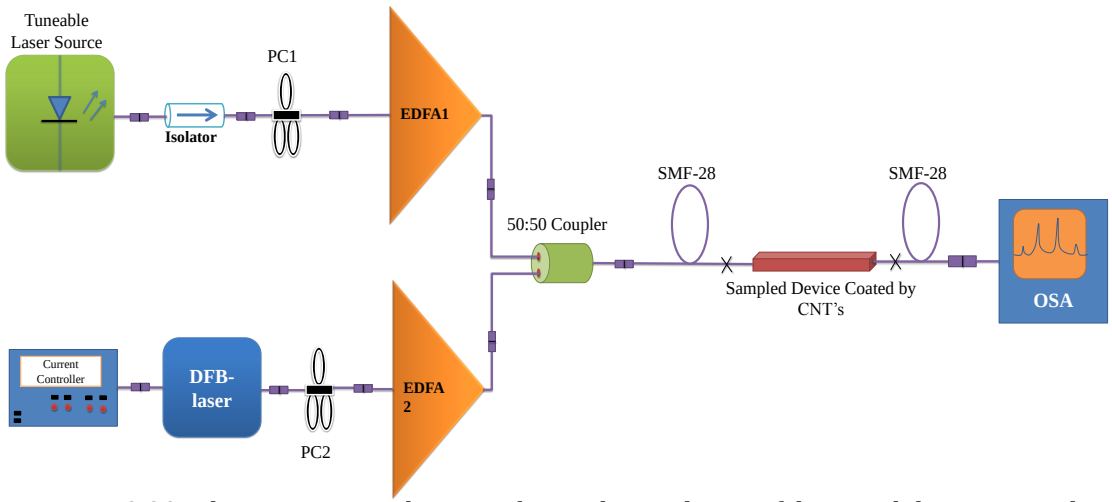

Figure 3.33: The experimental setup of FWM by applying a fabricated device coated with CNTs.

4.3.2 Results & Discussion

First of all, we investigated the FWM setup by applying a bare (non-etched) SMF-28 fibre with fibre length L>150m (D_{fibre}=125µm) instead of the fabricated fibre devices embedded with CNTs as a way to checked and characterize the setup of FWM. The lunched power from both EDFA1 as probe ~18dBm at wavelength of 1548.840nm and the EDFA2 as a pump power ~25dBm at wavelength 1550.02nm. Hence, the FWM output spectrum was monitored after the bare SMF-28 fibre to generate two new wavelengths (idlers); λ_{idler1}= 1547.661nm (SNR~4.3dB) and λ_{idler2} =1551.179nm (SNR~13.9dB), respectively (as shown in Figure 4.8 the red-spectrum). As, the idler signals were matching with the numerical estimation by using Eq.2.37 in Chapter2; $\lambda_{idler1}= 2\lambda_{probe}-\lambda_{pump}$, $\lambda_{idler2}= 2\lambda_{pump}-\lambda_{probe}$. Since the conversion efficiency defined as the ratio of the output idler power with respect to the signal power, then idler 1 and 2 showed a conversion efficiency of ~-35.3dB and ~-26.9dB, respectively, because of the different of the powers of the two pump and probe wavelengths leading to not equal conversion, and the two new wavelengths generated have different powers (SNR). From this optimisation results we assured that our setup is functional to employ with the fabricated coated fibre devices.

On the other side, we examined the CNTs coated etched fibre devices that we fabricated by an optical deposition process first employed coated fibre with IL~3.6dB and etched L=22mm (Table 4.4), as mentioned in the section above. We repeated the same setup as in Figure 4.7, where the input power for the probe and pump signal were used -1.89 ± 0.01dBm and 2.5 ± 0.1 dBm respectively. Then, the two signal sources were amplified to 18.0 ± 0.02 dBm for the probe power (λ_{probe}=1548.840nm, SNR=40.0dB) and 27.0± 0.01dBm for the pump power,

since it needed to escalate the pump power in order to observe a clear idler and due to the fibre device losses, (λ_{pump}= 1550.04nm, SNR~50.5dB)(as shown in Figure 4.8 the black-spectrum), followed by coupling them, by using (50:50) coupler, both to the coated fibre device. Following that, by utilising the OSA to measure the output signal spectrum, we could approach four-wave mixing in the coated fibre samples and generation of one new wavelength idler at 1551.240nm close to the numerical estimation wavelength by $\lambda_{idler2}= 2\lambda_{pump}-\lambda_{probe}$, with SNR = 1.8dB and showed a conversion efficiency about -39.2dB, due to the IL of the CNTs/DMF coated fibre device, we did not observe a second new signal wavelength getting generated idler2. By applying the wavelength conversion efficiency η, Eq. 2.38, at Chapter 2 Section 2.6.2, the nonlinear coefficient γ in the etched fibre coated with CNTs was calculated to be ~1122 W^{-1} km^{-1} for η~-39dB, pump power ~27dBm and for effective length L_{eff} <22mm. Thus, the wavelength conversion efficiency from this coated fibre device did not show an enhancement in the FWM efficiency comparing to the other reported conversion efficiency such as; 1816.8 $W^{-1}km^{-1}$ as the effective γ in CNTs embedded in tapered microfibre (D_{fibre}~1μm, IL~5dB) with wavelength conversion efficiency of -27dB and L_{eff} ~5cm and P_{pump}~32dBm at λ=1550nm −1 by Bo Xu and et.al.[28] and other study had resulted on effective γ of 5640 $W^{-1}km^{-1}$ for wavelength conversion about -21 dB, at P_{pump} ~25dBm λ=1550nm from CNTs deposited on planar lightwave circuit (PLC) waveguide with IL ~19dB by [117].

While the second fabricated fibre samples (D_{fibre}=19.0±0.5μm, IL=1.6dB) embedded with CNTs (shown in Table 4.4) and we repeated the same experimental condition as the coated fibre sample above; as both lunched probe and pump power were ~ 18.0 ± 0.02 dBm (λ_{probe}=1548.840nm, SNR=43.5dB) and 27.0± 0.01dBm (λ_{pump}= 1550.04nm, SNR~53.5dB), respectively. Adding to that, it is worth noting that the pump power was the maximum limit of power that could be applied to the coated fibre device. However, the coated fibre device did not showed a FWM effects and creation of new signal wavelength (idler) at the transmission output spectrum. This is believed is due to the thickness of the etched fibre that was still thick, correspondingly, there is limited rate of evanescent wave that interacting with the embedded CNTs on the fibre. Furthermore, due to the insufficient and unsystematic deposition of CNTs on the etched cladding fibre which has led to very week interaction length of CNTs nonlinearity with evanescent wave extended from the etched fibre.

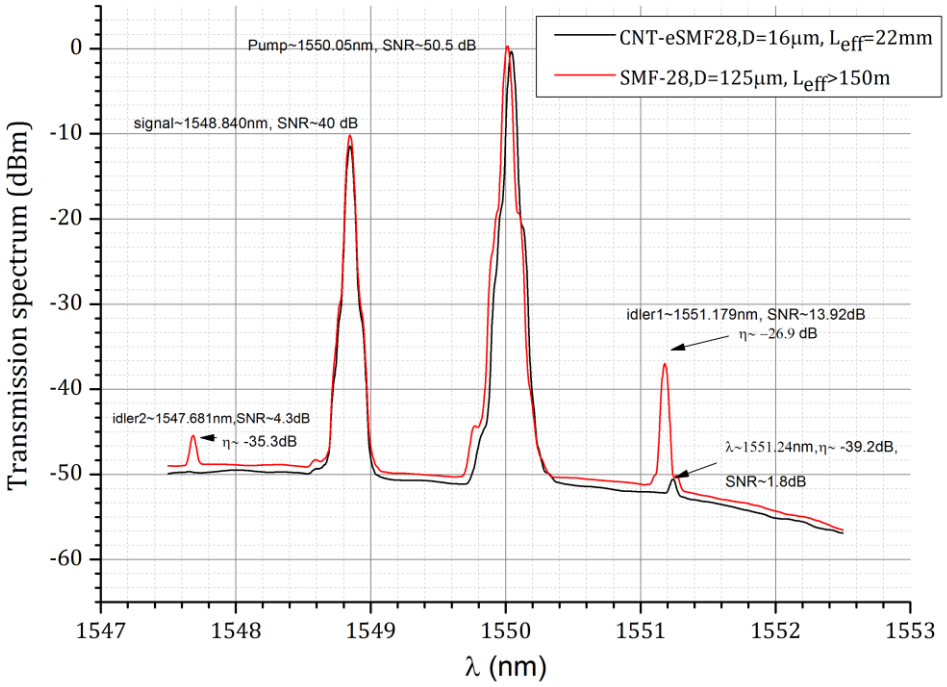

Figure3.34: FWM transmission spectrum for both fibre samples; (red-spectrum) bare SMF-28 fibre (D_{fibre}=125μm) with L>150m and (black spectrum) etched SMF-28 fibre device embedded with CNTs (D_{fibre}=16μm) , L=22mm.

Table 3.4: The measured results of the Optical Fibre FWM coated by CNTs/DMF optically deposited.

Sample	Length (mm)	D_{fiber} (μm)	I.L. (dB)	Probe power		Pump power	
				Output (dBm)	SNR (dB)	Output (dBm)	SNR (dB)
CNT/DMF-SMF-28	22	16.0±0.5	3.6	-11.5	40.0	0.0	50.5
CNT/DMF-SMF28	20	19.0±0.5	1.6	-9.5	43.5	0.9	53.5

From the experimental point of view, the fabricated devices did not show any evidence of nonlinearity for the following possible reasons;

1) A very weak amount of CNTs that optically deposited around and along the etched section of the optical Fibre.
2) Besides the thin and non-uniformity of CNTs deposited layer that surrounding the etched surface of the fibre due to the difficulties in adopting suitable SWCNTs and designing suitable configurations for SWCNT-light interaction..
3) The periodical and cluster formation along the coated section or on both transition regions in the etched fibre during the optical deposition.
4) The high insertion loss of the fabricated fibre devices before they were applied in the FWM experiment.

It is worth noting that the other samples were not efficient enough to be tested as they had very high losses (>11dB or > 92% power loss) and the inconsistency and very week quantity of the deposited CNTs on the etched fibre samples as illustrated in Figures 4.3, 4.4 and 4.6 as well as in Table 4.1 and 4.2.

4.4 Optical Deposition Process using CNTs/Water-SDS mixed Solution

CNTs is known as an interesting material and attracting enormous promising applications; however, it still inhibits deposition, basically due to the effort that is required to separate the entangled nanotubes dispersed with other materials. However, besides the DMF polymer which is mostly used to disperse CNTs, it has been reported in an extensive study that the SDS surfactant can disperse the aggregations of the single-walled carbon nanotubes at room conditions[118]. Here, we are going to investigate the mix of SDS with CNTs coated on the etched fibre samples through the process of optical deposition.

4.4.1 CNTs/SDS Solution

In this section, we are demonstrating another concept of deposition of CNTs, i.e. another surfactant to be used for dispersing of the aggregations of nanoscales of CNTs. Hence, we utilised a mix of DI-Water and 2% of SDS surfactant as solvents for the solute (CNTs). First, 5mg of CNT flakes were ground using a mortar as shown in Figure 4.9a. Then, we added several

drops of acetone solvent to the flakes to ease the grinding process of CNTs. In the next step, we used a commercial SDS powder material. The SDS powder was mixed and dispersed in DI-water with a concentration of 2% via precise measuring scaled in the Chemistry labs. Finally, the CNTs flakes were mixed in 100mL of the mix of 2% of SDS/DI-water solution to have a concentration of 10ppm of CNTs where it was sonicated for about 6 hours until it dispersed homogeneously as shown in Figure 4.9b. Moreover, from our observations, this mix proved to have a longer lifetime of consistent and untangling dispersed CNTs than the mix of CNTs/DMF solution. The mixed solution was ready to be applied on the etched fibre samples as will be discussed in the next Section 4.4.2.

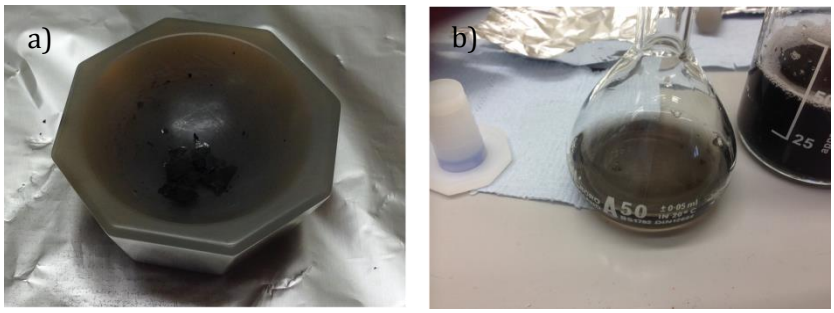

Figure3.35: a) Grounding the CNTs flaks in a mortar. b) Sonicated mix of CNTs in a solution of DI-water and 2% of SDS material.

4.4.2 Experimental setup of the Optical Deposition

Here, several different etched fibre diameters by BHF acid solution with concentration (20:1) have been used to investigate the losses in each different fibre diameter, etched length, optical deposition time and the launch power in the deposition process. We applied the same optical setup and procedure for the optical deposition as mentioned before in Section 4.2. Two (99:1) couplers were used in the setup as shown in Figure 4.10. One of the couplers, its input port (common) was connected to the EDFA amplified input power. The other two output ports 99% and 1% were connected to the etched fibre sample and power-meter 1. This used to control the value and the stability of the injected power into the fibre sample during the optical deposition run. The second coupler was connected to the end of the fibre sample to measure and monitor the output power during the deposition run, in-situ and after the end of the process (illustrated in Figure 4.10). The optical deposition process was done at wavelength 1560nm. The maximum launched power from the EDFA source was up to 20dBm @1560nm.

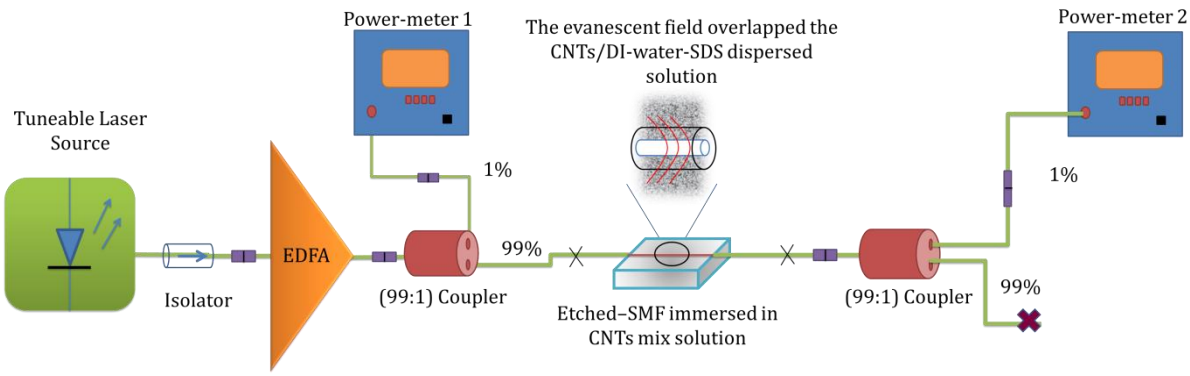

Figure3.36: the experimental setup of the optical deposition of CNTs on the etched SMF28 surface by submerging it in a solution mix of CNTs/DI-water-SDS.

4.4.3 Results and Discussion

The process of the optical deposition was done for a number of etched fibre samples with different diameters and times of deposition. The prepared mix solution of CNTs/DI-water-SDS was encompassed on a concentration of CNTs of 10ppm. We monitored the deposition of CNTs around the etched surface of fibre sample based on the output power via the power-meter2. We stopped the process of deposition when we reached an observed insertion loss within 1-3dB. Table 4.5 includes the resulted coated etched fibre samples with CNTs from the process of optical deposition by applying dispersed CNTs in a solution of DI-water and 2% of SDS. Figure 4.11 shows the microscope images of the coated etched fibre samples after optical deposition. It can be discerned from Figure 4.11c, that the fibre sample with D_{fibre}= 13.0±0.5μm was coated with CNTs and a cluster was formed around the etched surface of the fibre led to optical IL ~3.3dB (Table 4.5). This cluster is dried residue of the CNTs and the SDS (as shown in Figure 4.11 c) which is attributed to the high optical loss of the coated fibre samples that is correlated to the light scattering and optical absorption by the cluster and layers of CNTs deposited on the fibre (as explained before in Section 4.2.1, and could have been caused, due perhaps to the following reasons:

1) Two times of optical deposition run as we tried to obtain a uniformly coated layer of CNTs.
2) We launched a high input power into the etched fibre sample in the two runs.
3) Several drops of the mixed solution on the etched fibre sample during the optical deposition run, in-situ, assuming that the CNTs will be deposited efficiently and consistently on the etched cladding surface of the fibre sample.

Alternatively, the other two samples (Figure 4.11a and 4.11b) showed an enhanced coating layer around the etched surface of the fibre with less clustering around the etched fibre sample, yet we still observed the same trend of periodic deposition of CNTs along the etched fibre as illustrated in Figure 4.11a, and as mentioned before in Section 4.2.1. From Table 4.5 it can be observed that the coated fibre samples have shown lesser insertion loss than the applied solution of CNTs/DMF in Section 4.2, except that the one in Sample no. 2 and 3 (D_{fibre}=12.0µm±0.5µm and 10.0µm±0.5µm) had a high insertion loss than the other fibre samples since the two fibre samples had long time of optical deposition process (180mins and 30mins as detailed in Table 4.5). Furthermore, we believe it is also related to the two times of optical deposition process on each side of the fibre as we tried to obtain a uniformly coated layer of CNTs. However, this has resulted of formation of clusters of CNTs with residuals of SDS on one or both sides of the transition region or the middle etched section of the etched fibre (as shown in Figure 4.11c). Adding to that, seemingly there was no urge to apply low index polymer to suppress the insertion loss of these coated fibre devices by CNTs/DI-water-SDS. What is more, due to limit time of this work and the unavailability of most optical equipment we was not able to apply these deposited fibre samples in FWM effect experiment likewise the resulted deposited fibre samples in Section 4.3. However, instead of that some of these coated etched fibre devices were used to demonstrate saturable absorption effect to characterise the nonlinear optical functioning of these fabricated fibre devices as will be examined later in the next section.

Table 3.5: The resulted data of the coated etched fibre samples by an optical deposition process, by using CNTs/DI-water-SDS solution.

	Diameter (µm) ±0.5(µm)	Etched length (mm)	I.L before OD (dB)	Deposition time (minutes)	I.L after OD (dB)
1	13.0	10	0.9	15	3.3
2	12.0	10	1.9	180	15.0
3	10.0	10	2.0	30	9.6
4	10.0	10	1.8	12	3.3
5	12.0	10	0.70	24	1.4
6	16.0	20	0.34	15	3.5

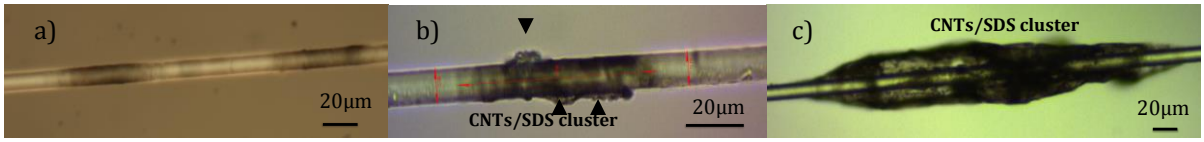

Figure 3.37: Etched fibre optic samples by BHF aicd (20:1), optically deposited with CNTs /DI-Water-SDS solution checked under microscope Nikon. a)D_{fibre}=10.0±0.5µm. b)D=12.0±0.5µm. c)D=13.0±0.5µm.

4.5 CNTs Etched Fibre Devices as Saturable Absorber

Saturable Absorber (SA) is a nonlinear optical component with a certain optical loss that drops when applied to high optical intensities. Therefore, SAs have been implemented widely to obtain mode-locking fibre lasers. Since CNTs, and specifically single-wall carbon nanotubes SWCNTs, have an excellent performance it can be applied as an SA [119]. This is because SWCNTs are direct-bandgap materials and their band-gap depends on the diameter and chirality of the CNTs structure as aforementioned in Chapter 2, Section 2.6.1.

Hence, in this section, we will be demonstrating and optimising the fabricated etched photonic fibre devices coated with CNTs as an SA for the purpose of testing and emphasising the nonlinear effect on these coated fibre devices that were fabricated in Section 4.4.

4.5.1 Experimental Setup of CNTS Coated Fibre Devices as SAs

Figure 4.12 represents the optical experimental setup of CNTs coated etched fibre devices as an SA. These devices will be named as device under test (DUT), since we are characterising and testing their nonlinear optical effect as SAs. The setup included a tunable CW laser source (TLS) (Anritsu Tunics BT) with bandwidth 1500nm-1600nm, an isolator with input power 1dBm, EDFA power amplifier with output up to 30dBm. An optical attenuator (HP Agilent Keysight 8156a) was used to reduce the amplified power launched into the DUT in steady steps.

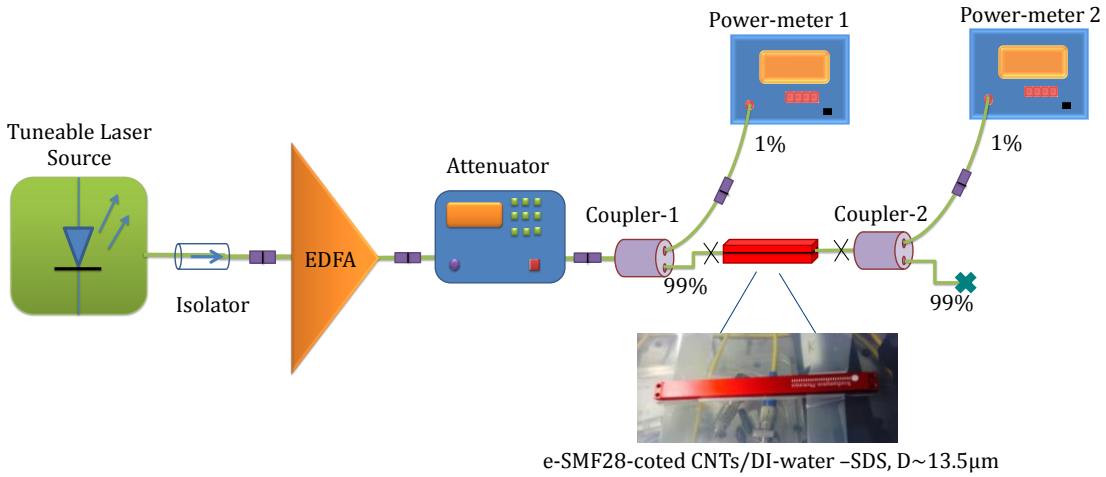

Figure3.38: Experimental setup of the proposed CNTs coated etched fibre devices as a SA. In the set shows the coated fibre device under test (DUT).

In Addition, two (99:1) couplers were used in the setup; coupler-1 to measure and monitor the stability of the injected power into the DUT, and coupler-2 to measure the output power from the DUT. This DUT was made from the fabricated etched fibre samples that were coated by CNTs in Section 4.4, and after they were checked under the microscope they were mounted in an AL- container. The two fibre ends of DUT were spliced to pigtail connectors with splice losses < 0.02dB and connected to the optical setup as shown in Figure 4.12. Following that, a CW- light source was launched by using TLS source, and then it was amplified through the EDF-amplifier. The amplified output power was attenuated in steps consistently through the attenuator before it was injected into the DUT from the 99% tap of the coupler. The output power was measured from the 1% tap of the second coupler of (99:1); and the results will be discussed and illustrated in the next section.

4.5.2 The Results and Discussion

The DUT that was coated with a CNTs/DI-water-SDS mixed solution had a D_{fibre}= 13.5µm±0.5, IL~-27dB, and etched section length=10 mm. In this experiment, we applied two different laser sources CW and pulse source with the same setup as in Figure 4.12. Figure 4.13 illustrates the experimental results of optimising the fabricated coated etched fibre device or DUT (with D_{fibre}=13.0±0.5µm) as an SA for two different light sources CW-source and pulse source at λ=1550nm. In case of the CW-laser source, with an injected power of around 12dBm (~16mW) into the DUT, the loss of the DUT reduced and exposed an SA effect with an increase in the launched power, and the reduction was by more than 23dB as shown in Figure 4.13a. In case of a pulsed laser source, a seed laser operating at 1550 nm is pulse modulated

using an acousto-optic modulator with pulse repetition frequency (PRF) of 200 kHz and 10% duty cycle. The pulses are amplified in a 27 dBm average power EDFA. The output from the EDFA is passed through a variable optical attenuator (VOA) and launched into the DUT as shown in Figure 4.12. 1% taps are used to monitor the power into and out of the DUT to measure the transmission characteristics. The EDFA gives 5 W of peak power with highest output average power of 27 dBm with 10% duty cycle. However, the fibre device did not show a noticeable effect as an SA due to the high pulse peak of the input power which it is believed to have caused a thermal damage to the CNTs coating layer of the DUT and degradation of the optical properties of the embedded nantubes as reported in sevral studies[115, 120] (Figure4.13b).

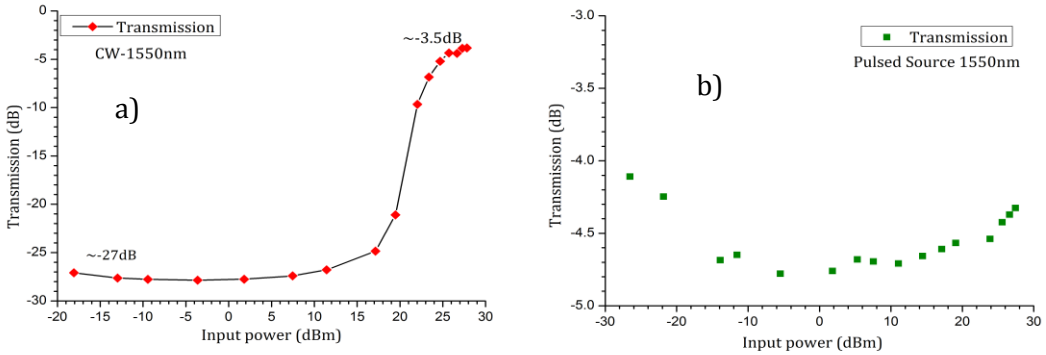

Figure 3.39: Experimental results of the proposed CNTs/SDS coated etched fibre device as a SA effect has a D_{fibre}=13.0±0.5μm, etched length= 10mm. a) CW-source. b) Pulse-source.

Other samples with different diameters were proposed as SAs by applying the same setup and procedures as mentioned above. Two other DUTs were proposed with D_{fibre}= 10.0±0.5µm (IL= 17.1dB), and D_{fibre}=12.0±0.5µm (IL=24dB) with etched length= 10mm for both, applied at λ=1550nm as SAs as shown in Figure 4.14 a and b. Those two coated samples did not illustrate a strong effect as an SA either which is attributed to week layer of deposited CNTs around the microfibre, whereas the IL of DUT with D_{fibre}= 10.0±0.5µm has shown only ~ 0.7dB reduction at high power, >25dBm (Figure 4.14a) while for the sample with D_{fibre}=12.0±0.5µm showed ~3.5 dB reduction in IL (Figure4.14b). We checked these samples twice by reducing the attenuator (forward) and increasing the attenuator (backwards) to emphasize any different trends of saturable absorbing for the tested samples. In these two samples, we did not obtain a high notable SAs effect due to what might be the non-functional and insufficient coating quality of deposited CNTs around the etched fibre samples. In addition, a poor amount of coated layer of CNTs embedded on the etched surface of the fibre samples.

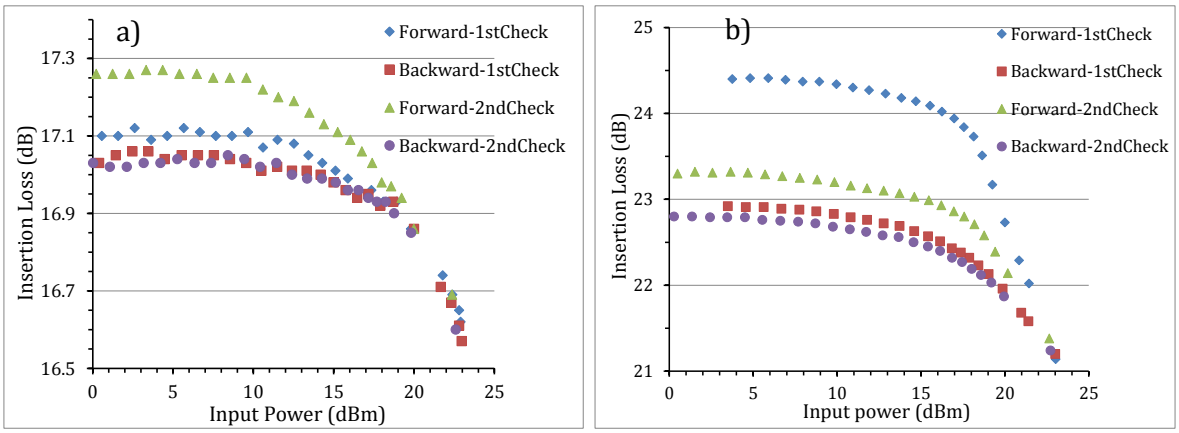

Figure 3.40: Experimental results of the proposed CNTs/SDS coated etched fibre device as a SA for different diameters at λ=1550nm. a)D_{fibre}=10.0±0.5µm. b) D_{fibre}=12.0±0.5µm.

4.6 Conclusion

In this chapter, we investigated and demonstrated a simple method for fabricating photonic microfibre devices coated with CNTs and that is by optical deposition process. We examined and illustrated the performance of two mixed solutions including on homogenous dispersed CNTs which are commercial CNTs/DMF solution and CNTs/DI-water with 2% of SDS was prepared in the laboratory. The coated etched fibre samples that resulted after the process of optical deposition of CNTs dispersed in DMF solution, were very lossy where in some coated fibre samples the IL exceeded 60 dB due to the interaction between the evanescent wave and the CNTs dispersed in the DMF polymer mix solution led to absorption loss and light scattering. Another factor investigated during the optical deposition was the optical deposition time impact on the optical loss which is showed inconsistencey effect on the optical loss (or IL) of the fibre samples embedded with CNTs in our setup work. Another point that it is believed is attributed to the insufficient dispersion of CNTs around the etched fibre samples was the shelf-life limitations (<3months) of the commercial mix solution of dispersed CNTs in DMF and it was displaced by employing a new same mix solution of CNTs/DMF. At the second attempt of optical deposition, the resulted etched fibres embedded with CNTS showed drop and enhancement in the optical losses than the first attempt of optical deposition process, due to applying thinner etched fibre samples (D_{fibre} <13.0μm), and using functional new mixed solution of CNTs/DMF. Nevertheless, the optical loss of some coated fibres still high (>14dB) due to the light scattering and absorption loss by CNTs, which also believed was associated with the injected power to the fibre samples escalated to ~23dBm-27dBm, and formation of CNTs agglomeration on one side middle section of the etched fibre. Adding to that, we abled relatively, to reduce the optical losses in most of the fibre samples caused by the coated layer of CNTs by applying low index polymer (n=1.37) due to the effect of light scattering and coupling out of more evanescent wave were minimized since the propagating mode becomes more guided by the low index polymer (>air=1). Furthermore, the resulted fibre samples embedded with CNTs after check under microscope were non-uniform CNTs depositions around the etched surface of the standard fibre; where the CNTs are most likely to entangle in some areas, besides formation of periodic way along the etched section of the fibre.

A solution of CNTs dispersed homogenously in a mixed of DI-water and 2% of SDS was prepared and employed efficiently on the etched fibre samples. It has been observed that the CNTs that dispersed in DI-water-SDS solution have longer disentanglement and consistency lifetime than the CNTs/DMF solution. The CNTs coated etched fibre devices that resulted from the optical deposition process showed an enhanced coating layer around the etched surface of the fibre with less clustering around the etched fibre sample and optical loss

comparing to the optical deposition employed CNTs/DMF mix, yet we still observed the same trend of periodic deposition of CNTs along the etched fibre and unpredictable trend of high optical losses for several etched fibre samples due to the light scattering and absorption loss by the deposited CNTs around the fibre. Moreover, a periodic cluster creation along and around the etched surface of the fibre during the optical deposition was seen which caused on fabricating optically deficient and lossy coated photonic fibre devices for both used mix solution CNTs/DMF and CNTS/DI-water-SDS.

However, we were able to apply couple fibre devices (D_{fibre}=16.0μm and 19.0μm) coated with CNTs in FWM effect without being able to achieve an efficient enhancement performance of nonlinearity due to the high losses and the poor coating layer of CNTs on the surface of the etched fibre. One coated fibre samples (D_{fibre}= 16.0μm) showed a very weak four-wave mixing at λ=1550nm and generation of new wavelength (λ_{idler}=1551.240nm and SNR~1.8dB) with conversion efficiency ~-39dB and calculated effective nonlinear coefficient ~ 1122 W^{-1} km^{-1} for pump power ~27dBm and for effective length L_{eff} <22mm which is lower than other reported results[28, 117]. While, four-wave mixing effect was not obtained from the second coated fibre sample (D_{fibre}= 19.0 μm) because of thickness of the etched fibre, hence less rate of evanescent wave that interacting with the nonlinearity of the embedded CNTs besides the optical loss of the fabricated coated fibre (~2dB) and lack of CNTs dispersed along the etched fibre. We were not able to observe incompetent four-wave mixing effect due to the difficulties in adopting suitable SWCNTs and designing suitable configurations for SWCNT-light interaction with evanescent wave of etched fibre samples.

Furthermore, some of the fabricated coated fibre devices by CNTS/DI-water-SDS with D_{fibre}~ 13.5μm (IL~-27dB) with high optical losses were implemented as SA and presented a considerable reduction of loss was by more than 23dB by injecting CW source high power <27dBm, whilst by injecting pulse power output average ~ 27dBm (peak power ~5 W) resulted on unnoticeable drop in loss and SA effect due to a thermal damage by the high input power and degradation of the optical properties of the embedded nanotubes as other reported [115, 120]. Furthermore, another two CNTs/SDS coated fibre both with D_{fibre}~ 10.0μm (IL= 17.1dB), and 12.0μm (IL=24dB) with etched length= 10mm for both, investigated at λ=1550nm as SAs showed a weak drop in the optical loss ~0.7 dB and 3.5dB, respectively, at high injected power >25dBm associated to the poor amount of coated layer of CNTs embedded on the etched surface of the fibre samples.

Chapter 5 : Modelling and Simulation of Cladding-Thinned of Optical Fibre

5.1 Introduction

In this chapter, we investigate and optimise the impact of thinned cladding diameter in a standard single mode optical fibre, by building a simulation model of etched silica cladding in a single mode optical fibre using COMSOL Multiphysics software. The resulting numerical simulations will be compared to the experimental data obtained in Chapters 3 and 4. In the first Section, we will concentrate on modelling of etched optical fibre (single-mode fibre) and study the behaviour of the propagating mode and the evanescent wave and their association with the change of diameter and the effective mode index in etched silica-cladding fibre optic. Moreover, a numerical optimisation of the rate of the evanescent wave overlapping within the outer-cladding in etched optical fibre and for different fibre diameters and surrounding refractive indices (SRIs) will be presented in the Second section. In addition, a numerical study of thinned FBG as a function of various diameter and SRIs and their effects on the optical features of the etched fibre in the perspective of; effective refractive index, generation of higher-order modes and Bragg wavelength shifts will be demonstrated in Section 3. Section 4 provides a theoretical expectation of the effective nonlinear coefficient of a coated optical fibre by CNTs in terms of different fibre diameters and various concentrations of coated CNTs. Finally, in section five, we will investigate by a numerical speculation of the effective nonlinear coefficient of the proposed fabricated CNTs based etched optical fibre devices by implementing them in FWM application.

5.2 Modelling of Etched Optical Fibre

In this section, we have built a simulation model of single mode fibre with the same parameters and optical specifications of the SMF-28, which has been employed experimentally in the wet chemical etching process, as explained in Chapter 3. By using the COMSOL Multiphysics software, we aim to study the wave equation of the propagated mode by solving Maxwell's equation to analyse and calculate the mode effective indices of the model fibre, by applying the finite element method at different fibre diameters for the SMF-28 profile. From another perspective, we analyse the effect of other parameters such as the change of normalised electric field propagating within and outside the etched fibre, and the effective refractive index n_{eff}.

Firstly, the model of the step-index optical fibre for single mode guidance, SMF-28 uses the following parameters; core diameter (D_{core}) = 8.2µm, refractive index of the core (n_{core}) = 1.4489, inner cladding diameter ($D_{in\text{-}Cladding}$) = 125 µm, and its refractive index ($n_{in\text{-}Cladding}$) = 1.444, outer cladding diameter ($D_{out\text{-}Cladding}$) = 200µm, and its refractive index ($n_{out\text{-}Cladding}$) = 1.360 (is estimated BHF acid refractive index with concentration (20:1)). Figure 5.1 illustrates the model index profile of single mode fibre as a function of fibre radius (rc) and has been done for three different fibre diameters D_{fibre}= 125µm, 67.5µm and 10µm (rc= 62.5 µm, 33.75 µm and 5.0 µm). The study is done at λ=1550nm by solving a variation of the refractive index region of step-index fibre for, each, the core index, inner cladding index, and outer cladding index (the surrounding medium index).

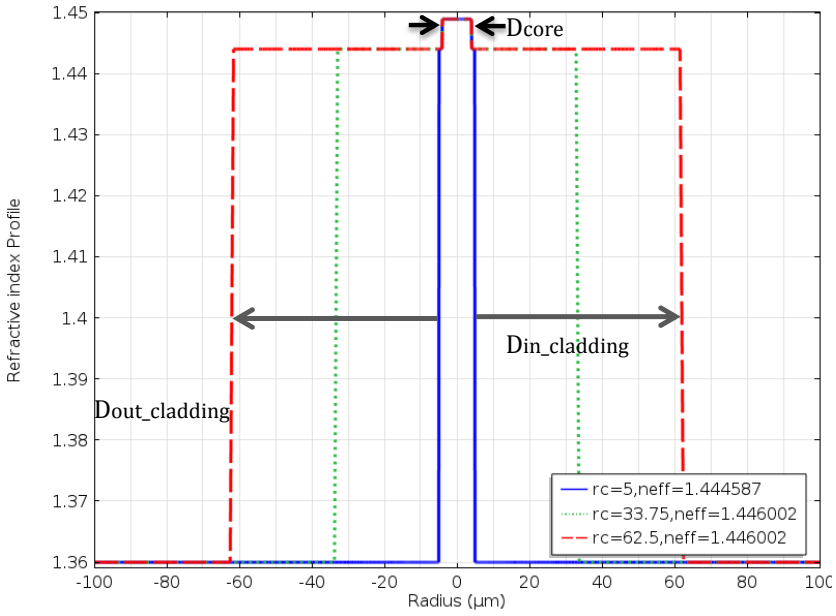

Figure 3.41: The index profile of standard mode fibre model of SMF-28 at λ=1550nm for three different fibre diameters D_{fibre} = 125µm (rc=62.5 µm), 67.5µm (rc=33.75 µm) and 10µm (rc=5.0 µm).

In Figure 5.2a, b and c, the mode analysis of the electric field distribution is demonstrated for inner- and outer-cladding, and within the core of the SMF-28 fibre for various fibre diameters. It can be seen how the propagated mode started to be more confined in the core with the thinner cladding diameter, especially in the case of the non-cladding layer, D_{core} = 8.2µm, where the majority of the mode is propagating (as shown Figure 5.22c). As it was explained before, that propagating mode is more likely to confine in the fibre core, as it is not well bonded anymore by the thick layer of cladding, allowing the evanescent field to extend from the inner cladding to interact with the outer cladding.

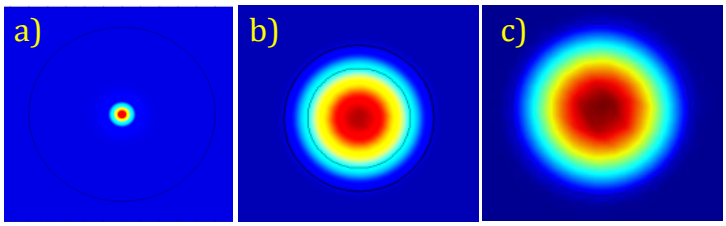

Figure 3.42: The mode distribution of the electric field intensity propagating within core, inner-cladding, and outer-cladding of the single mode fibre for different diameters of fibre ; a) 125µm. b) 12µm. c) 8.2µm.

To clarify the change of the propagated mode in thinned SMF-28, Figure 3.5 shows the normalised electric field propagating within the core and different diameters of inner-cladding of the fibre model. What can be noticed is the change of normalised electric field distribution in standard optical fibre with a normal diameter at rc =62.5µm (D_{fibre}=125µm) (dashed-diamond-red) and rc =33.5 µm (D_{fibre} =67.5 µm) (dot-circular-green), in addition to seeing how it became highly confined near the core diameter of the fibre, rc=5.0µm (D_{fibre} =10µm) (line-star-blue). As is known, the NA of standard SMF-28 is ~0.12 and V=1.99 (as calculated) at λ=1550nm is $<V_{cut\text{-}off}$ (2.405). However, in the case of thinned SMF-28 model (D_{fibre} =10µm), the distribution of normalised electric field decreased by 20 percent in the core as a response to the increase of the NA and the V-number as well as the normalised propagation constant (as in Eq. 2.3) of the fibre. Subsequently, in this stage, the fibre starts to support higher-order modes through the thinned waist section of the etched fibre and attenuation for the propagated intensity occurs. From another perspective, the evanescent wave rate starts to propagate from the inner-cladding, extending with a specific fraction, depending on the fibre diameter, to the outer-cladding; this will be illustrated numerically in Section 5.2.

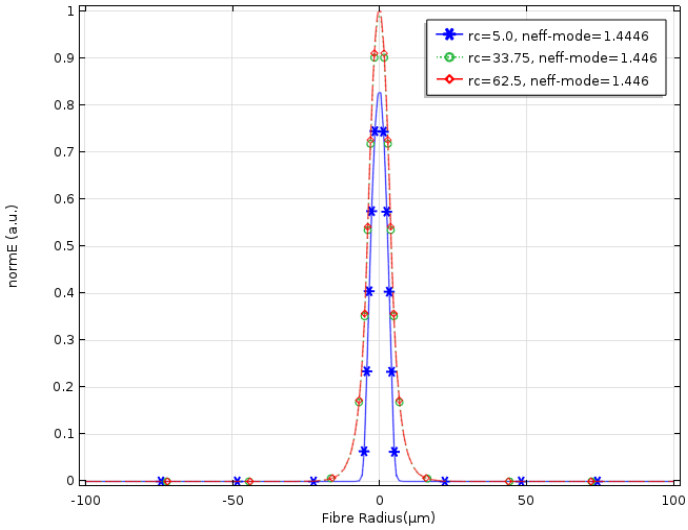

Figure 3.43: The normalized electric field profile propagating in etched SMF-28 fibre as a function of fibre radius.

Another point has been investigated to clarify the variation effect of fibre diameters on the n_{eff} of the standard optical fibre model as a function of SRI coating or outer-cladding refractive index, as illustrated in Figure 5.4. When the outer-cladding refractive index became closer to the inner-cladding index ~ 1.444 (orange-dot-lines in Figure 5.4), the n_{eff} of the SMF-28 model was reset to the initial value of 1.446 since NA of the fibre return back to ~0.12 as well as the V-number of the fibre as SMF-28 value ($V_{cut\text{-}off}$<2.405) and the propagating mode guided as normal single mode fibre and for different fibre diameters. While, at higher external SRI at n>1.445 (navy-cross-line in Figure 5.4), as it started coming closer to the core index, it resulted in weakly guiding of the propagating fundamental mode with less confined and coupling out of the core region. This is leading to rise the interaction with the outer-cladding (or the higher SRI), especially since the fibre diameter is thinned to D_{fibre}<20.5µm[121], these are due to the changes in the optical parameters of the thinned fibre from the n_{eff}, consequentially the NA of the fibre model. Moreover, we could predict from this numerical simulation that n_{eff} of the propagating mode is more sensitive to the SRI in etched SMF-28 with fibre diameters <20µm and as it has been reported in other studies [21, 41, 121] and illustrated in Figure 5.4. This investigating was for the objective to control the optical mode to be more guided by the core leading to less insertion loss with a controlled rate of an evanescent wave propagating within the inner-outer cladding interface, and that is achieved by selecting the right index coating in the process of fabricating the CNTs based photonic fibre devices.

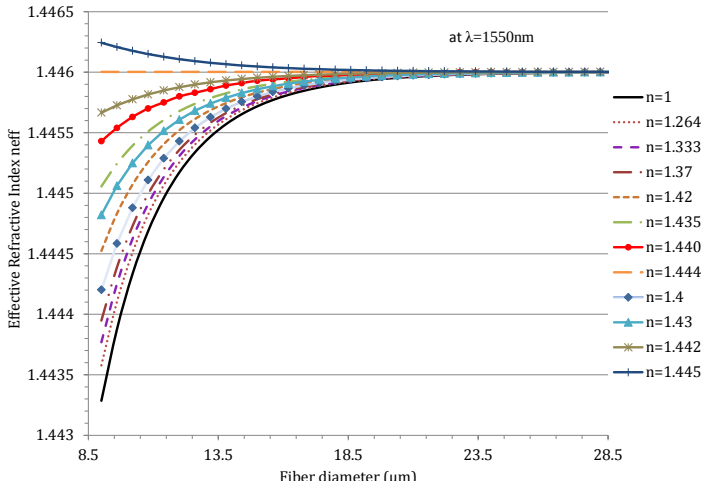

Figure 3.44: The variation of effective refractive index as a function of optical fibre diameter for different outer-cladding (SRI) coatings.

Furthermore, it is worth mentioning that n_{eff} is particularly sensitive to the SRI for cladding diameter below ~ 20μm, when it started to gradually drop within a sensitivity of about 10^{-5} for different coatings of SRI between 1 and 1.445, beyond a cladding diameter of 20μm—as clarified in Figure 5.4. Hence, most of the numerical simulations were done by the SMF-28 fibre model in COMSOL done from diameter 20μm in the next section, as the most effective and sensitive region to the SRI in etched –cladding fibre.

5.3 Optimisation the Fraction of Model Power at the Outer-Cladding of Thinned Optical Fibre

We could optimise by applying the same COMSOL model, a numerical simulation of the fraction of model power (FMP), the evanescent wave that extends into the outer-cladding in a single mode fibre as a function of fibre diameter and various refractive indices of the outer-cladding (external layer surrounding the etched fibre cladding) were demonstrated as shown in Figure 5.5 and Figure 5.6. As a function of fibre diameter with various refractive indices of the outer-cladding, the overlapped power fraction (or FMP) was valued. In Figure 5.5 b, d and f, we clarified that the higher-order mode has a higher value of evanescent wave overlapping with the SRI (outer-cladding), than the fundamental mode (LP01) (Figure 5.5 a, c, and e), in given an etched single mode fibre surrounded with BHF acid for different diameters.

Therefore, this study aimed at fabricating coated fibre devices with minimum insertion losses. We need to control the intended rate of overlapping of evanescent field with the coated materials for a specific diameter and apply the right index mix, with the purpose of fabricating coated fibre devices with low losses and an effective nonlinear coefficient (γ_{eff}). In addition, from another viewpoint of this simulation, we can evaluate the interaction of the extended evanescent waves with the coated substances (measurand) with different refractive indices in correspondence to Bragg wavelength shift in etched FBG for sensing application. As a single mode fibre SMF-28 is used in this work, which is indicated as a weakly guiding mode due to $n_{core}/n_{cladding} \cong 1$, the optical fraction carried by each propagated mode is specified by the propagated mode power through that specified layer (of the optical fibre structure) to the total power of the propagated mode through all area sections of the optical fibre[122].

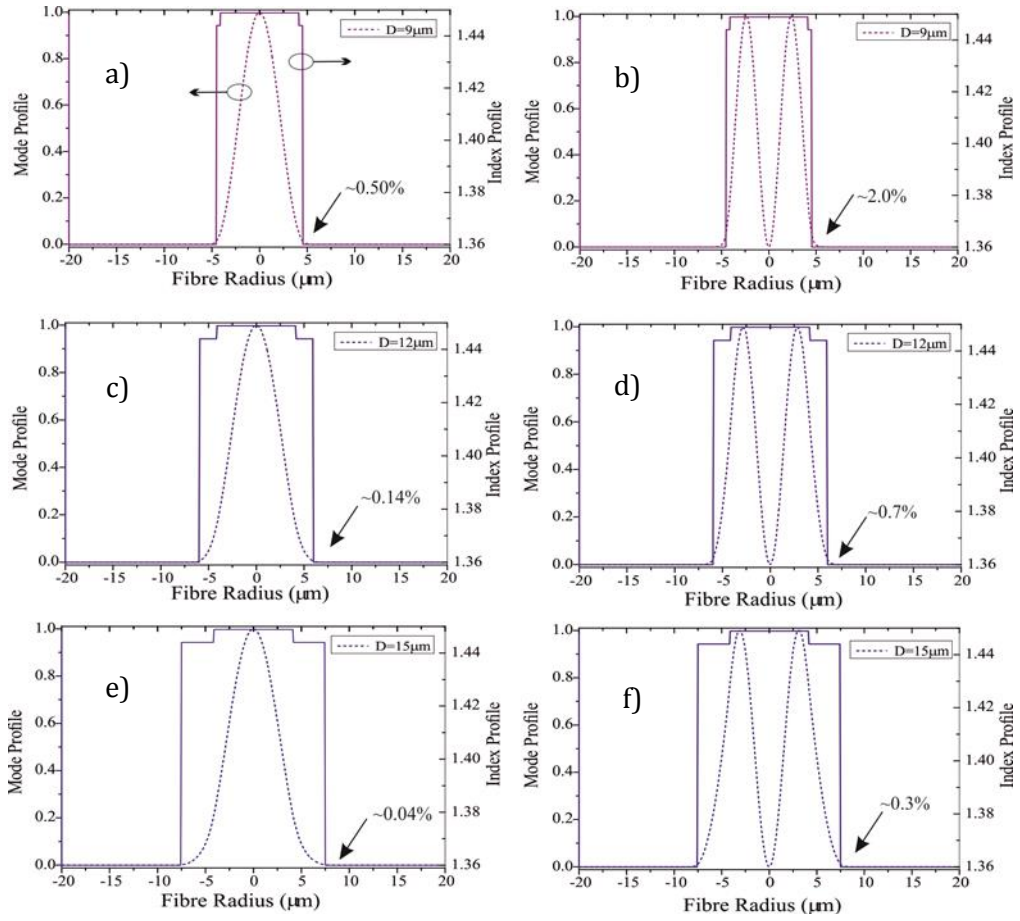

Figure 3.45: The propagating mode profile of etched standard optical fibre, SMF-28, and their index profile for different diameters; D_{fibre} =9.0μm, 12.0μm, and 15.0μm in BHF acid (20:1) (n=1.360 to be demonstrated later) for the fundamental mode LP01 a), c), e), and the first-Higher-order mode LP11 b), d), f) at λ=1550nm.

The COMSOL model is based on solving the wave equation to analyse the mode propagation through a thinned cladding fibre and estimate the rate of evanescent mode extending to the Outer-cladding at thinned optical fibre, $\Gamma_{outer\text{-}cladding}$ by applying;

$$\Gamma_{outer-cladding} = 1 - \left(\Gamma_{core} + \Gamma_{inner-cladding}\right) \quad (5.1)$$

where, Γ_{core} and $\Gamma_{inner\text{-}cladding}$ are the fraction of model power of the propagating mode for the core and the inner-silica-cladding at the optical fibre, respectively. From the numerical results, the evanescent mode fraction $\Gamma_{outer\text{-}cladding}$ at the outer-cladding for the fundamental mode LP01, along with those for the higher-order modes of LP11, LP02, LP21, was estimated theoretically based in Eq. (5.1), as illustrated in Figure 5.6a,b, c and d. The numerical simulations were obtained with a wavelength of 1550.0nm. From Figure 5.6, the fraction of the propagating mode FMP within the outer-cladding shows the tendency to rise with thinner silica cladding. For instance, n=1.360 at fibre diameter = 15.0 μm has an interfacing depth of ~0.04 %, while at fibre diameter D_{fibre} =9.0 μm, the fraction depth, FMP is 0.50% and therefore is more sensitive to the outer-cladding index (external refractive index). Moreover, for the applied refractive index in the outer-cladding, the fraction of overlap will change for the same fibre diameter to other. For example, at same fibre diameter D_{fibre} =9. 0μm and for LP01, at low applied index =1.320 and high index= 1.440 at λ= 1550.0nm, the fraction of interfacing is 0.30 % and 10.2 %, respectively, as shown in Figure 5.6a.

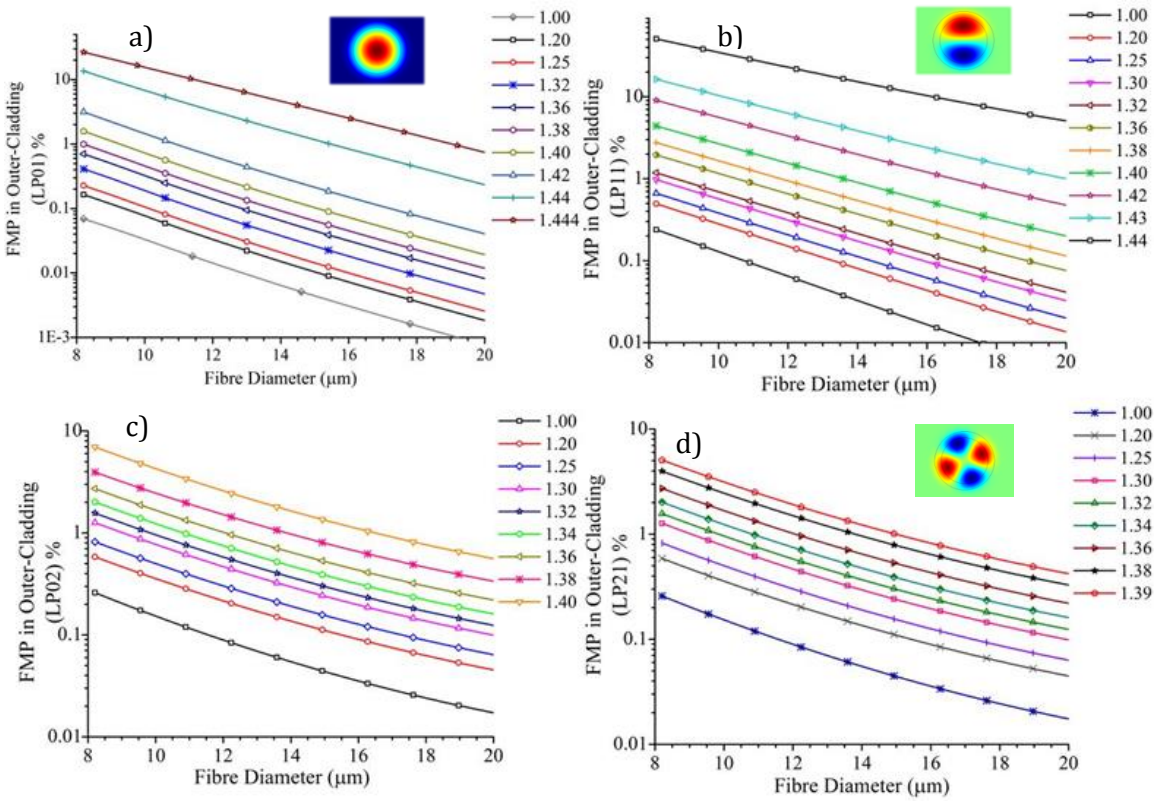

Figure 3.46: The fraction of model power (FMP) at the outer-cladding (surrounding layer) as a function of different fibre diameter and various refractive indices of the surrounding for; a) LP01. b) LP11. c) LP02. d) LP21. At λ=1550.0nm.

Higher-order modes shows larger fraction of evanescent wave, FMP, than LP01, such as in LP11 for the fibre diameter D_{fibre}= 9.5µm, and for an applied index= 1.32 and 1.44, the rate of the fraction FMP is 0.90% and 40.0%, respectively. Thus, the evanescent wave in the inner-cladding is almost likely to extend its tale to the outer cladding (the surrounding index) and increase the interfacing rate with the outer layer. Thus, in this way we are able to better control the rate of overlapping with the interacted coated materials, to get a coated fibre with minimum insertion loss. The same trend can be seen in the higher-order modes from LP11, LP02, LP21, as shown in Figure 5.6b, c and d. They revealed higher FMP of evanescent wave than the fundamental mode from 1% depth of overlapping with fibre diameters < 11µm and exceeding 10% within high refractive indices of the surrounding. Furthermore, These are corresponding to the changes of effective refractive index $n_{eff,}$ NA and the V-number of the fibre by reducing the inner-cladding diameter and the variation between $n_{in\text{-}cladding}$ and $n_{out\text{-}cladding}$ leading to a more leaky fundamental mode [123].

5.4 Optimisation of Thinned Fibre Bragg Gratings

In order to check and support the results that we obtained from the experiment of etching uniform FBG, we applied a numerical analysis by COMSOL software proposing the same step-index model mentioned above. In addition, we aim to clarify the obtained results from the thinly coated FBG by comparing them to the numerical study, using the same parameters in the simulation study as the ones used in the experimental FBG-sample.

From Figure 5.7, we notice the variation effect on the n_{eff} as a function of SRI within different diameters of uniform FBGs. The simulation reported on the increase of effective refractive index n_{eff} sensitivity with higher SRI corresponding to a thinner fibre diameter. For instance, at D_{fibre}=8.4µm and D_{fibre} =24.0µm, the n_{eff} sensitivity (Δn_{eff} / Δn_{SRI}) at n=1-1.2 is ~ 1.2×10^{-3} and ≈ 4×10^{-6}, respectively. While at n=1.435-1.442, the n_{eff} sensitivity is ≈ 0.1 and ~6×10^{-4} for D_{fibre}=8.4µm and D_{fibre}= 24.0µm respectively. Thus, reducing the inner-cladding thickness of the FBG decreased the n_{eff} to smaller than inner-cladding refractive index and subsequently the NA and V-number of the fibre increased, resulting in the propagating fundamental mode being more guided by the core as well as the single mode fibre starts of supporting higher-order modes. This increases the rate of the evanescent field overlap into the outer-cladding, attributed by the extended tail of higher-order modes and small rate of the fundamental mode resulting in the etched FBG and growing more sensitive to SRI, specifically at D_{fibre}< 15.0µm.

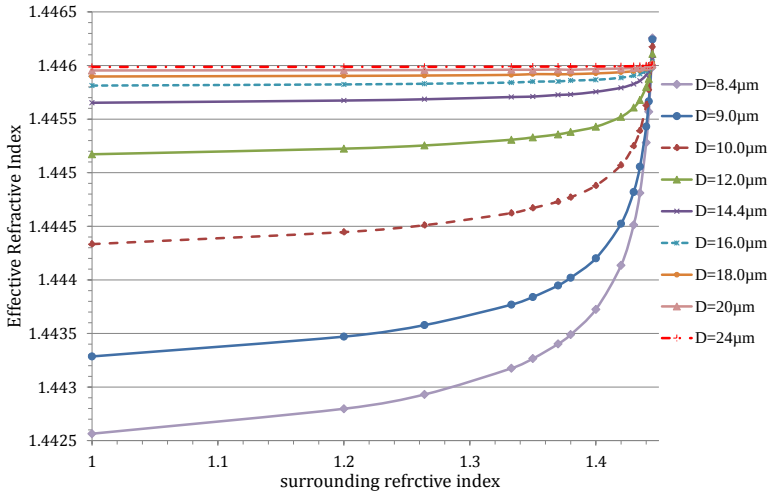

Figure 3.47: The relation of the n_{eff} with different surrounding medium indices for different optical fibre diameter.

On the other hand, from Eq.(2.11) described in Chapter 2 Section 2.2.1, using the following equation [21],

$$\frac{\Delta\lambda_B}{\lambda_B} = \frac{\Delta n_{eff}}{n_{eff}} \tag{5.2}$$

Which represents the sensitivity of the FBG, we were able to evaluate the amount of alteration numerically in effective refractive index difference Δn_{eff} as well as the shift of Bragg wavelength $\Delta\lambda_B$ in thinned-FBG for LP01 mode within the various diameters of fibre versus SRI as shown in Figure 5.8a, b. In Figure 8.5a, the Δn_{eff} as expected has the same trend as in Figure 5.7, showing higher sensitivity at thinned FBG ~ -3.5×10^{-3} at D_{fibre}=8.4 μm. For Figure 5.8b, it is clear that the Bragg wavelength is shifting toward shorter wavelength from Eq.(2.11), as the n_{eff} has reduced owing to a decrease in the inner-cladding diameter, where it approaches at D_{fibre}=8.4μm about -3.6 nm as a shift for n=1.0. Whereas at higher indices, for example n=1.445, the shift of λ_B has about +0.3nm, because the n_{eff} became higher again and the Bragg wavelength tends to shift back to a longer wavelength.

From Figure 5.8a and b, we see that the numerical analysis has a comparable match to the results that were obtained in Chapter 3 (Section 3.5.2), where, in a surrounding medium of BHF acid with concentration (20:1), the shift of Bragg wavelength numerically gives about ~2.9nm within the diameter of ~8.4μm at n_{SRI}=1.360 (BHF acid refractive index to be calculated in Chapter 6), compared with the experimental results of real monitor of etching a uniform FBG at calculated same etched diameter ~8.4μm we obtained measured Bragg wavelength shift was $\Delta\lambda_B$~2.7nm. However, we also obtained the last recorded wavelength shift before losing the FBG-sample as 3.3nm approximately, which confirms that we etched most of the cladding fibre and reached into the core (D_{fibre}~5.6μm) of the FBG while the fibre still in the BHF acid with concentration (20:1). However, the second etched FBG sample ($\Delta\lambda_B$~ 0.3nm at air n=1), in Section 3.6, coated with different solvents has revealed poor similarity with the numerical analysis but has shown a similar trend overall where the numerical simulation showed $\Delta\lambda_B$~ 0.25nm at air n=1 (Figure 5.8b). This is because the thickness of the etched-FBG sample was = 19.8±0.5 μm, which is still far from approaching a good observable effect on the fundamental Bragg wavelength (λ_{LP01}).

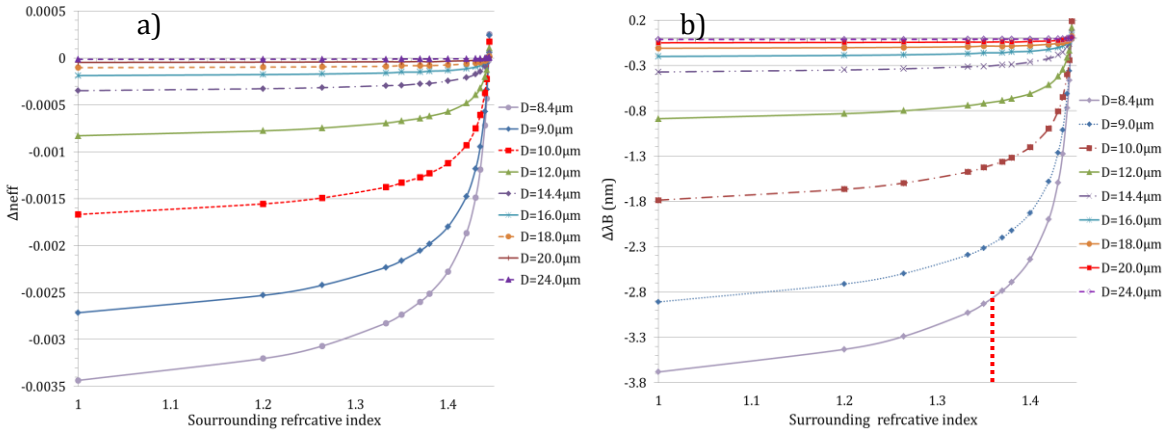

Figure 3.48: The relation of SRI for a range of optical fibre diameter in thinned FBG with; a) the change of effective refractive index Δn_{eff}. b) Bragg wavelength shift $\Delta\lambda_B$.

On the other hand, the reduced diameter of normal FBG changed the effective NA and increased the V-number (as explained before in Chapter 3) leading to generate other higher-order modes besides the LP01 such as LP11, LP21 and LP02. In Chapter 6, these higher-order Bragg resonances will be demonstrated experimentally and a numerical analysis by COMSOL, as well, will be presented.

5.5 Effective Nonlinear Coefficient γ_{eff} Optimisation

For the purpose of estimating the effective nonlinear coefficient γ_{eff}, and as it is the figure of merit of the fabricated CNTs based microfibre optical devices, we have done a numerical study for γ_{eff} based on Eq. (2.20) in Chapter 2 Section 2.5, as a function of fibre diameter for the same model of SMF-28fibre with the same parameters in Section 5.1 for a range of refractive indices of outer-cladding and different concentrations of dispersed CNTs, which are illustrated in Figure 5.9a, b, c and d.

Where a, b, c and d in Figure 5.9 depict the dispersed concentration of CNTs of 1ppm, 10ppm, 100ppm and 1000ppm respectively, to evaluate the effect of each one on the γ_{eff} at λ =1550.0nm. The numerical study is based on the effective nonlinear index $n_{NL\text{-}eff}$; which is obtained from the rate of the power fraction FMP (by using the model in Section 5.2) that is interacting with the n_{NL} includes in the coated fibre, where: core ($n_{NL\text{-}core}$ ~3×10^{-20} m^2/W), inner-cladding ($n_{NL\text{-}cladding}$ ~2.7×10^{-20} m^2/W) [124] and outer-cladding (CNTs-layer) ($n_{NL\text{-}CNTs}$ ~2×10^{-12} m^2/W)[125] as follow;

$$n_{NL-tot} = \Gamma_{core} n_{NL-core} + \Gamma_{in-cladding} n_{NL-cladding} + (\Gamma_{out-cladding} n_{NL-CNTs})m \qquad (5.3)$$

m is the concentration of the CNTs (ppm).The outer-cladding is a composite of CNTs/polymer; thus, the $n_{NL\text{-}eff}$ of the CNTs contributed with its applied concentration. Then, according to Eq. (2.20), $\gamma_{eff} = \frac{2\pi n_{NL-tot}}{\lambda A_{eff}}$ was optimised at λ = 1550nm and the effective area A_{eff} for an SMF-28 ~ 50μm². From this initial numerical study, we could observe noticeable and exciting values of γ_{eff} in low rates of CNTs concentration and quite high remarkable values at high CNTs concentrations, especially at 1000ppm.

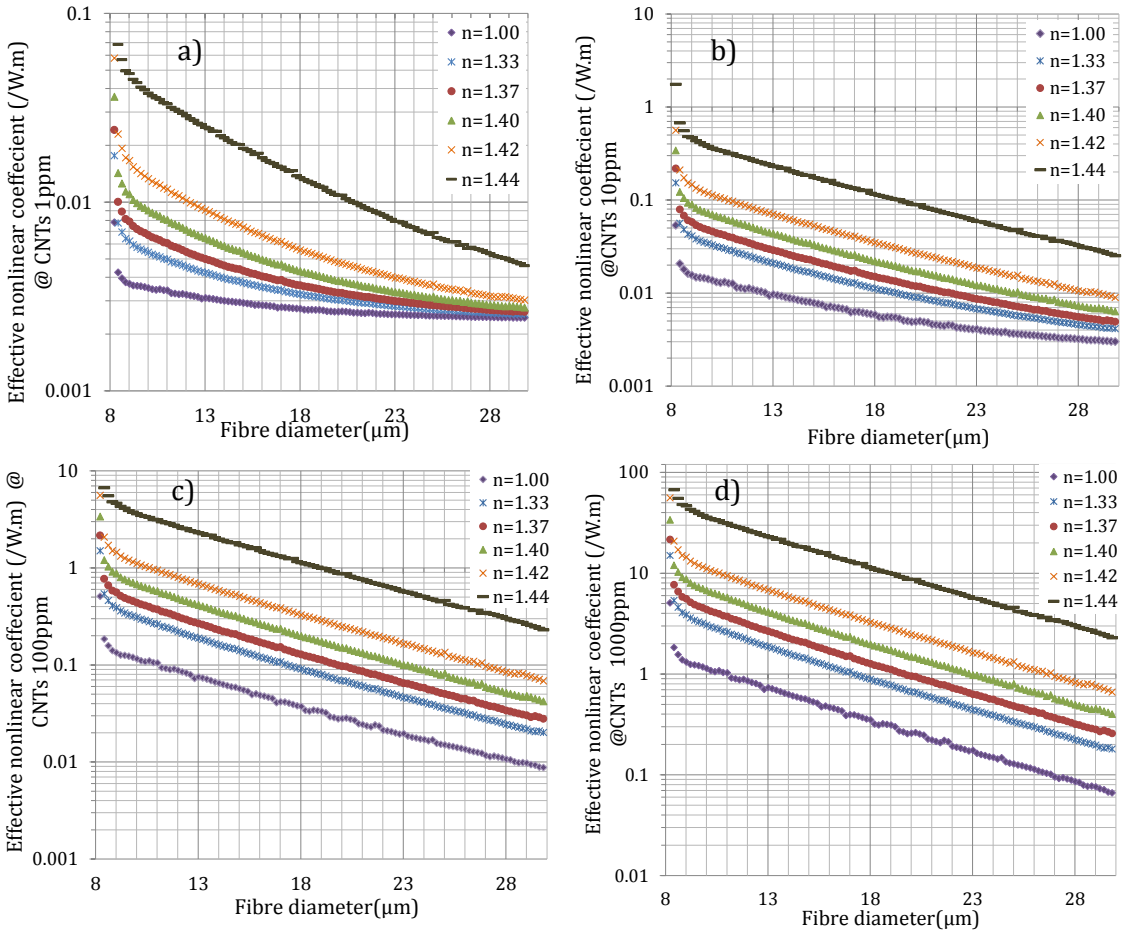

Figure 3.49: The effective nonlinear coefficient as a function of fibre diameter for a range of outer-cladding refractive indices of different concentrations of CNTs; a) at 1ppm b) at 10ppm c) at 100ppm d) at 1000 ppm.

Furthermore, the effect of applying different refractive indices of outer-cladding stimulatingly (Figure 5.9a,b,c and d) showed a rising trend of the γ_{eff} owing to the increase rate of the evanescent waves overlapping in the outer-cladding, as has been explored in Figure 6.5a in Section 5.2. This explains the interest of exploiting CNTs to coat etched optical fibre more than other materials. However, these high γ_{eff} might cause high loss for the fabricated fibre device, which is needed to investigate this point more; but tentatively, it is believed this could be controlled by applying polymer index to eliminate the losses.

5.6 The Effective Length and Nonlinear Coefficient Optimising for FWM in CNTs Coated Photonic Fibre Devices

Here we depict numerical simulation by MATLAB programming for estimating the conversion efficiency of FWM, which is the ratio of the converted wavelength power signal to the probe power signal or $\eta = (\gamma_{eff} L_{eff}\ P_{pump})^2$. Figures 5.10a and b show an estimation of the conversion efficiency of FWM η as a function of the pumped power reported for different effective lengths of optical fibre and for two different cases of effective nonlinear coefficient: γ_{eff} =1.15$W^{-1}km^{-1}$ (for silica fibre SMF-28) and γ_{eff} =1816.1$W^{-1}km^{-1}$(for coated optical fibre within CNTs as reported in [28]) as shown in Figure 5.10a and b, respectively. We can notice the rise in conversion efficiency of FWM proportionally with the increase of the launched pump power, an increase of the effective length, and a highly effective nonlinear coefficient.

From Figure 5.10a, at standard optical fibre with γ_{eff} = 1.15 $W^{-1}km^{-1}$, it is obvious that we obtained quite a low conversion efficiency η around -163 to -75 dB for L_{eff} = (5-30) mm and range of pumped power (0-35) dBm. Whereas in Figure 10.5b for higher γ_{eff}~1816.1 $W^{-1}km^{-1}$, the conversion efficiency η has shown an increase of around -100dB to -10dB with the same range of pumping power and effective length. This numerical analysis explains the inability of getting an observable idler signal for the FWM of the coated optical fibre-based device experiment (in Chapter 4) as the conversion efficiency of the FWM was below -45dB.

a)

b)

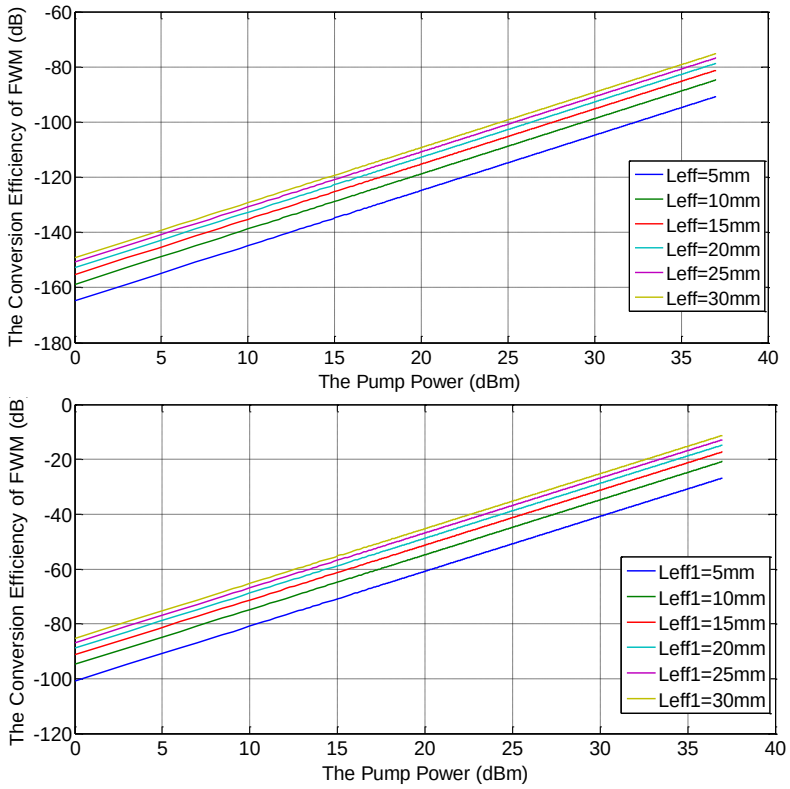

Figure 3.50: The conversion efficiency of FWM as a function of pumping power for different effective length of optical devices. a) For γeff ~1.15$W^{-1}km^{-1}$. b) For γeff ~1816.1$W^{-1}km^{-1}$.

In addition, Figure 5.11a and b indicate the conversion efficiency of FWM as a function of different γ_{eff} for a range of L_{eff}, for two pump powers of 20dBm (100 mW) and 30dBm (1W), respectively. We can observe that as expected, the conversion efficiency of FWM grows, with increasing the nonlinearity γ_{eff} of the applied coated optical fibre device as a maximum conversion efficiency of the FWM around -10dB and 10dB for P_{pump}=20dBm and P_{pump}=30dBm, correspondingly within the effective length range. As a result, from the numerical analysis, we can predict the gaining of an interesting conversion efficiency of FWM η with a highly effective nonlinear coefficient $\gamma_{eff,}$ and lengthen the effective nonlinear length L_{eff} of the fabricated device without the need to consume high pump power.

a)

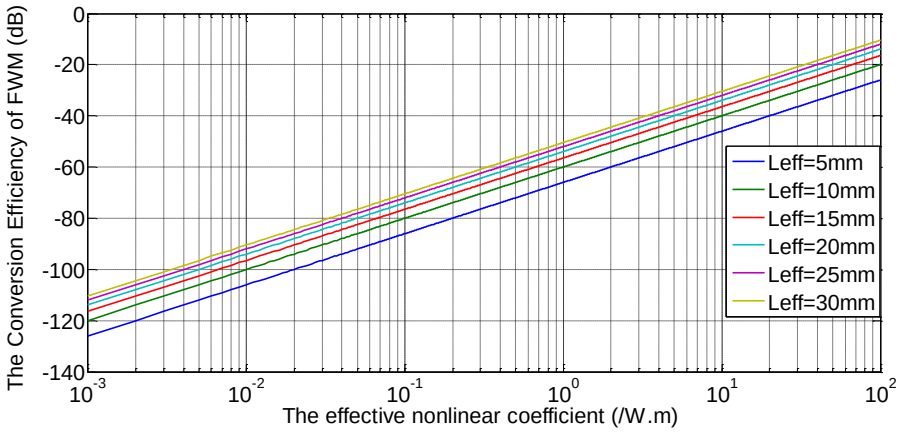

b)

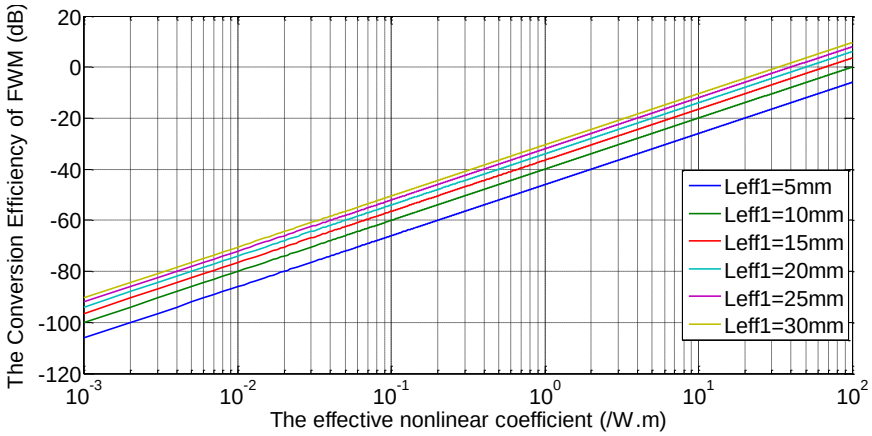

Figure 3.51: The conversion efficiency of FWM as function of the effective nonlinear coefficient γeff for different effective length of optical devices. a) For P_{pump}=20dBm. b) For P_{pump}=30dBm.

Alternatively, Self-Phase Modulation is another process that can be applied experimentally in order to optimise the fabricated devices. Besides, it is worth mentioning that the numerical study of FWM at a highly anticipated γ_{eff} for CNTs coated optical fibre resulted in remarkable values with less power consumption and shorter applied devices before carrying out the actual experiment. Regardless, considering the effect of losses is worthy of investigation, more experimentally and theoretically, in other future works to eliminate such drawback.

5.7 Conclusion

In summary, a simulation model for single mode fibre, using similar optical properties of SMF-28 with different diameters of silica cladding and for different surrounding indices was build and demonstrated by using COMSOL Multiphysics. A numerical evaluation was presented for the fraction of model power (FMP) (the extended evanescent field outside the fibre) within the outer-cladding in etched optical fibre as a function of different diameters and refractive indices of the surrounding. This numerical study was done for the fundamental mode as well as the higher-order modes; LP11, LP21 and LP02 and achieved more ability in controlling the rate of evanescent wave overlapping with the coated materials, such as CNTs, with different refractive indices especially the higher order modes. They revealed higher FMP of evanescent wave than the fundamental mode from 1% depth of overlapping with fibre diameters < 11μm and exceeding 10% within high refractive indices of the surrounding, which are interesting from a sensing prospect as well. Moreover, thinned FBG and the modifications that were obtained from the change of effective refractive index, shift of Bragg wavelength, and generated higher order modes in etched FBG were examined and illustrated numerically. The numerical results were corroborated by the experimental results and displayed good congruence. Furthermore, a numerical estimation of the effective nonlinear coefficient γ_{eff} in CNTs coated fibre devices for different CNTs concentrations (1ppm, 10ppm, 100ppm and 1000ppm) was demonstrated as a function of various diameters and applied refractive indices of outer-cladding of fibre optic based on the fraction of power within the outer-cladding in etched fibre interacting with the nonlinear refractive index of the coating layer of CNTs. Finally, a numerical simulation for evaluating the conversion efficiency of FWM anticipated by photonic microfibre devices coated with CNTs was studied under different pump powers (P_{pump} ~0dBm-37dBm) and effective nonlinear length (L_{eff} =5mm-30mm) of the coated microfibre devices at λ=1550nm exhibited a noteworthy theoretical estimation of conversion efficiency of FWM.

Chapter 6 : Optical Sensors Based on the Relative Shifts of Higher-Order Modes in Etched FBGs

6.1 Introduction

In the past two decades the uses of FBGs have expanded to numerous applications due to their merits, such as low insertion loss, fibre compatibility and compact design [19, 20, 126-128]. Optical sensing systems based on FBGs are used in many aspects for detection – mostly in strain, temperature, and pressure [129, 130] since it can be applied in harsh environments with a quick system of sensing [131, 132]. Recently, attention has focused on cladding-etched FBGs refractive index sensor as it provides higher interaction with the surrounding environment than the normal FBG, is adaptable, simple and has a low-cost technique. These sensors have found implementations in chemical and biological fields for measuring a variety of physical and chemical substance parameters, including various liquids and gases [18, 21, 41, 133, 134]. The sensor is based on evanescent mode-field interaction with the measurand to the surrounding ambience. Some other sensors are based on other different coating materials on the etched cladding surface for their promised potential, such as carbon nanotubes CNTs, graphene oxides GO, and gold. Here, the coating material interacts with the propagating evanescent field (overlapping) from the cladding-etched fibre Bragg grating surface, leading to sensors with much higher sensitivity enhancement – up to 10 times higher than uncoated micro-FBG, as has been reported for NO_2 gas sensing with a detection limit of 0.5 ppm with 0.8 pm/min sensitivity; for humidity, the limit of detection in the CNTs-coated etched FBG is ~0.03RH at λ=1550nm and room temperature [49, 135-137]. Furthermore, other proposed functions have been investigated, such as a tuneable filter based on CNTs-coated etched FBG to utilize the optical absorption characteristic of CNTs. It was able to shift the reflected peak of Bragg wavelength of CNTS-etched-FBG in proportion to the optical pump power with a detuning range of 2nm. Hence, the optical-power-dependent shift rate was reported is around 0.026 nm/mW [18, 30].

6.2 Simple Technique to Determine the Diameter of Etched Optical Fibres Precisely

In this section, based on the simple technique of measuring the differential relative shifts of the Bragg resonances between the fundamental mode (LP01) and the higher-order modes LP11, LP02, LP21, LP12, LP31, the technique to determine the fibre diameter in an etched FBGs is demonstrated. These modes exist, even in standard SMF-28 fibres, when the diameter is below ~20μm. In general, silica-based fibres are etched using HF acid with various concentrations ranging from pure HF (49%) to buffered HF solutions, depending on the required precision and final etch quality of the fibre surface. Thus, being able to precisely determine the evanescent field overlap with the measurand is vital when seeking a high precision of sensing or other fibre optic applications mentioned above. Some applications require a very specific evanescent field of overlap – less than a percent in some instances – to control the losses of the manufactured microfibre-devices sufficiently. In this case, it is essential to be able to control the fibre diameter precisely to ensure that the correct field overlap has been achieved. The evanescent field rate for each mode was investigated for different etched cladding fibre diameters and various refractive indices of surrounding mediums as demonstrated in Chapter 5.

For this purpose, it is beneficial to know the refractive index of the solution of HF acid in the etching process to obtain a precise measurement of fibre diameter, and this will be demonstrated later in Section 6.3. Previous work has also demonstrated fibre etching with HF to determine the fibre core diameter based on in-situ monitoring of the shift of the Bragg wavelength of the fundamental mode [138]. However, this was only reported for the case when the etching had reached the fibre core itself. In that work, the precision in determining the diameter outside the fibre core was not reported. In view of that, we also explore this concept further – but through the observation of the higher-order mode resonances of the Bragg grating.

This section has demonstrated the determination of the fibre diameter in an etched FBGs based on the technique of measuring the differential relative shifts of the Bragg resonances between the fundamental mode LP01, and the higher-order modes LP11, LP02, LP21, LP12 and LP31.

6.2.1 Theoretical Analysis and Simulation

The main principle of the Bragg gratings sensor written in silica fibre is that the resonance Bragg wavelength shifts due to any changes in the n_{eff} of the propagating mode (as in Eq. 2.11 mentioned earlier, in Chapter 2). Then, FBGs based on single mode fibre only support the LP01 when oscillating above the fundamental cut-off wavelength of the fibre. However, the process of etching of the cladding fibre results in a change of the effective refractive index (Δn_{eff}) of the propagating mode, prompting a shift in the reference Bragg wavelength λ_B, due to the decrease of the fibre diameter. This change of Bragg wavelength $\Delta\lambda_B$ is given by:

$$\Delta\lambda_B = 2\Delta n_{eff}\,\Lambda \tag{6.1}$$

As a result of this, the corresponding values of the normalized propagation constant *b* and V-number of the etched fibre will also be different from that of the pristine fibre, as shown in Figure 6.1. This in turn implies that, at that stage, fibre can start to support higher-order modes and thus, in the case when a Bragg grating is written in the fibre, can support higher-order Bragg resonances [36, 123], as illustrated in Figure 6.2. Since the different cut-off wavelengths of the modes, the evanescent field values of the LP01 and the higher-order modes LPxy are different. They are, thus, affected by the external refractive index to a different extent, as it will be displayed later in this chapter.

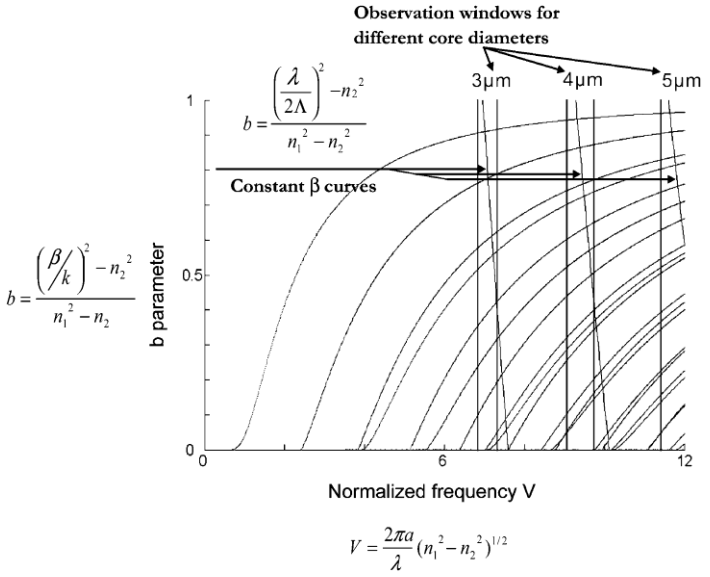

Figure 3.52: Normalized propagation constant as a function of V-number in FBGs, and illustrates the effect of altering the fibre structure on *b* parameter [36].

In view of that, the Bragg wavelength-shifts of these modes will be different, depending on the etched diameter of the FBGs and on the refractive index of the surrounding material. According to the Bragg resonance condition in Eq. (2.11.), the relative shifts, $\Delta\lambda_{LPxy}$, between the fundamental mode LP01 and higher-order LPxy modes can be expressed as:

$$\Delta\lambda_{LPxy} = 2\Lambda\left(n_{eff}^{LP01} - n_{eff}^{LPxy}\right) \tag{6.2}$$

where n_{eff}^{LP01} and n_{eff}^{LPxy} are the effective refractive index of the fundamental mode and higher-order modes, respectively. Theoretically, we have investigated this principle in Chapter 5 as illustrated in Section 5.2, Figure 5.5 and Figure 5.6. Therefore, from the simulated results of the different effective refractive indices, we are able to simultaneously predict the relative Bragg wavelength shifts for the fundamental mode and various higher-order modes, as will be shown in the next section (solid lines in Figure 6.4).

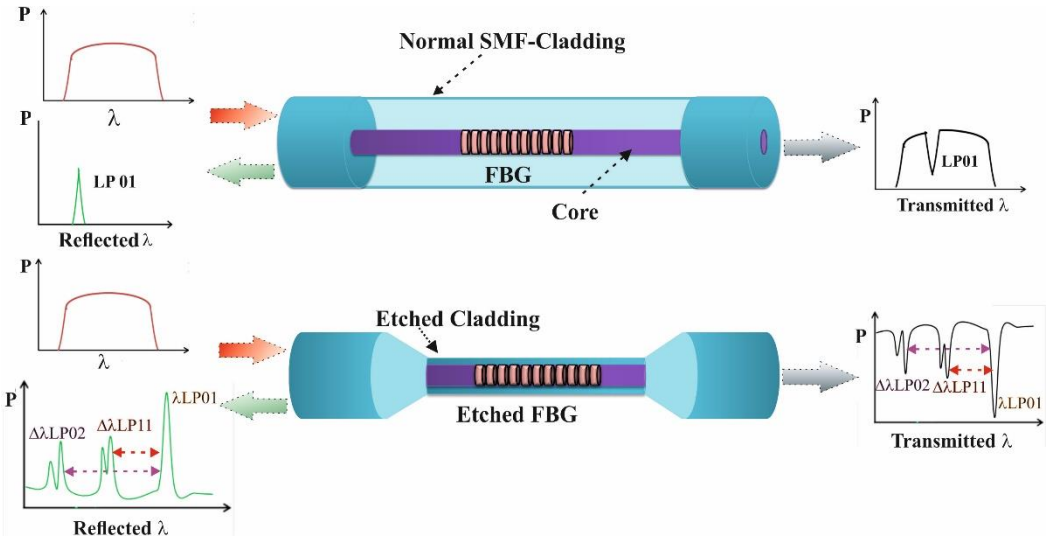

Figure 3.53: Schematic representation of a FBG before and after being HF acid etched.

6.2.2 Experimental Work and Analysis Results

In order to implement our simple technique, the schematic setup of the experiment is illustrated in Figure 6.3. The experiments are carried out using 8-10mm long uniform FBG written in single mode fibre SMF-28, with an initial wavelength of 1534.5nm, 1544.0nm, and 1560.0nm. The Bragg wavelength has a bandwidth around 0.2nm, with transmission loss up to 1.5dB (for the FBG with $\boldsymbol{\lambda_B^{LP01}}$= 1534.5 and 1544.0nm) and a bandwidth around 0.8nm and transmission loss up to 20dB (for the FBG with λ=1560.0nm). The grating is mounted in a Teflon/Plastic container (as shown in Figure 3.2 in Chapter 3) before being immersed in a BHF acid solution. Following the mounting, the etching process is carried out under controlled conditions; from temperature (T=20°C ± 0.5°C) and relative humidity (45% ± 5%).

The reflection and transmission spectra of the grating are monitored in real-time using a broadband source ASE source and an optical spectrum analyser (Agilent 86140B) with a nominal resolution bandwidth of 0.06nm. In order to substantiate the method under different chemical wet etching conditions; two different concentrations of BHF (20:1) and (7:1) were applied in the process of etch of silica-cladding FBG diameter.

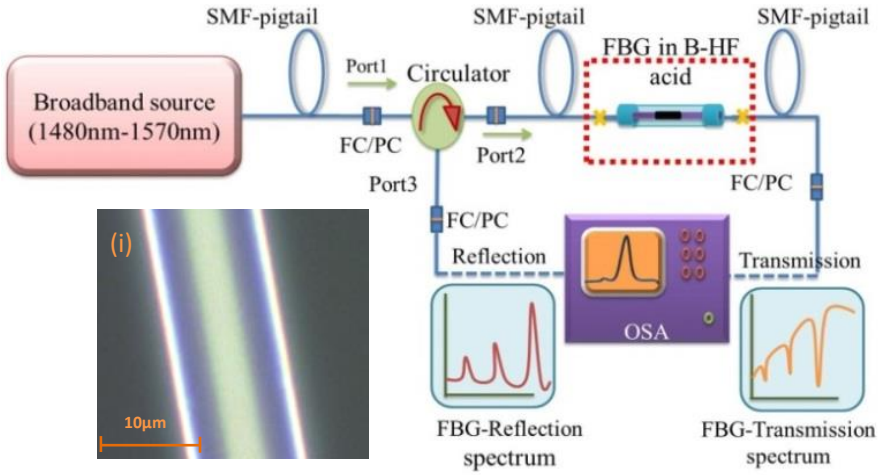

Figure 3.54: Schematic of the Experimental setup. On the left side a microscope image of etched uniform FBG based silica using BHF acid (20:1); i) D_{fibre}~11.0±0.2µm.

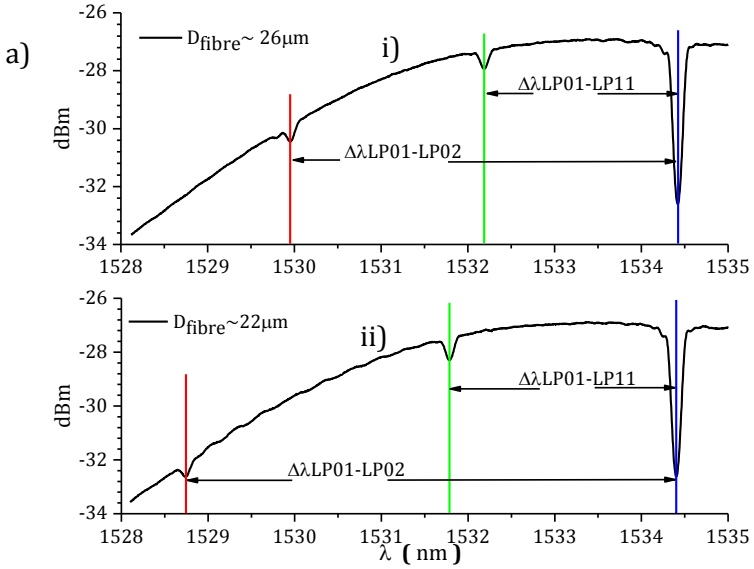

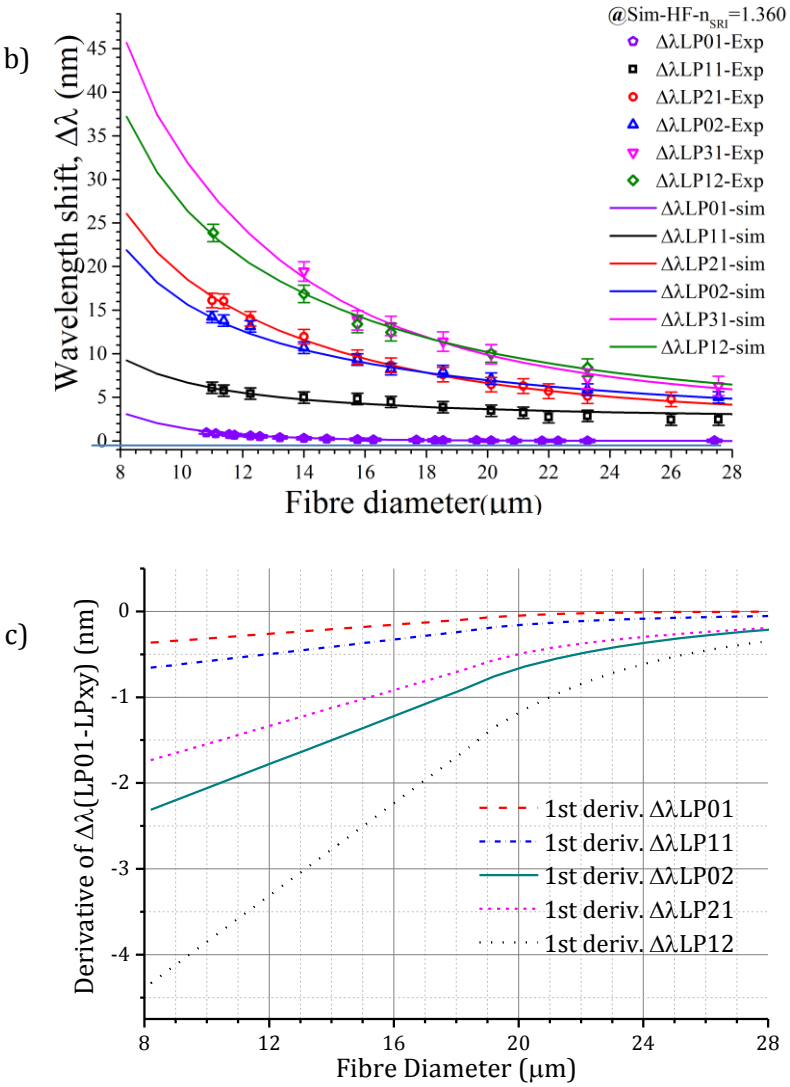

Figure 3.55: a) Transmission spectra of FBG of $\lambda_B^{LP01} = 1534.5nm$during real-time of etching process by BHF acid (20:1) experiment for two different stages of etching time and calculated etched FBG diameters D_{fibre}~26μm and 22μm (based of etching rate 4.5±0.1μm/hour). b) Measured (symbols) and simulated(solid-lines) results of the wavelength shifts against fibre diameter for the fundamental and higher-order modes Bragg grating resonances via BHF acid (20:1)at λ_B=1550.0nm. c) The first derivative of relative shifts of the higher-order modes and fundamental mode (ΔλLP01-LPxy) as a function of fibre diameter.

Figure 6.4a represents the experimental transmission spectrum of etching FBG$\lambda_B^{LP01} = 1534.5nm$, in-situ, monitoring the etch process by BHF acid (20:1) which is illustrating two different stages of calculated etched diameter of FBG under etch run (etching rate 4.5±0.1μm/hour). When the etched fibre approached a diameter >20μm, several Bragg grating resonances, including those of higher-order modes from; LP11, LP21, and LP02, show up in addition to the fundamental mode of Bragg resonance. However, It can be noticed from Figure 6.4a,i the two groups of higher order modes of Bragg resonances $\lambda_B^{LP11} = 1532.1nm$ and $\lambda_B^{LP02} = 1529.9nm$, are supported by the etched single mode FBG fibre with calculated diameter D_{fibre} ~26μm as obviously shown at the reflection spectrum while the etching process time was around 22hours. The two higher-order modes $\lambda_B^{LP11} = 1532.1nm$ and $\lambda_B^{LP02} = 1529.9nm$ have shown relative wavelength shift to the $\lambda_B^{LP01} = 1534.45nm$ (as shown in Figure 6.4a,i) about $\Delta\lambda_{(LP01\text{-}LP11)}$= 2.4nm and $\Delta\lambda_{(LP01\text{-}LP02)}$= 4.6nm, respectively. Then, Figure 6.4a,ii represents another experimental stage of etching time ~23 hours for the same FBG ($\lambda_B^{LP01} = 1534.5nm$) while still in the etching process, and the two group of the higher-order modes of Bragg resonances $\lambda_B^{LP11} = 1531.75nm$ and $\lambda_B^{LP02} = 1528.7nm$ have exhibited an apparent shift comparing to the LP01 Bragg wavelength by about $\Delta\lambda_{(LP01\text{-}LP11)}$= 2.7nm and $\Delta\lambda_{(LP01\text{-}LP02)}$= 5.7nm, respectively. These experimental results of the relative shifts of higher order modes at two D_{fibre} ~26μm and 22μm are close to what we get by the numerical simulation results as shown in Figure 6.4b. Hence, Figure 6.4b, which is show the theoretical (solid-lines) and experimental (symbols) results of the wavelength shifts of LP01 and other higher-order modes; LP11, LP02, LP21, LP12 and LP31 as a function of various diameters of etched FBG with SRI=1.360 (as BHF acid (20:1) refractive index to be determined later). At the completion of the etching process within etching rate about 4.5±0.1μm (for BHF acid with concentration (20:1)), where the targeted fibre diameter of D_{fibre} ~ 11.0±0.2μm was reached and the etching process was stopped. The observed Bragg wavelength shifts of LP01, LP11, LP02, LP21and LP31 relative to the Bragg wavelength of the un-etched fibre were, ~-0.97nm, -6.09nm, -14.21nm, -16.16nm, -23.86nm, respectively. The same technique was repeated with obtaining targeted diameter ~10.0±0.2μm at $\boldsymbol{\lambda_B^{LP01}}$=1560.0nm and observing the same wavelength relative shifts of higher-order modes of LP01, LP11, LP21, and LP02 were; ~-1.62nm, -6.87nm, -16.53nm, and -19.32nm. Within the measurement precision of the OSA these values are very well-matched with the numerical simulations for an index of the BHF of 1.360, as shown in Figure 6.4b. Furthermore, Figure 6.4c shows the derivative of the relative shifts between the fundamental mode and higher-order modes as function of different fibre diameter which is clearly shows how various the wavelength shift of each higher-order mode in relative to the LP01and the shifts are increases at thinner etched FBG diameter.

6.3 Determination of the Refractive Index of 20:1 and 7:1 BHF Solutions

It is beneficial to know the refractive index of the solution of HF acid in the etching process as it is a vital factor to obtain a precise measurement of etched fibre diameter. There are several reports on measuring the refractive index of HF acid by using Mach Zehnder interferometric and reflectometric measurements in the short and longer wavelength ranges [21, 139, 140]. On the other hand, it is also a method to calibrate and apply the etched FBG as a sensor of refractive index. Therefore, the obtained etched FBG samples from the experiment mentioned above (D ~ 11±0.2μm and ~10.0±0.2μm) were used in conjunction with a range of liquids with well-known refractive indices, such as water (1.318), methanol (1.317), acetone (1.351), ethanol (1.352), isopropanol (1.374) and ethylene glycol (1.420) (at λ~1550nm). The setup in Figure 6.2 was used and the BHF acid in the Teflon container was changed by instead applying the other solvents that were mentioned above. The resulted wavelength shifts of the fundamental mode LP01 is shown in Figure 6.5a. These results occurred when the concentration (20:1) of BHF acid was applied in the etching process, and it revealed a refractive index of 1.360±0.005 $\boldsymbol{\lambda_B^{LP01}}$ =1534.5nm and 1560.0 nm.

Adding to that, as a way to substantiate our concept more, and as a way to identify the refractive index of HF acid with different concentrations, we repeated the same experiment with the same setup, except with a different concentration of BHF acid with (7:1). The targeted diameter at the end of etch was ~10μm. The obtained etched silica-cladding fibre at the end was ~9.7μm. In Figure 6.5a and b, we compare the obtained differential shift between the LP01 and LP11 modes for both different concentrations (20:1) and (7:1) with diameters ~11.0μm, 10.1μm and 9.7μm, respectively. The experimental results were corroborated by simulations and again displayed excellent agreement for both cases of BHF acid concentrations (in Figure 6.5a and b).

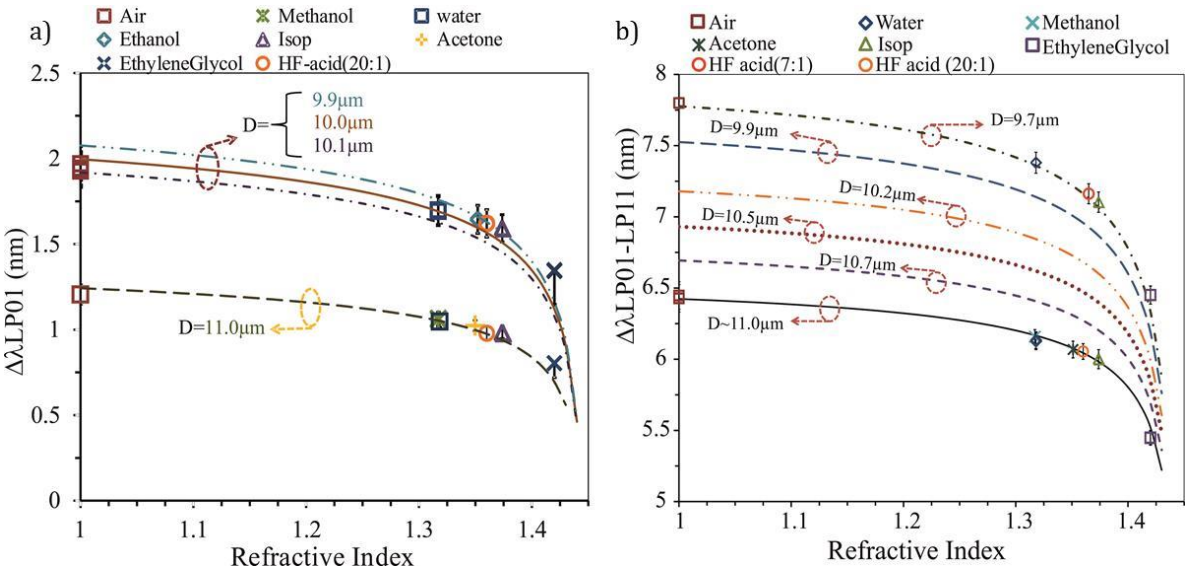

Figure 3.56: Measured and simulated results of relative wavelength shifts of; (a) LP01 mode at $\boldsymbol{\lambda_B^{LP01}}$=1534.5nm and 1560.0nm with D_{fibre}~11.0±0.2μm and ~10.0±0.2μm, respectively, via BHF acid (20:1), (b) LP11mode at $\boldsymbol{\lambda_B^{LP01}}$=1534.5nm (black-solid line) and $\boldsymbol{\lambda_B^{LP01}}$=1544.0nm (other coloured-dashed lines), against different external refractive indices applied at etched FBG with D_{fibre}~11.0±0.2μm via BHF acid (20:1) and D_{fibre}~9.7±0.2μm via BHF acid (7:1).

The same was also observed in the other etching processes of FBG, and higher-order modes Bragg resonances was also observed, as illustrated in Figure 6.5b. For instance, LP11 at D~11.0±0.2μm at $\boldsymbol{\lambda_B^{LP01}}$=1539.3nm shows relative wavelength shifts for a range of labelled solvents with refractive indices: air = 6.48nm, water = 6.13nm, isopropanol = 6.01nm, and ethylene glycol = 5.50nm. As a result, the refractive index of BHF acid with concentration (20:1) has been determined to be ~1.360±0.005 since $\Delta\lambda_{LP01\text{-}LP11}$= 6.06nm, which is comparable to the simulation result. Additionally, another etched FBG sample with D~ 9.7±0.2μm shows a relative shift difference for a range of solvents with different refractive indices: air = 7.80nm, water = 7.40nm, isopropanol = 7.10nm and ethylene glycol = 6.48nm, as illustrated in Figure 6.5b. For this, we were able to identify the refractive index of BHF acid with concentration (7:1) to be ~ 1.370±0.005 at $\boldsymbol{\lambda_B^{LP01}}$=1544.0nm.

It is worth mentioning that we applied an efficient and simple method for sensing the refractive index of unlabelled solutions due to the precision of determining the diameter of the etched FBG sensor (based on the same technique) within 0.2μm – and this is proven by the experimental results corresponding to the numerical simulations, as shown in Figure 6.5 a and b.

6.4 Salinity Sensor Based on the Relative Shifts of Higher-Order Modes in Etched Fibre Bragg Gratings

The measurement of water salinity has become an important parameter to control manufacturing industries and marine environments since salinity is a crucial parameter for protecting and preventing pollution in the ocean and global environment [50, 141]. Sensors based on evanescent mode-field interaction have emerged as one of the key components of the modern engineering practice, aimed at providing vital information about the measurand. Cladding-etched FBG sensors are being used for diverse applications for a precise detection of a variety of physical and chemical substance parameters, such as water pollution. Additionally, due to their immunity to electromagnetic interference, compatibility, small size, higher sensitivity and low losses, they are preferred as precise sensors. Previous works have reported salinity and temperature sensors based on Bragg wavelength shift of the fundamental mode (LP01) in the etched core of FBGs [50, 141]. In this section, based on simple, low-cost, efficient, and yet, precise technique in fabricating a highly sensitive refractive index as well as temperature sensor, we propose a water salinity sensor based on the relative shifts of the higher-order modes resonances (LP11, LP21, LP02) in an etched silica-cladding of a uniform FBG.

6.4.1 Experimental setup and work

An experimental setup was established in order to perform the salinity sensing, as shown in Figure 6.6. The experimental setup consists of broadband of ASE with a range of 1480nm-1570nm, an OSA (Agilent 86140B) with a resolution bandwidth of 0.02pm, and a circulator to monitor the reflection spectra of the grating. The setup employed a 10mm long cladding-etched FBG written in an SMF-28 fibre with an etched diameter of 10.2μm ± 0.2μm and $\boldsymbol{\lambda_B^{LP01}}$=1560.2nm. This sensor fabricated from a uniform FBG etched chemically via BHF acid with concentration (20:1), in-situ, was monitored based on an efficient technique of determining the targeted diameter with a high precision (<200nm), reported in our previous work mentioned above [142, 143]. The etched-FBG and a reference arm from a thermometer, both were mounted in parallel in a metal container filled with 100mL of DI-water and was put on a digitally controlled hot plate for a thermal reassessment of the liquid with two

temperatures, 22°C and 35°C. We utilized sodium chloride (NaCl) mixed with the DI-water with a range of concentrations, from 0 to 28g/100mL and refractive index range= 1.318-1.360 (based on the comparison of experimental and numerical simulation in next Section), to characterize the proposed sensor (D~10.2±0.2μm) by measuring the wavelength shifts of its fundamental mode (λ_B^{LP01}=1560.2nm) and the higher-order mode (λ_B^{LP11}=1552.6nm), relative to the LP01. The other groups of higher-order modes from LP21, LP02 were weakly excited and it was not easily measurable due to the high noise floor of the reflection spectrum. However, we repeated the experiment with other etched FBG samples, which had stronger reflected spectrum and with λ_B=1562.0nm and etched diameters ~10.0±0.2μm and ~9.2±0.2μm. We applied the same experiment procedure mentioned above to sense the DI-water salinity concentration, and NaCl was mixed with the DI-water, in a range of concentrations from 0 to 14.2g diluted in 100mL.

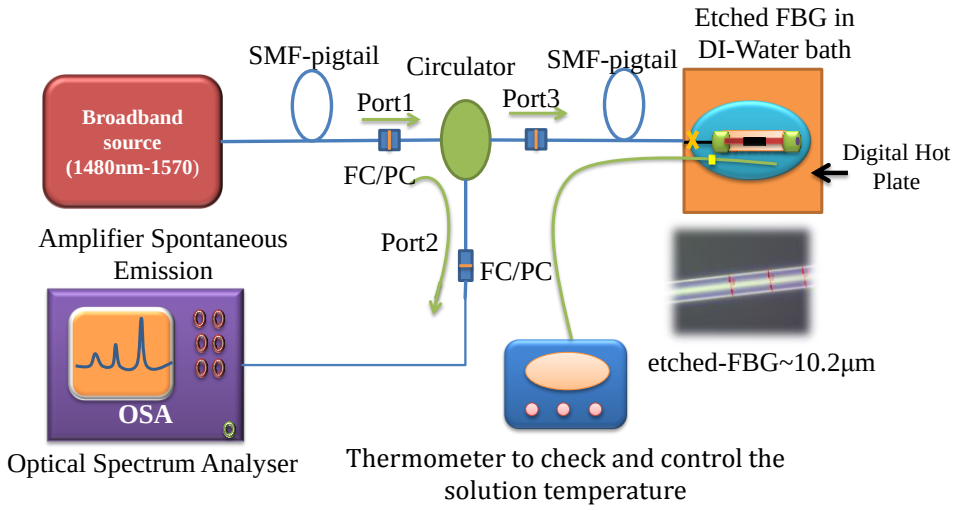

Figure 3.57: Experimental setup of water salinity sensing based on etched FBG.

6.4.2 Results and Discussion

From those sets of experiments, we conclude that the change of RI of the salinity solution based on the ΔλLP11-LP01 shows a sensitivity of around 3.43nm/RIU and 2.94nm/RIU for ΔλLP01, with T=22°C, as shown in Figure 6.7a and Figure 6.8a and b. The experimental results were corroborated by simulations and again displayed excellent agreement within accuracy R^2~0.99 and R^2>0.97 – for simulation and experimental results, respectively (as shown in Figure 6.7a, b and Figure 6.8a, b). Figure 6.7b illustrates the differential relative shifts of the Bragg resonances between LP01 and the higher-order mode (ΔλLP11-LP01) variation due to the upsurge of salinity concentration (%). This is due to change of the refractive index of the water with sensitivity ~ 10^{-4}. Note that we obtained the measurements with two natural environmental temperature T=22°C and 35°C. As mentioned, we repeated the experiment with two other etched FBG (D~10.0±0.2μm and ~9.2±0.2μm) and for a

different range of salinity concentrations, as demonstrated in Figure 6.9a and b. We achieved an obvious higher-order mode Bragg resonance of LP02, regardless of the LP11 and LP01 in both the etched FBGs with a similar environmental temperature mentioned above. Hence, the ΔλLP02-LP01 shows a sensitivity of around 18.8 nm/RIU and 12.0nm/RIU for etched FBG, with diameters D~9.2±0.2µm and 10.0±0.2µm respectively at $\boldsymbol{\lambda_B^{LP01}}$=1560.0nm, as presented in Figure 6.9a, b, c and d.

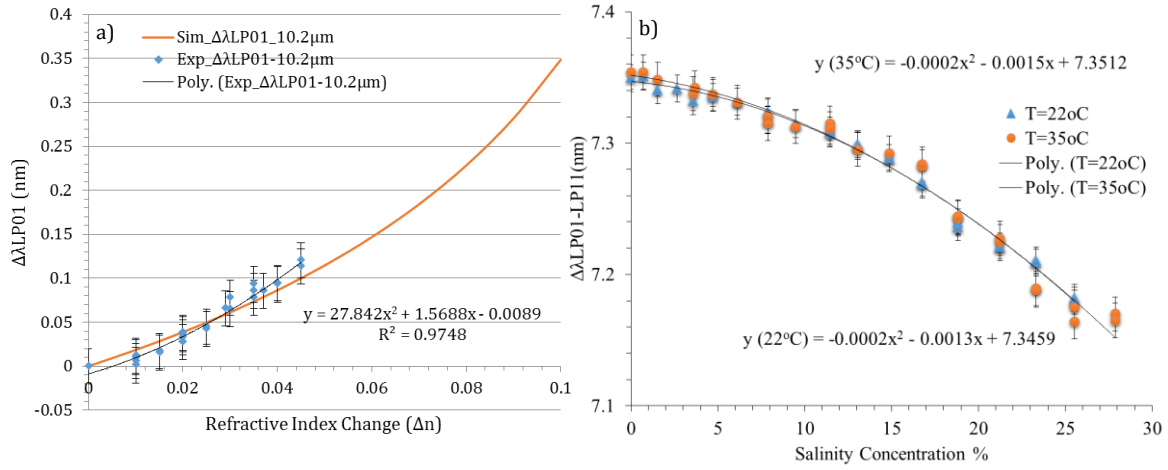

Figure 3.58: a) Measured and numerical results of the LP01 Bragg wavelength shifts for refractive index change Δn of DI-water salinity at λ_B^{LP01}=1560.2nm. b) Measured results of the relative wavelength of Bragg resonance shifts between the LP01 and LP11 versus different salinity concentrations and solution temperatures T=22°C and 35°C.

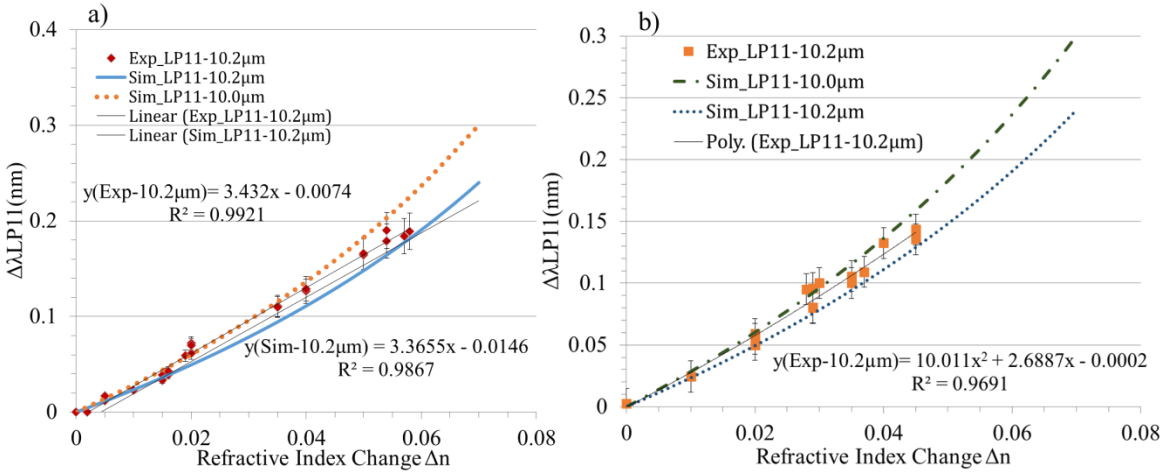

Figure 3.59: Measured and simulated results of the relative wavelength shifts of the higher-order mode LP11 in the etched FBG against relative refractive index changes Δn of DI-water salinity for two different samples; a) etched-FBG sample1. b) etched-FBG sample2.

Again, the numerical simulation has a comparable agreement with the experimental results, within accuracy of R^2 ~0.99 for experimental and simulation results correspondingly as illustrated in Figure 6.9a and b. Furthermore, from Figure 6.10 a, b, c, and d, the numerical simulations for the relative shifts of Bragg resonances of LP01, LP11, LP21 and LP02 in etched-Silica-cladding FBG for different fibre diameters and range of refractive index change (Δn) are expected to be of higher sensitivity than only the LP01 and further experimental data for these higher-order modes has been presented.

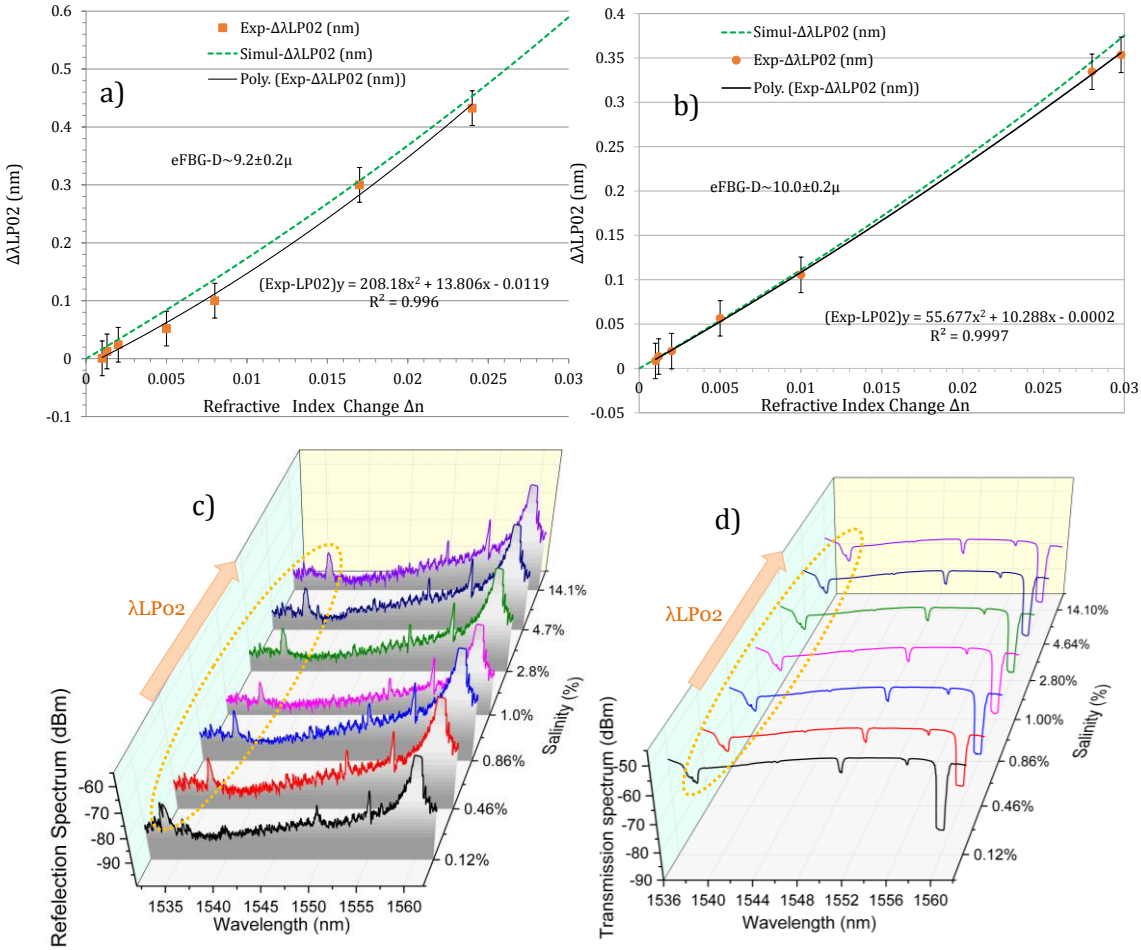

Figure 3.60: Measured and simulated results of the relative wavelength shifts of the higher-order mode LP02 in etched FBG against relative refractive index changes Δn of DI-water salinity for two different samples; a) D~9.2±0.2μm . b) D~10.0±0.2μm. The reflection spectra for a range of Salinity concentrations from 0.12g to 14.1g diluted in 100 mL of DI-water, for e-FBG with two different diameters; c) D~9.2μm and $\boldsymbol{\lambda_B^{LP02}}$ =1535.93 nm. d) D~10.0μm and $\boldsymbol{\lambda_B^{LP02}}$=1538.10nm.

Again, the numerical simulation has a comparable agreement with the experimental results, within accuracy of R^2 ~0.99 for experimental and simulation results correspondingly as illustrated in Figure 6.9a and b. Furthermore, from Figure 6.10 a, b, c, and d, the numerical simulations for the relative shifts of Bragg resonances of LP01, LP11, LP21 and LP02 in

etched-Silica-cladding FBG for different fibre diameters and range of refractive index change (Δn) are expected to be of higher sensitivity than only the LP01 and further experimental data for these higher-order modes has been presented.

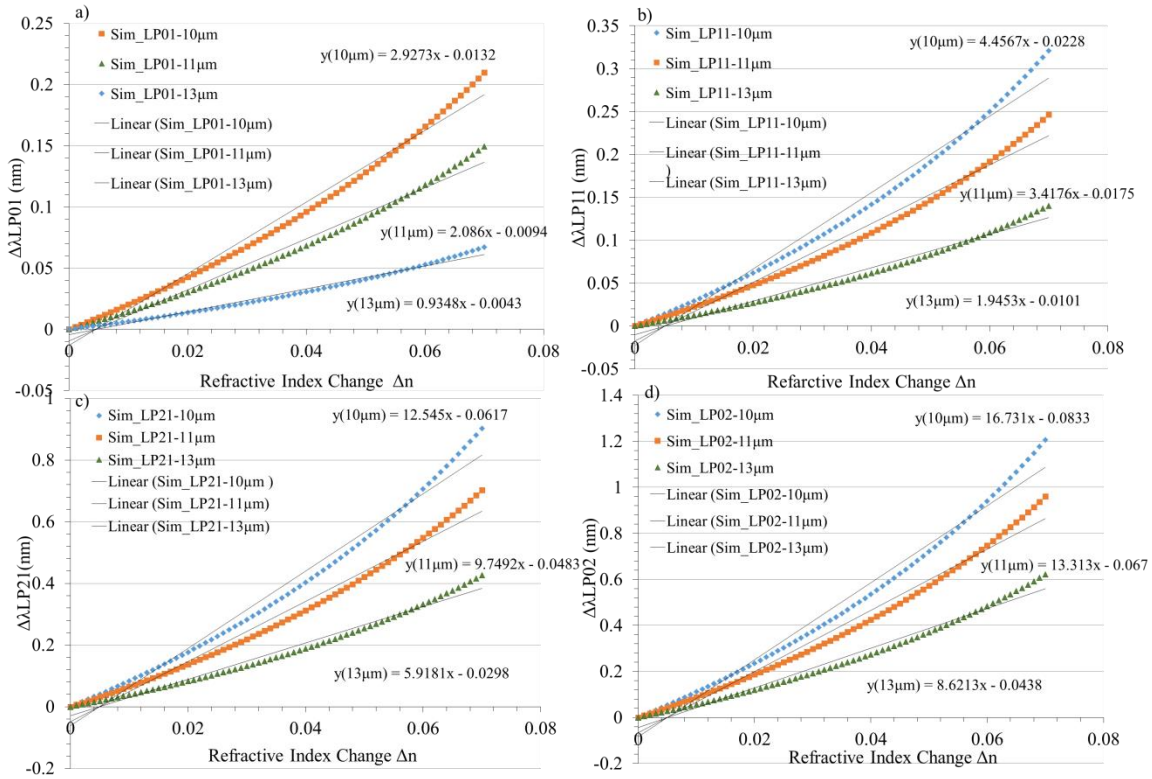

Figure 3.61: Simulated results of relative wavelengths shifts Δλ of (a) LP01 mode, (b) LP11 mode , (c) LP21 mode , (d) LP02 mode, against range of refractive index changes Δn and various diameters; 10.0μm, 11.0μm, 13.0μm at $\boldsymbol{\lambda_B^{LP01}}$= 1560.0nm.

6.5 Conclusion

The study of generated higher-order modes in etched silica-cladding FBG presents an interesting research area as it can offer an enhancement in sensing. In this chapter, a functional method based on observing the differential relative wavelength shifts between higher-order modes and the fundamental mode in an etched FBG was demonstrated and explained. A simple technique to determine the diameter of etched fibre based on the relative shifts of Bragg resonances in etched FBG was demonstrated experimentally and theoretically. This potential method has revealed a high precision to attain the targeted diameter, in-situ monitoring about 200nm. Based on the same technique of fabricating a precise refractive index sensor based on the etched silica-cladding FBG, the refractive index of BHF acid solution with two different concentrations (20:1) and (7:1) were determined to be 1.360±0.005 (at λ=1550.0nm) and 1.370±0.005 (at λ=1544.0nm), respectively. Furthermore, based on this precise technique in fabricating a highly sensitive refractive index as well as

temperature sensor, a water salinity sensor based on the relative shifts of the higher-order modes resonances in etched uniform FBG written in single mode fibre was investigated experimentally and theoretically. The higher-order modes from LP11 and LP02 have achieved an interesting sensitivity to the concentrations of salinity for the range of 28g/100mL and 14.1g/100mL in DI-water concentrations about 3.43nm/RIU and 18.0nm/RIU, respectively. The experimental results were substantiated by simulations and again displayed excellent agreement within accuracy $R^2 \sim 0.99$ and $R^2 > 0.97$ for simulation and experimental results, respectively.

Chapter 7 : Conclusion and Outlook

7.1 Conclusion

This work investigated the design, fabrication, and applications of photonic fibre devices that are based on the evanescent field interacting with the surrounding medium in terms of non-linear coated materials (i.e. CNTs) and implemented as micro-optical sensors.

- In this thesis, Chapter 3 and 4 are focused on the design and fabrication of non-linear all-optical fibre devices based on CNTs. The main approach of fabricating thinned photonic fibre devices was through the wet chemical etching process. Experimentally, in the wet etching process, a BHF acid solution (with two different concentrations (20:1) and (7:1)) was utilized to etch the silica-cladding of SMF-28. Some factors affected on the consistency of the etching rate of BHF acid for both concentrations were manged to be solved either by; enhancement the design of the container was used during the etching process, and control the environmental conditions during the etching process (i.e. temperature and relative humidity %). The BHF acid solution was characterised and the etch rate/diameter reduction in silica-cladding fibre was obtained for both concentrations (20:1) and (7:1) and found to be 4.5±0.1μm/hour and 12.0±0.2μm/hour, respectively. Furthermore, the insertion loss of the resulting etched SMF-28 was optimised to an average of less than 0.8±0.2dB at λ=1550. In contrast, the BHF with concentration (7:1) showed a higher insertion loss of about 1.7±0.2dB due to the formation of a double transition region in the etched fibre caused by the policy working hours of the cleanroom (when we targeted etched diameter <16μm). However, the optical quality of etched surface with (7:1) was quite comparable to the BHF concentration (20:1) in terms of smooth, uniform and robustness etched fibre.

- In addition, a real-time monitoring of the etching process for a standard optical SMF-28 fibre and uniform FBG was carried out. This resulted in a similar drop for both SMF-28 sample and the uniform FBG sample (SMF-28 and FBG (λ_B=1553.14nm)) of the transmitted power by 1.7±0.2dB, since we etched into the fibre core itself. Also, the etched FBG ($D_{fibre} \sim 5.8\pm0.5\mu m$) showed about 3.3nm shift of Bragg wavelength as all the cladding were etched into the fibre core, which has been backed up with the simulation results. The etched single mode fibre started to support higher-order modes due to reduction the thickness of the fibre diameter and in parallel the optical properties of the fibre. Based on the experimental results and numerical calculations obtained from the real-time monitoring of etching process by BHF acid (20:1), in term

of the etched FBG sample (λ_B=1553.14nm), the reflectivity of the etched FBG enhanced by average 0.4±0.02 besides the rate of the power confinement of the fundamental mode in the fibre core of etched FBG increased from 0.75 to 0.95 after etched D_{fibre} <15μm. Furthermore, the Bragg wavelength of the etched FBG sample (λ_B=1553.14nm) shifted 3.3nm in the longer wavelength shift that it believed to be resulted of either from the exothermic properties from the chemical reaction between HF acid and and the FBG or the contribution of non-adjustable setup of the FBG caused a rise of strain effects along the weak etched area.

- Another uniform etched FBG (D_{fibre}=19.8±0.5μm) was examined experimentally and numerically, which resulted in observing a higher-order mode, i.e. LP11, besides the LP01 mode. A small shift of Bragg wavelength for LP01 was obtained (ΔλLP01~0.3nm) while LP11 showed an obvious wavelength shift of Bragg resonance relative to LP01 (ΔλLP11~5.0nm). Furthermore, in this etched FBG, a good sense contribution to different surrounding solvents indices was achieved by the higher order mode LP11 when compared to the fundamental mode, which was too limited to be noticed. Numerical simulation results showed a few similar matches with the experimental ones, and were presented in Chapter 5.

- A detailed description of a simple technique of the optical deposition of CNTs for etched fibre based devices was presented in Chapter 4. In this process, two different dispersed CNTs mixed solutions were used to coat the etched silica-cladding of the fibre: first, CNTs/DMF solution, and then, CNTs/DI-water with 2% of SDS mixed solution. The latter mixed solution was assorted and prepared in our laboratory. This solution proved to have a longer efficient lifetime, with consistent and untangling dispersed CNTs being used instead of the commercial mixed of CNTs/DMF solution. The coated etched fibre samples that resulted after the process of optical deposition of CNTs dispersed in DMF solution, were very lossy where in some coated fibre samples the IL exceeded 60 dB due to the interaction between the evanescent wave and the CNTs dispersed in the DMF polymer mix solution led to absorption loss and light scattering. Another factor investigated during the optical deposition was the optical deposition time impact on the optical loss which is showed inconsistency effect on the optical loss (or IL) of the fibre samples embedded with CNTs in our setup work. Another point that it is believed is attributed to the insufficient dispersion of CNTs around the etched fibre samples was the shelf-life limitations (<3months) of the commercial mix solution of dispersed CNTs in DMF The time of deposition, the diameter thickness of the coated etched fibre, the dispersed CNTs mix solution that was applied, the insertion losses of the fabricated fibre coated devices and the

injected power during the optical deposition process were all examined and characterised in many aspects and different etched fibre samples experimentally. Because of the un-methodical trend of the deposition results for the photonic fibre coated devices, this resulted in inefficient fabricated non-linear all-optical photonic fibre devices coated with CNTs, and was not achieved to the level expected. Nevertheless, the optical loss of some coated fibres still high (>14dB) due to the light scattering and absorption loss by CNTs, which also believed was associated with the injected power to the fibre samples escalated to ~23dBm-27dBm, and formation of CNTs agglomeration on one side middle section of the etched fibre. Adding to that, we abled relatively, to reduce the optical losses in most of the fibre samples caused by the coated layer of CNTs by applying low index polymer (n=1.37) due to the effect of light scattering and coupling out of more evanescent wave were minimized since the propagating mode becomes more guided by the low index polymer (>air=1). Furthermore, the resulted fibre samples embedded with CNTs after check under microscope were non-uniform CNTs depositions around the etched surface of the standard fibre; a periodic cluster formation, as a result of CNTs deposition layer along and around the etched section of the fibre, was the observed trend after each optical deposition process.

- Furthermore, an optical fibre FWM experiment was implemented near λ=1550nm to characterize and optimize several fabricated photonic fibre devices (D_{fibre}=16.0μm and 19.0μm) coated with CNTs. One coated fibre samples (D_{fibre}= 16.0μm) showed a very weak four-wave mixing at λ=1550nm and generation of new wavelength (λ_{idler}=1551.240nm and SNR~1.8dB) with conversion efficiency ~-39dB and calculated effective nonlinear coefficient ~ 1122 W^{-1} km^{-1} for pump power ~27dBm and for effective length L_{eff} <22mm which is lower than other reported results[28, 117]. While, four-wave mixing effect was not obtained from the second coated fibre sample (D_{fibre}= 19.0 μm) because of thickness of the etched fibre, hence less rate of evanescent wave that interacting with the nonlinearity of the embedded CNTs besides the optical loss of the fabricated coated fibre (~2dB) and lack of CNTs dispersed along the etched fibre. We were not able to observe incompetent four-wave mixing effect due to the difficulties in adopting suitable SWCNTs and designing suitable configurations for SWCNT-light interaction with evanescent wave of etched fibre samples. Hence, that resulted in unobserved idler signal and sufficient nonlinearity for the following possible factors, along with those mentioned above;
    - i- the high insertion losses of the fibre devices were used (>92% of power loss)
    - ii- the limited amount of the deposited CNTs on the etched surface of the fibre.

The fabricated photonic fibre devices deposited with CNTs with D_{fibre}~ 13.5μm (IL~-27dB) were examined experimentally as a saturable absorber. The coated fibre revealed a noteworthy suppression (~23 dB) to their insertion loss when a CW high input power (Pin~27dBm) was launched at λ= 1550.0nm. Whilst by injecting pulse power output average ~ 27dBm (peak power ~5 W) resulted on unnoticeable drop in loss and SA effect due to a thermal damage by the high input power and degradation of the optical properties of the embedded nanotubes as other reported [115, 120]. Furthermore, another two CNTs/SDS coated fibre both with D_{fibre}~ 10.0μm (IL= 17.1dB), and 12.0μm (IL=24dB) with etched length= 10mm for both, investigated at λ=1550nm as SAs showed a weak drop in the optical loss ~0.7 dB and 3.5dB, respectively, at high injected power >25dBm associated to the poor amount of coated layer of CNTs embedded on the etched surface of the fibre samples.

- In Chapter 5, a numerical model for SMF-28 fibre was demonstrated. This model studied the alterations that occurred in thinned silica-cladding of single mode fibre. In addition, the power fraction rate that is coupling at the outer-cladding in etched fibre was estimated as a function of different fibre diameters and refractive indices of the outer-cladding at different modes LP01, LP11, LP21, and LP02. Therefore, we were able to precisely determine and control the rate of the evanescent field overlapping with the surrounding material, specifically for a high precision of sensing or nonlinear fibre optic applications mentioned above. From the simulations were done to the model, we found that etched single mode fibres with diameters <20μm are more likely to support higher-order modes besides the fundamental mode. This resulted from the altered values of NA, V-number and subsequently the *b* of the etched fibre. A numerical optimisation for the n_{eff} and Bragg wavelength shift with different SRIs for various diameters of FBG were studied and revealed interesting Bragg wavelength shifts for LP01.

- Furthermore, a numerical study of the effective non-linear coefficient as a function of the fibre diameter and different SRIs were carried out, anticipating remarkable values of nonlinearity for different concentrations (from 1ppm to 1000ppm) of dispersed CNTs at λ=1550nm. Then, the conversion efficiency of FWM as a function of pump power, effective length and effective non-linear coefficient has been explored numerically, demonstrating that conversion efficiencies as high as ~10dB at highly effective non-linear coefficient and extend the effective non-linear length few centimetres of the fabricated devices without the need to consume a high pump

power. These tentative theoretical results for FWM have been done without considering the loss factor in the fabricated device, which needs to be probed later, both experimentally and theoretically.

- Furthermore, an optical sensor based on the relative shifts of higher-order modes in etched FBGs was examined and demonstrated in Chapter 6. A simple technique based on observing the differential wavelength shifts between higher-order modes in an etched Bragg grating to determine the refractive index of the BHF (20:1) acid solution is ~1.360 ±0.005 (at λ=1534nm and 1560nm), and with concentration (7:1) is ~ 1.370±0.005 (at λ=1544.0nm) were presented. We have applied this technique to a number of gratings with different specifications in the C-band wavelength region. Besides, relying on that technique, we being able to determine the etch diameter of the optical fibre with a precision of ~200nm for diameters below ~20μm, via the etching process of cladding fibre of FBG, in–situ, monitoring the etching process. Moreover, relying on the same concept and the precise technique in fabricating a highly sensitive refractive index sensor, a water salinity sensor based on the relative shifts of the higher-order modes resonances in etched uniform grated single mode fibre was investigated experimentally and theoretically. A sensitivity of ~ 2.94nm/RIU was gained by the LP01 mode to the concentrations of salinity in DI-water. The higher-order modes from LP11 and LP02 have achieved an improved sensitivity to the concentrations of salinity in DI-water concentrations – about 3.43nm/RIU and 18.0nm/RIU, respectively. The experimental results were substantiated by simulations, and again displayed excellent agreement within accuracy R^2~0.99 and R^2>0.97 for simulation and experimental results respectively, and all around λ=1560.0nm.

7.2 Outlook

We believe that we have established the premier route and elements for design and fabrication of the promising micro-photonic fibre devices coated with CNTs. However, there still are a number of factors that need to be investigated, and plenty of developing work in the future.

1. The most logical step forward for the work presented in this thesis is to investigate and work on minimising the losses of the fabricated photonic fibre devices coated with CNTs – that is, by exploring all parameters that are involved, from fibre diameter and the length of the etched section to the coating materials.

2. The optical deposition process can be further examined and developed on etched-silica cladding fibre for the purpose of fabricating a uniform long layer of CNTs coated on the etched area of an optical fibre or FBG within low loss and sufficient coating layer. Moreover, other types of coatings can be developed and tailored, depending on the type of CNTs, the fragileness of the applied thinned fibre, and on the optical application that the coated fibre will be utilised for, such as wrapping a single-layer of Graphene sheet around the etched silica-cladding in fibre optic.

3. Another interesting future direction is investigating additional two-dimensional (2D) monolayer materials, such as monolayers of Molybdenum disulphide (MoS_2) and Tungsten sulphide (WS_2) as coating materials instead of CNTs, since they are among the newer areas of interest. They have opened up new possibilities for exploration in non-linear photonic applications, i.e. FWM, SPM, optical switching and etc.

4. Micro-fibre optic sensors based on the relative shifts of higher-order modes in etched FBGs have the potential to be probed more for enhancing their sensing of sensitivity so it can be explored in many other disciplines – biomedical, industrial, and environment protection. The other higher-order modes from LP31, LP12, LP03, etc. that are created in etched FBG is another exciting subject to be demonstrated experimentally since the investigated numerical results in this work revealed an interesting ultra-high sensing sensitivity. In addition, it would be interesting if these sensors are inspected and exploited as temperature and gas sensors.

5. Finally, bare etched FBG or FBG coated with other materials also make for interesting investigation regarding prospective optical fibre applications such as wavelength tuning and optical switching applications.

List of Publications

- ## Journals

[1] C.L.Sones, I.N.Katis, P.J.W.He, B.Mills, **M.F.Namiq**, P.C.Shardlow, M.Ibsen, R.W.Eason "Laser-induced photo-polymerisation for creation of paper-based fluidic devices" Lab on a Chip 2014 Vol.14 (23) pp.4567-4574.

- ## Conferences

[1] C.L.Sones, I.N.Katis, B.Mills, M.Feinäugle, **M.F.Namiq**, M.Ibsen, R.W.Eason "Laser patterning for paper-based fluidics" SPIE Photonics West: Microfluidics, BioMEMS, and Medical Microsystems XII San Francisco 1-6 Feb 2014 8976-17. (Oral)

[2] **M. F Namiq**, M. Ibsen, "Simple Technique For Real-time Monitoring of the Diameter of Etched Optical Fibres", Photonics Day Conference, Southampton, UK, Sep. 2014. (Poster)

[3] **M. F Namiq**, M. Ibsen, "Simple Technique to Determine the Diameter of Etched Optical Fibres In-situ with Sub-micron Precision Accuracy", CLEO/Europe-EQEC Conference, Munich, Germany, 21st-25th June 2015. (Oral)

[4] **M. F Namiq**, M. Ibsen, "Hydrofluoric Acid Refractive Index Determination using In-situ Monitoring of Etched Fibre Bragg Gratings", Advanced Photonics 2015 Conference, Boston, Massachusetts, 27th-1st July 2015. (Oral)

[5] **M. F Namiq**, M. Ibsen"Refractive Index Determination of Hydrofluoric Acid using In-situ Monitoring of Etched Fibre Bragg Gratings", Siegman Summer School 2016, Barcelona, Spain, 24th-30th July 2016. (Poster)

[6] **M. F Namiq**, M. Ibsen"Simple Salinity Sensor Based on Cladding-Etched Fibre Bragg Gratings", Photonics and Fiber Technology Conference 2016, Sydney, Australia, 5th-8th Sep. 2016. (Oral)

- ## Manuscripts under preparation

[1] **M. F Namiq**, M. Ibsen, **"**Simple Technique of Sensing based on Relative Shifts of Higher-Order Modes in Etched Fibre Bragg Gratings".

List of References

[1] J.-M. Liu, "Photonic devices," ed: ***Cambridge University Press***, 2009.

[2] J. Wang, Y. Chen, and W. J. Blau, "Carbon nanotubes and nanotube composites for nonlinear optical devices," ***Journal of Materials Chemistry,*** vol. 19, pp. 7425-7443, 2009.

[3] R. del Coso and J. Solis, "Relation between nonlinear refractive index and third-order susceptibility in absorbing media," ***Journal of the Optical Society of America B,*** vol. 21, pp. 640-644, 2004.

[4] S. Iijima, "Helical microtubules of graphitic carbon," ***Nature,*** vol. 354, pp. 56-58, 1991.

[5] S. Iijima and T. Ichihashi, "Single-shell carbon nanotubes of 1-nm diameter," vol. 363, pp. 603-605, 1993.

[6] A. Thess, R. Lee, P. Nikolaev, H. Dai, P. Petit, J. Robert, C. Xu, Y. H. Lee, S. G. Kim, A. G. Rinzler, D. T. Colbert, G. E. Scuseria, D. Tomanek, J. E. Fischer, and R. E. Smalley, "Crystalline Ropes of Metallic Carbon Nanotubes," ***Science,*** vol. 273, pp. 483-487, 1996.

[7] S. Yamashita, Y. Inoue, S. Maruyama, Y. Murakami, H. Yaguchi, M. Jablonski, and S. Set, "Saturable absorbers incorporating carbon nanotubes directly synthesized onto substrates and fibers and their application to mode-locked fiber lasers," ***Optics letters,*** vol. 29, pp. 1581-1583, 2004.

[8] P. L. McEuen, "Single-wall carbon nanotubes," ***Physics World,*** vol. 13, pp. 31-36, 2000.

[9] F. Bonaccorso, Z. Sun, T. Hasan, and A. Ferrari, "Graphene photonics and optoelectronics," ***Nature photonics,*** vol. 4, pp. 611-622, 2010.

[10] S. Set, H. Yaguchi, M. Jablonski, Y. Tanaka, Y. Sakakibara, A. Rozhin, M. Tokumoto, H. Kataura, Y. Achiba, and K. Kikuchi, "A noise suppressing saturable absorber at 1550nm based on carbon nanotube technology," presented at the ***Optical Fiber Communication Conference***, 2003.

[11] S. Y. Set, H. Yaguchi, M. Jablonski, Y. Tanaka, Y. Sakakibara, A. G. Rozhin, M. Tokumoto, H. Kataura, Y. Achiba, and K. Kikuchi, "A Noise Suppressing Saturable Absorber at 1550nm Based on Carbon Nanotube Technology," in ***Optical Fiber Communication Conference***, Atlanta, Georgia, 2003, p. FL2.

[12] J. Nicholson, R. Windeler, and D. DiGiovanni, "Optically driven deposition of single-walled carbon-nanotube saturable absorbers on optical fiber end-faces," ***Optics Express,*** vol. 15, pp. 9176-9183, 2007.

[13] S. Li-Yang, M. B. Jakubinek, T. Sun, B. Simard, and J. Albert, "Four-wave mixing in carbon nanotube-coated optical fiber gratings," ***Applied Physics Letters,*** vol. 100, pp. 1-3(071108), 2012.

[14] K. Chow and S. Yamashita, "Four-wave mixing in a single-walled carbon-nanotube-deposited D-shaped fiber and its application in tunable wavelength conversion," ***Optics Express,*** vol. 17, pp. 15608-15613, 2009.

[15] K. K. Chow, M. Tsuji, and S. Yamashita, "Single-walled carbon-nanotube-deposited tapered fiber for four-wave mixing based wavelength conversion," ***Applied Physics Letters,*** vol. 96, pp. 1-3(061104), 2010.

[16] A. Martinez, K. Fuse, B. Xu, and S. Yamashita, "Optical deposition of graphene and carbon nanotubes in a fiber ferrule for passive mode-locked lasing," ***Optics Express***, vol. 18, pp. 23054-23061, 2010.

[17] Y.-W. Song, S. Yamashita, C. S. Goh, and S. Y. Set, "Carbon nanotube mode lockers with enhanced nonlinearity via evanescent field interaction in D-shaped fibers," ***Optics letters***, vol. 32, pp. 148-150, 2007.

[18] S. Sridevi, K. S. Vasu, N. Jayaraman, S. Asokan, and A. K. Sood, "Optical bio-sensing devices based on etched fiber Bragg gratings coated with carbon nanotubes and graphene oxide along with a specific dendrimer," ***Sensors and Actuators B: Chemical***, vol. 195, pp. 150-155, 2014.

[19] R. Kashyap, *Fiber Bragg Gratings*, 1st. ed.: ***Academic Press***, 1999.

[20] K. O. Hill and G. Meltz, "Fiber Bragg grating technology fundamentals and overview," ***Journal of Lightwave Technology,,*** vol. 15, pp. 1263-1276, 1997.

[21] A. Iadicicco, A. Cusano, S. Campopiano, A. Cutolo, and M. Giordano, "Thinned fiber Bragg gratings as refractive index sensors," ***Sensors Journal, IEEE***, vol. 5, pp. 1288-1295, 2005.

[22] W. Liang, Y. Huang, Y. Xu, R. K. Lee, and A. Yariv, "Highly sensitive fiber Bragg grating refractive index sensors," ***Applied Physics Letters***, vol. 86, pp. 1-3 (151122), 2005.

[23] S. Yamashita, Y. Inoue, K. Hsu, T. Kotake, H. Yaguchi, D. Tanaka, M. Jablonski, and S. Y. Set, "5-GHz pulsed fiber Fabry-Pe'rot laser mode-locked using carbon nanotubes," ***Photonics Technology Letters, IEEE***, vol. 17, pp. 750-752, 2005.

[24] T. Hasan, Z. Sun, F. Wang, F. Bonaccorso, P. H. Tan, A. G. Rozhin, and A. C. Ferrari, "Nanotube–polymer composites for ultrafast photonics," ***Advanced Materials***, vol. 21, pp. 3874-3899, 2009.

[25] S. Yamashita, Y. Inoue, S. Maruyama, Y. Murakami, H. Yaguchi, T. Kotake, and S. Y. Set, "Mode-locked fiber lasers using adjustable saturable absorption in vertically aligned carbon nanotubes," ***Japanese journal of applied physics***, vol. 45, pp. L17-L19, 2006.

[26] Y.-W. Song, K. Morimune, S. Y. Set, and S. Yamashita, "Polarization insensitive all-fiber mode-lockers functioned by carbon nanotubes deposited onto tapered fibers," ***Applied Physics Letters***, vol. 90, pp. 1-3(021101), 2007.

[27] K. Kashiwagi and S. Yamashita, "Deposition of carbon nanotubes around microfiber via evanascent light," ***Optics Express***, vol. vol.17, pp. 18364-18370, 2009.

[28] B. Xu, M. Omura, M. Takiguchi, A. Martinez, T. Ishigure, S. Yamashita, and T. Kuga, "Carbon nanotube/polymer composite coated tapered fiber for four wave mixing based wavelength conversion," ***Optics Express***, vol. 21, pp. 3651-3657, 2013.

[29] S. Y. Choi, F. Rotermund, H. Jung, K. Oh, and D.-I. Yeom, "Femtosecond mode-locked fiber laser employing a hollow optical fiber filled with carbon nanotube dispersion as saturable absorber," ***Optics Express***, vol. 17, pp. 21788-21793, 2009.

[30] K. T. Dinh, Y.-W. Song, S. Yamashita, and S. Y. Set, "Realization of All-fiber Tunable Filter & High Optical Power Blocker Using Thinned Fiber Bragg Gratings Coated with Carbon Nanotubes," in ***Applied Physics Express***, 2008, pp. 1-3(012008).

[31] G. E. Villanueva, M. B. Jakubinek, B. Simard, C. J. Otón, P. Pérez-Millán, and J. Albert, "Tilted fiber Bragg grating assisted nonlinear effects in carbon nanotube-coated

optical fibers," in ***Lasers and Electro-Optics Europe (CLEO EUROPE/EQEC)***, 2011, pp. 1-1.

[32] B. N. Shivananju, A. Suri, S. Asokan, and A. Misra, "Carbon nanotube coated fiber Bragg grating for photomechanical optic modulator," ***Review of Scientific Instruments***, vol. 84, pp. 1-8 (095101), 2013.

[33] O. S. Wolfbeis, "Fiber-optic chemical sensors and biosensors," ***Analytical chemistry***, vol. 80, pp. 4269-4283, 2008.

[34] A. Cusano, A. Iadicicco, S. Campopiano, M. Giordano, and A. Cutolo, "Thinned and micro-structured fibre Bragg gratings: towards new all-fibre high-sensitivity chemical sensors," ***Journal of Optics A: Pure and Applied Optics***, vol. 7, pp. 734–741, 2005.

[35] J.-L. Kou, M. Ding, J. Feng, Y.-Q. Lu, F. Xu, and G. Brambilla, "Microfiber-based Bragg gratings for sensing applications: a review," ***Sensors***, vol. 12, pp. 8861-8876, 2012.

[36] A. N. Chryssis, S. M. Lee, S. B. Lee, S. S. Saini, and M. Dagenais, "High sensitivity evanescent field fiber Bragg grating sensor," ***Photonics Technology Letters, IEEE***, vol. 17, pp. 1253-1255, 2005.

[37] S.-M. Lee, S. S. Saini, and M.-Y. Jeong, "Simultaneous measurement of refractive index, temperature, and strain using etched-core fiber Bragg grating sensors," ***Photonics Technology Letters, IEEE***, vol. 22, pp. 1431-1433, 2010.

[38] J.-l. Kou, S.-j. Qiu, F. Xu, and Y.-q. Lu, "Demonstration of a compact temperature sensor based on first-order Bragg grating in a tapered fiber probe," ***Optics Express***, vol. 19, pp. 18452-18457, 2011.

[39] D. Grobnic, S. J. Mihailov, D. Huimin, and C. W. Smelser, "Bragg grating evanescent field sensor made in biconical tapered fiber with femtosecond IR radiation," ***Photonics Technology Letters, IEEE***, vol. 18, pp. 160-162, 2006.

[40] X. Fang, C. R. Liao, and D. N. Wang, "Femtosecond laser fabricated fiber Bragg grating in microfiber for refractive index sensing," ***Optics letters***, vol. 35, pp. 1007-1009, 2010.

[41] A. Iadicicco, S. Campopiano, A. Cutolo, M. Giordano, and A. Cusano, "Refractive index sensor based on microstructured fiber Bragg grating," ***Photonics Technology Letters, IEEE***, vol. 17, pp. 1250-1252, 2005.

[42] Y. Zhang, B. Lin, S. C. Tjin, H. Zhang, G. Wang, P. Shum, and X. Zhang, "Refractive index sensing based on higher-order mode reflection of a microfiber Bragg grating," ***Optics Express***, vol. 18, pp. 26345-26350, 2010.

[43] A. Iadicicco, S. Campopiano, A. Cutolo, M. Giordano, and A. Cusano, "Nonuniform thinned fiber Bragg gratings for simultaneous refractive index and temperature measurements," ***Photonics Technology Letters, IEEE***, vol. 17, pp. 1495-1497, 2005.

[44] Q. Zhang, T. Zhu, J. Zhang, and K. S. Chiang, "Micro-Fiber-Based FBG Sensor for Simultaneous Measurement of Vibration and Temperature," ***Photonics Technology Letters, IEEE***, vol. 25, pp. 1751-1753, 2013.

[45] E. Lyons and H. Lee, "Demonstration of an etched cladding fiber Bragg grating filter with reduced tuning force requirement," ***Photonics Technology Letters, IEEE***, vol. 11, pp. 1626-1628, 1999.

[46] B. N. Shivananju, S. Yamdagni, R. Fazuldeen, A. K. S. Kumar, S. P. Nithin, M. M. Varma, and S. Asokan, "Highly Sensitive Carbon Nanotubes Coated Etched Fiber Bragg

Grating Sensor for Humidity Sensing," ***IEEE Sensors Journal,*** vol. 14, pp. 2615-2619, 2014.

[47] G. Rajan, Y. M. Noor, B. Liu, E. Ambikairaja, D. J. Webb, and G.-D. Peng, "A fast response intrinsic humidity sensor based on an etched singlemode polymer fiber Bragg grating," ***Sensors and Actuators A: Physical,*** vol. 203, pp. 107-111, 2013.

[48] B. N. Shivananju, S. Yamdagni, R. Fazuldeen, A. K. Sarin Kumar, G. M. Hegde, M. M. Varma, and S. Asokan, "CO2 sensing at room temperature using carbon nanotubes coated core fiber Bragg grating," ***Review of Scientific Instruments,*** vol. 84, pp. 1-7 (065002), 2013.

[49] Y. Wu, B. Yao, A. Zhang, Y. Rao, Z. Wang, Y. Cheng, Y. Gong, W. Zhang, Y. Chen, and K. Chiang, "Graphene-coated microfiber Bragg grating for high-sensitivity gas sensing," ***Optics letters,*** vol. 39, pp. 1235-1237, 2014.

[50] D. A. Pereira and O. Fraza, "Fiber Bragg grating sensing system for simultaneous measurement of salinity and temperature," ***Optical Engineering,*** vol. 43, pp. 299-304, 2004.

[51] R. Ismaeel, "Microfiber devices based on evanescent field coupling," Ph.D. , Physical Sciences and Engineering, ***University of Southampton***, UK 2015.

[52] T. Lee, "Nonlinear properties of optical microfibres," Ph.D., Faculty of Physical Sciences and Engineering, ***University of Southampton***, 2013.

[53] R. Ismaeel, T. Lee, M. Ding, M. Belal, and G. Brambilla, "Optical microfiber passive components," ***Laser & Photonics Reviews,*** vol. 7, pp. 350-384, 2013.

[54] T. Liu, K. Liu, J. Jiang, E. Li, H. Zhang, D. Jia, and Y. Zhang, "Photonic sensors review recent progress of fiber sensing technologies in Tianjin University," ***Photonic Sensors,*** vol. 1, pp. 90-96, 2011.

[55] S. W. H. K. S. Lim, H. Arof and H. Ahmad *Fabrication and Applications of Microfiber*: ***InTech***, 2012.

[56] M. Sumetsky, "Optical microfibers: fundamentals and applications," in ***Conference on Lasers and Electro-Optics***, 2006, p. CMGG1.

[57] G. Brambilla, F. Xu, and X. Feng, "Fabrication of optical fibre nanowires and their optical and mechanical characterisation," ***Electronics Letters,*** vol. 42, pp. 517-519, 2006.

[58] J. A. Buck, *Fundamentals of Optical Fibers*, 2nd ed. vol. 1: ***John Wiley & Sons, Inc.***, 2004.

[59] J. D. Shi, "Periodic fibre devices for advanced applications in all-optical systems," PhD Thesis, ***University of Southampton***, 2012.

[60] G. P. Agrawal, *Nonlinear Fiber Optics* 5th ed.: ***Academic Press***, 2013.

[61] G. P. Agrawal, *Fiber-optic communication systems* vol. 222: ***John Wiley & Sons***, 2010.

[62] A. Othonos and K. Kalli, *Fiber Bragg gratings: fundamentals and applications in telecommunications and sensing*: ***Artech House Boston***, 1999.

[63] T. Erdogan, "Fiber grating spectra," ***Lightwave Technology, Journal of,*** vol. 15, pp. 1277-1294, 1997.

[64] P. Antunes, H. Varum, and P. S. Andre, "Uniaxial fiber Bragg grating accelerometer system with temperature and cross axis insensitivity," ***Measurement,*** vol. 44, pp. 55-59, 2011.

[65] S. P. Singh and N. Singh, "Nonlinear effects in optical fibers: Origin, management and applications," ***Progress In Electromagnetics Research,*** vol. 73, pp. 249-275, 2007.

[66] J. Toulouse, "Optical nonlinearities in fibers: review, recent examples, and systems applications," ***Lightwave Technology, Journal of,*** vol. 23, pp. 3625-3641, 2005.

[67] V. A. Margulis and T. A. Sizikova, "Theoretical study of third-order nonlinear optical response of semiconductor carbon nanotubes," ***Physica B: Condensed Matter,*** vol. 245, pp. 173-189, 1998.

[68] H. Zhang, S. Virally, Q. Bao, L. Kian Ping, S. Massar, N. Godbout, and P. Kockaert, "Z-scan measurement of the nonlinear refractive index of graphene," ***Optics letters,*** vol. 37, pp. 1856-1858, 2012.

[69] E. P. Ippen, C. V. Shank, and T. K. Gustafson, "Self-phase modulation of picosecond pulses in optical fibers," ***Applied Physics Letters,*** vol. 24, pp. 190-192, 1974.

[70] G. Veith, "Self-Phase Modulation In Optical Fibers," in ***1987 Symposium on the Technologies for Optoelectronics***, 1988, pp. 154-161.

[71] O. Aso, M. Tadakuma, and S. Namiki, "Four-wave mixing in optical fibers and its applications," ***Furukawa Review,*** vol. 19, pp. 63-68, 2000.

[72] V. N. Popov, "Carbon nanotubes: properties and application," ***Materials Science and Engineering: R: Reports,*** vol. 43, pp. 61-102, 2004.

[73] M. J. O'connell, *Carbon nanotubes: properties and applications*: ***CRC press***, 2006.

[74] P. M. Ajayan, L. S. Schadler, C. Giannaris, and A. Rubio, "Single-Walled Carbon Nanotube–Polymer Composites: Strength and Weakness," ***Advanced Materials,*** vol. 12, pp. 750-753, 2000.

[75] Y. Wenrong, T. Pall, J. J. Gooding, P. R. Simon, and B. Filip, "Carbon nanotubes for biological and biomedical applications," ***Nanotechnology,*** vol. 18, p. 412001, 2007.

[76] L. Dai, P. Soundarrajan, and T. Kim, "Sensors and sensor arrays based on conjugated polymers and carbon nanotubes," in *Pure and Applied Chemistry* vol. 74, ed, 2002, p. 1753.

[77] S. Yamashita, "A tutorial on nonlinear photonic applications of carbon nanotube and graphene," ***Journal of Lightwave Technology,*** vol. 30, pp. 427-447, 2012.

[78] M. Dresselhaus, G. Dresselhaus, and R. Saito, "Physics of carbon nanotubes," ***Carbon,*** vol. 33, pp. 883-891, 1995.

[79] S. Iijima and T. Ichihashi, "Single-shell carbon nanotubes of 1-nm diameter," ***Nature,*** vol. 363, pp. 603-605, 1993.

[80] G. Y. Guo, K. C. Chu, D.-s. Wang, and C.-g. Duan, "Linear and nonlinear optical properties of carbon nanotubes from first-principles calculations," ***Physical Review B,*** vol. 69, pp. 1-11 (205416), 2004.

[81] A. L. Kalamkarov, A. V. Georgiades, S. K. Rokkam, V. P. Veedu, and M. N. Ghasemi-Nejhad, "Analytical and numerical techniques to predict carbon nanotubes properties," ***International Journal of Solids and Structures,*** vol. 43, pp. 6832-6854, 2006.

[82] P. Avouris, M. Freitag, and V. Perebeinos, "Carbon-nanotube photonics and optoelectronics," ***Nature photonics,*** vol. 2, pp. 341-350, 2008.

[83] R. Martel, T. Schmidt, H. R. Shea, T. Hertel, and P. Avouris, "Single- and multi-wall carbon nanotube field-effect transistors," ***Applied Physics Letters,*** vol. 73, pp. 2447-2449, 1998.

[84] V. Choudhary and A. Gupta, *Polymer/carbon nanotube nanocomposites*: ***InTech***, 2011.

[85] M. Monthioux, P. Serp, E. Flahaut, M. Razafinimanana, C. Laurent, A. Peigney, W. Bacsa, and J.-M. Broto, "Introduction to carbon nanotubes," in *Springer Handbook of Nanotechnology*, ed: ***Springer***, 2010, pp. 47-118.

[86] R. B. Weisman and S. Subramoney. (2006) Carbon nanotubes. *The Electrochemical Society Interface*

42-46.

[87] S. Y. Set, H. Yaguchi, Y. Tanaka, and M. Jablonski, "Laser mode locking using a saturable absorber incorporating carbon nanotubes," ***Journal of Lightwave Technology,*** vol. 22, pp. 51-56, 2004.

[88] K. S. Kim, G. Cota-Sanchez, C. T. Kingston, M. Imris, B. Simard, and G. Soucy, "Large-scale production of single-walled carbon nanotubes by induction thermal plasma," ***Journal of physics D: Applied physics,*** vol. 40, p. 2375, 2007.

[89] R. Purohit, K. Purohit, S. Rana, R. S. Rana, and V. Patel, "Carbon Nanotubes and Their Growth Methods," ***Procedia Materials Science,*** vol. 6, pp. 716-728, 2014.

[90] H. J. Kbashi, "Fabrication of submicron-diameter and taper fibers using chemical etching," ***Journal of Materials Science & Technology,*** vol. 28, pp. 308-312, 2012.

[91] K. Yallup and K. Iniewski, *Technologies for smart sensors and sensor fusion*: ***CRC Press***, 2014.

[92] G. Spierings, "Wet chemical etching of silicate glasses in hydrofluoric acid based solutions," ***Journal of Materials Science,*** vol. 28, pp. 6261-6273, 1993.

[93] T. Oku, R. Hattori, and K. Sato, "Mechanism for Breakage of Si-O Networks of SiO2 Films in HF Solutions," ***MRS Online Proceedings Library Archive,*** vol. 492, pp. 213–218, 1998.

[94] M. Zourob and A. Lakhtakia, *Optical Guided-wave Chemical and Biosensors: II* vol. 2: ***Springer***, 2010.

[95] C. J. Gow, D. W. Martin, and K. B. Albaugh, "Use of Dilute, Aqueous HF for Selective Etching," ***SOVIET PHYSICS CRYSTALLOGRAPHY C/C OF KRISTALLOGRAFIIA,*** vol. 259, pp. 433-433, 1993.

[96] C. R. Kurkjian, M. J. Matthewson, and J. Rooney, "Effects of heat treatment and HF etching on the strength of silica lightguides," in ***Photonics Europe; Reliability of Optical Fiber Components, Devices, Systems, and Networks II.***, 2004, pp. 223-229.

[97] L. Fuller. (2008). *Wet Etch for Microelectronics*.

[98] G. Axel, G. Matthias, and F. Henning, "Deep wet etching of fused silica glass for hollow capillary optical leaky waveguides in microfluidic devices," ***Journal of Micromechanics and Microengineering,*** vol. 11, p. 257, 2001.

[99] S. Ingo and F. Henning, "Deep fused silica wet etching using an Au-free and stress-reduced sputter-deposited Cr hard mask," ***Journal of Micromechanics and Microengineering***, vol. 15, p. 2130, 2005.

[100] E. C. Group. Technical Data:BOE Buffered Oxide Etchants,Clean, Uniform Etching for Semiconductor Devices Electronic Chemicals [Online].

[101] R. McIntosh, T.-S. Kuan, and E. Defresart, "Hydrogen fluoride vapor etching for Pre-Epi silicon surface preparation," ***Journal of electronic materials***, vol. 21, pp. 57-60, 1992.

[102] E. Sinchenko, W. E. K. Gibbs, A. P. Mazzolini, and P. R. Stoddart, "The Effect of the Cladding Refractive Index on an Optical Fiber Evanescent-Wave Sensor," ***Lightwave Technology, Journal of***, vol. 31, pp. 3251-3257, 2013.

[103] K.-i. Kitayama, "Light propagation in optical fibers," in *Optical Code Division Multiple Access: A Practical Perspective*, K.-i. Kitayama, Ed., ed Cambridge: ***Cambridge University Press***, 2014, pp. 65-106.

[104] Fosco. (2016). *BASIC OPTICS FOR OPTICAL FIBER*.

[105] F. K. Coradin, G. R. C. Possetti, R. C. Kamikawachi, M. Muller, and J. L. Fabris, "Etched fiber bragg gratings sensors for water-ethanol mixtures: a comparative study," ***Journal of Microwaves, Optoelectronics and Electromagnetic Applications***, vol. 9, pp. 131-143, 2010.

[106] L. Qi, C.-L. Zhao, J. Kang, Y. Jin, J. Wang, M. Ye, and S. Jin, "Simultaneous measurement of refractive index and temperature based on intensity demodulation using matching grating method," ***Review of Scientific Instruments***, vol. 84, pp. 1-5(075004), 2013.

[107] T. Guo, F. Liu, B.-O. Guan, and J. Albert, "[INVITED] Tilted fiber grating mechanical and biochemical sensors," ***Optics & Laser Technology***, vol. 78, pp. 19-33, 2016.

[108] Y. Jiang, C. Liu, W. Zhang, D. Mao, D. Yang, and J. Zhao, "Multi-parameter sensing using a fiber Bragg grating inscribed in dual-mode fiber," ***IEEE Photonics Technology Letters***, vol. PP, pp. 1-1, 2017.

[109] K. Kashiwagi and S. Yamashita, "Optical Deposition of Carbon Nanotubes for Fiber-based Device Fabrication," ed: ***INTECH Open Access Publisher.***, 2010, pp. 674(385-402).

[110] K. Kieu and M. Mansuripur, "Femtosecond laser pulse generation with a fiber taper embedded in carbon nanotube/polymer composite," ***Optics letters***, vol. 32, pp. 2242-2244, 2007.

[111] H. H. Liu and K. K. Chow, "Dark pulse generation in fiber lasers incorporating carbon nanotubes," ***Optics Express***, vol. 22, pp. 29708-29713, 2014.

[112] S. Ko, J. Lee, J. Koo, B. S. Joo, M. Gu, and J. H. Lee, "Chemical Wet Etching of an Optical Fiber Using a Hydrogen Fluoride-Free Solution for a Saturable Absorber Based on the Evanescent Field Interaction," ***Journal of Lightwave Technology***, vol. 34, pp. 3776-3784, 2016.

[113] T. Wang, "LIGHT SCATTERING STUDY ON SINGLE WALL CARBON NANOTUBE (SWNT) DISPERSIONS " Master of Science Master of Science, School of Polymer, Textile and Fiber Engineering ***Georgia Institute of Technology*** USA, 2004.

[114] H. Soetedjo, M. F. Mora, and C. D. Garcia, "Optical Properties of Single-Wall Carbon Nanotube Films Deposited on Si/SiO(2) Wafers," ***Thin Solid Films***, vol. 518, pp. 3954-3959, 2010.

[115] H. H. Liu, Y. Yang, and K. K. Chow, "Enhancement of thermal damage threshold of carbon-nanotube-based saturable absorber by evanescent-field interaction on fiber end," ***Optics Express,*** vol. 21, pp. 18975-18982, 2013.

[116] C. Vinegoni, M. Wegmuller, and N. Gisin, "Measurements of the nonlinear coefficient of standard, SMF, DSF, and DCF fibers using a self-aligned interferometer and a Faraday mirror," ***IEEE Photonics Technology Letters,*** vol. 13, pp. 1337-1339, 2001.

[117] K. K. Chow, S. Yamashita, and S. Y. Set, "Four-wave-mixing-based wavelength conversion using a single-walled carbon-nanotube-deposited planar lightwave circuit waveguide," ***Optics letters,*** vol. 35, pp. 2070-2072, 2010.

[118] N. R. Tummala and A. Striolo, "SDS Surfactants on Carbon Nanotubes: Aggregate Morphology," ***Acs Nano,*** vol. 3, pp. 595-602, 2009.

[119] X. Li, K. Wu, Z. Sun, B. Meng, Y. Wang, Y. Wang, X. Yu, X. Yu, Y. Zhang, P. P. Shum, and Q. J. Wang, "Single-wall carbon nanotubes and graphene oxide-based saturable absorbers for low phase noise mode-locked fiber lasers," ***Scientific Reports,*** vol. 6, pp. 1-9 (125266), 2016.

[120] S. Y. Ryu, K.-S. Kim, J. Kim, and S. Kim, "Degradation of optical properties of a film-type single-wall carbon nanotubes saturable absorber (SWNT-SA) with an Er-doped all-fiber laser," ***Optics Express,*** vol. 20, pp. 12966-12974, 2012/06/04 2012.

[121] A. Iadicicco, A. Cusano, A. Cutolo, R. Bernini, and M. Giordano, "Thinned fiber Bragg gratings as high sensitivity refractive index sensor," ***IEEE Photonics Technology Letters,*** vol. 16, pp. 1149-1151, 2004.

[122] K. Okamoto, *Fundamentals of optical waveguides*, 2nd edition ed.: ***Academic press***, 2010.

[123] M. Monerie, "Propagation in doubly clad single-mode fibers," ***Quantum Electronics, IEEE Journal of,*** vol. 18, pp. 535-542, 1982.

[124] T. Kato, Y. Suetsugu, and M. Nishimura, "Estimation of nonlinear refractive index in various silica-based glasses for optical fibers," ***Optics letters,*** vol. 20, pp. 2279-2281, 1995.

[125] A. Martinez and S. Yamashita, "Carbon Nanotube-Based Photonic Devices: Applications in Nonlinear Optics," in *Carbon Nanotubes Applications on Electron Devices*, ed: ***InTech***, 2011, pp. 367-387.

[126] M. A. Davis and A. D. Kersey, "Fiber Bragg grating sensors for infrastructure sensing," in ***Optical Fiber Communication. OFC 97., Conference on***, 1997, pp. 177-178.

[127] A. Othonos, K. Kalli, and G. E. Kohnke, "Fiber Bragg gratings: Fundamentals and applications in telecommunications and sensing," ***Physics Today,*** vol. 53, pp. 1263-1276, 2000.

[128] A. Iadicicco, S. Campopiano, A. Cutolo, M. Giordano, and A. Cusano, "Microstructured fibre Bragg gratings: analysis and fabrication," ***Electronics Letters,*** vol. 41, pp. 466-468, 2005.

[129] B. Lee, "Review of the present status of optical fiber sensors," ***Optical Fiber Technology,*** vol. 9, pp. 57-79, 2003.

[130] B.-O. Guan, H.-Y. Tam, X.-M. Tao, and X.-Y. Dong, "Simultaneous strain and temperature measurement using a superstructure fiber Bragg grating," ***Photonics Technology Letters, IEEE,*** vol. 12, pp. 675-677, 2000.

[131] W. W. Morey, G. Meltz, and W. H. Glenn, "Fiber Optic Bragg Grating Sensors," presented at the ***Fiber Optic and Laser Sensors VII***, 1990.

[132] W. W. Morey, J. R. Dunphy, and G. Meltz, "Multiplexing fiber Bragg grating sensors," presented at the ***Distributed and Multiplexed Fiber Optic Sensors*** 1992.

[133] B.-b. Luo, X.-j. Zhou, M.-f. Zhao, N.-b. Zhong, and S.-f. Wang, "Recent developments in microstructured fiber Bragg grating refractive index sensors," ***Journal of Photonics for Energy,*** vol. 1, pp. 1-12 (018002), 2010.

[134] B. N. Shivananju, M. Renilkumar, G. R. Prashanth, S. Asokan, and M. M. Varma, "Detection Limit of Etched Fiber Bragg Grating Sensors," ***Journal of Lightwave Technology,*** vol. 31, pp. 2441-2447, 2013.

[135] B. Shivananju, M. Varma, S. Asokan, S. Yamdagni, R. Fazuldeen, and S. Nithin, "Highly Sensitive Carbon Nanotubes Coated Etched Fiber Bragg Grating Sensor for Humidity Sensing," ***IEEE Sensors Journal,*** vol. 14, pp. 2615-2619, 2014.

[136] S. Sridevi, K. S. Vasu, N. Bhat, S. Asokan, and A. K. Sood, "Ultra sensitive NO2 gas detection using the reduced graphene oxide coated etched fiber Bragg gratings," ***Sensors and Actuators B: Chemical,*** vol. 223, pp. 481-486, 2016.

[137] W. Yu, Y. Bai-Cheng, C. Yang, R. Yun-Jiang, G. Yuan, Z. Weili, W. Zegao, and C. Yuanfu, "Hybrid Graphene-Microfiber Waveguide for Chemical Gas Sensing," ***Selected Topics in Quantum Electronics, IEEE Journal of,*** vol. 20, pp. 49-54, 2014.

[138] A. Chryssis, S. Saini, S. Lee, and M. Dagenais, "Increased sensitivity and parametric discrimination using higher order modes of etched-core fiber Bragg grating sensors," ***Photonics Technology Letters, IEEE,*** vol. 18, pp. 178-180, 2006.

[139] D. F. Penning, D. Weimer, and W. F. Rumpel, "Indices of refraction of HF and F2. II," ***The Journal of Chemical Physics,*** vol. 59, pp. 2496-2497, 1973.

[140] D. L. Drummond, "Refractive index of HF from 2.5 μm to 2.9 μm," ***Applied optics,*** vol. 21, pp. 4331-4334, 1982.

[141] H. Z. Yang, M. M. Ali, M. R. Islam, K.-S. Lim, D. S. Gunawardena, and H. Ahmad, "Cladless few mode fiber grating sensor for simultaneous refractive index and temperature measurement," ***Sensors and Actuators A: Physical,*** vol. 228, pp. 62-68, 2015.

[142] M. Namiq and M. Ibsen, "Simple Technique to Determine the Diameter of Etched Optical Fibres In-situ with Sub-micron Precision Accuracy," presented at the ***The European Conference on Lasers and Electro-Optics***, 2015.

[143] M. F. Namiq and M. Ibsen, "Hydrofluoric Acid Refractive Index Determination using In-situ Monitoring of Etched Fibre Bragg Gratings," presented at the ***Optical Sensors***, 2015.